Estimation of tree height from PolInSAR: The effects of vertical structure and temporal decorrelation

Nafiseh Ghasemi

ESTIMATION OF TREE HEIGHT FROM POLINSAR: THE EFFECTS OF VERTICAL STRUCTURE AND TEMPORAL DECORRELATION

DISSERTATION

to obtain
the degree of doctor at the University of Twente,
on the authority of the rector magnificus,
prof.dr. T.T.M. Palstra,
on account of the decision of the Doctorate Board,
to be publicly defended
on Thursday, February 28, 2019 at 14.45 hrs

by
Nafiseh Ghasemi
born on June 20th, 1986
in Malayer, Iran

This dissertation is approved by:

Prof.dr.ir. A. Stein (supervisor)
Dr.V. Tolpekin (co-supervisor)

ITC dissertation number 344
ITC, P.O. Box 217, 7500 AE Enschede, The Netherlands

ISBN: 978–90–365–4730–7
DOI: http://dx.doi.org/10.3990/1.9789036547307
Printed by: ITC Printing Department, Enschede, The Netherlands

UNIVERSITY OF TWENTE.
ITC
FACULTY OF GEO-INFORMATION SCIENCE AND EARTH OBSERVATION

Graduation committee

Chair and Secretary

Prof.dr.ir. A. Veldkamp	University of Twente

Supervisor

Prof.dr.ir. A. Stein	University of Twente

Co-supervisor

Dr.V. Tolpekin	University of Twente

Members

Prof. dr. N. Kerle	University of Twente
Prof. dr. F.D. van der Meer	University of Twente
Prof. dr. A. Reigber	Deutsches Zentrum für Luft- und Raumfahrt (DLR)
Prof. dr. M. Motagh	Leibniz University Hannover

To my beloved parents
and
my dearest sisters:
Shadi and Reyhane

Summary

Height values of trees are an important indicator of the health and viability of forests. At present, it is the main biophysical parameter observable from remote sensing images, in particular from Polarimetric Interferometric SAR (PolInSAR) data. It is important to have these values as accurately as possible. The accuracy of estimated tree height obtained by PolInSAR is affected by temporal decorrelation. Modeling this correlation is the focus of the current thesis.

The first chapter explores modeling of the structure function. We used the Fourier-Legendre series and combined it with the Gaussian motion function for modeling the vertical displacement of the scatterers. This improved the height estimation accuracy using a single-baseline PolInSAR image pair. The improvement was higher when applied in P-band than in L-band. The reason is the different interaction of the ground and vegetation layer and the lower penetration of L-band. The penetration depth becomes important if we are interested in reconstructing the vertical profile of trees at a higher resolution. In this case, P-band should be used; this fortunately will be available in satellite sensors in near future. For L-band, the exponential function as assumed by the RVoG and RMoG model was equally good.

The second chapter proposes the use of the Polarimetric Coherence Tomography (PCT) model to estimate height from multi-baseline SAR tomostack data. In the past, temporal decorrelation was considered as a separate source of error that is independent of the canopy. It thus causes biased height estimates. Merging of a Fourier-Legendre series from the PCT model with a temporal decorrelation function from the Random Motion over Ground (RMoG) model has been explored to solve this problem. Results showed an improvement of height estimation accuracy after applying this modification. The optimal number of terms of the Fourier-Legendre series varied for each pixel. This can be used as an indicator of the complexity of the vegetation layer as for multi-layer dense forests, more terms are required. This chapter shows that increasing the number of unknown parameters can be done via segmenting the area into different height classes and selecting the optimum number of unknown parameters for each class.

The third chapter focuses on obtaining the most accurate height maps from PolInSAR. This is important by itself, whereas height also serves as the main biophysical parameter contributing to the estimation of biomass. The effect of mitigating temporal decorrelation was thus examined on biomass retrieval accuracy. This research developed new allometric equations for this purpose and tested different strategies for regression. This was challenging due to the lack of sufficient field data. The strategy to develop a new allometric equation based on height only is important. A parameter usually measured during fieldwork is H100, defined as the basal area weighted average of the 100 highest trees in each plot,. This chapter showed that the relation between PolInSAR height and H100 is weak, because PolInSAR height estimates the average of heights inside the plots and does not simply coincide with H100.

The fourth chapter discusses how to take temporal decorrelation into the estimation of tree heights. It addresses the sensitivity of the proposed modified model to the choice of complex coherence estimation method. The basic step of estimating height in any of the explained models is the selection of homogeneous pixels. To do so, we distinguished polarimetric from polarimetric-interferometric information. By addressing the pixel selection we could jointly take the phase and the magnitude values of the pixels into account. We employed two adaptive methods to define statistically homogeneous pixels. Height estimation accuracy increased after applying the adaptive methods. Since the proposed adaptive methods are computationally more intensive, a trade-off between the desired accuracy and computation is required prior to selection of any method.

To summarize, this dissertation improved the accuracy of tree height estimation from airborne fully polarized InSAR data by carefully addressing temporal decorrelation. This is potentially of use for future SAR satellite missions.

Samenvatting

De hoogtes van bomen zijn een belangrijke indicator voor de gezondheid en leefbaarheid van bossen. Op dit moment is het de belangrijkste biofysische parameter die waarneembaar is op remote sensing beelden, in het bijzonder adoor middel van Polarimetric Interferometric SAR (PolInSAR) data. Het is belangrijk om deze waarden zo nauwkeurig mogelijk te hebben. De nauwkeurigheid van de geschatte boomhoogte verkregen door PolInSAR wordt beïnvloed door temporele decorrelatie. Het modelleren van deze correlatie is de focus van dit proefschrift. Het eerste hoofdstuk onderzoekt het modellering van de structuurfunctie. Hiervoor gebruikten we de Fourier-Legendre-reeks en we combineerden deze met de Gaussische bewegingsfunctie voor het modelleren van de verticale verplaatsing van de verstrooiers. Dit verbeterde de nauwkeurigheid van de nauwkeurigheid van de hoogte met behulp van een PolInSAR-beeldpaar met één basislijn. De verbetering was hoger wanneer deze werd toegepast in P-band dan in L-band. De reden hiervoor is de verschillende interactie van de grond- en vegetatielaag en de lagere penetratie van de L-band. De penetratiediepte wordt belangrijk als we geïnteresseerd zijn in het reconstrueren van het verticale profiel van bomen met een hogere resolutie. In dit geval moet P-band worden gebruikt; dit zal gelukkig in de nabije toekomst beschikbaar zijn in satellietsensoren. Voor L-band was de exponentiële functie zoals die aangenomen wordt door het RVoG- en RMoG-model even goed. Het tweede hoofdstuk stelt het gebruik voor van het Polarimetric Coherence Tomography (PCT)-model om de hoogte van multi-baseline SAR tomostack gegevens te schatten. In het verleden is temporele decorrelatie beschouwd als een afzonderlijke bron van fouten die onafhankelijk is van het bladerdak. Het veroorzaakt dus onzuivere hoogteschattingen. Het samenvoegen van een Fourier-Legendre-serie van het PCT-model met een temporele decorrelatiefunctie van het Random Motion over Ground (RMoG)-model is onderzocht om dit probleem op te lossen. De resultaten toonden een verbetering van de nauwkeurigheid van de hoogteschatting na toepassing van deze wijziging. Het optimaal aantal termen van de Fourier-Legendre-reeks varieerde voor elke pixel. Dit kan worden gebruikt als een indicator van de complexiteit van de vegetatielaag: voor meerlaagse dichte bossen zijn meer termen vereist. Dit hoofdstuk laat zien dat het het aantal onbekende parameters kan worden vergroot door het gebied in verschillende hoogteklassen te segmenteren en het optimale aantal onbekende parameters voor elke klasse te selecteren. Het derde hoofdstuk

richt zich op het verkrijgen van de meest nauwkeurige hoogtekaarten op basis PolInSAR gegevens. Dit is op zichzelf al belangrijk, terwijl hoogte ook dient als de belangrijkste biofysische parameter die bijdraagt aan de schatting van biomassa. Het effect van het minder zwaar maken van de temporele decorrelatie werd onderzocht op nauwkeurigheid bij het bepalen van biomassa. Dit onderzoek ontwikkelde nieuwe allometrische vergelijkingen voor dit doel en testte verschillende regressie strategieën. Dit was een flinke uitdaging vanwege het ontbreken van voldoende veldgegevens. De strategie om een nieuwe allometrische vergelijking te ontwikkelen op basis van alleen hoogte is belangrijk. Een parameter die gewoonlijk tijdens veldwerk wordt gemeten, is H100, d.wz. de gemiddelde basale oppervlakte gewogen gemiddelde van de 10 hoogste bomen binnen een gedefinieerde steekproefplot. Dit hoofdstuk liet zien dat de relatie tussen PolInSAR-hoogte en H100 zwak is, omdat de PolInSAR-hoogte het gemiddelde van de hoogtes binnen de plots schat en de meting niet eenvoudig samenvalt met die van H100. Het vierde hoofdstuk bespreekt hoe je temporele decorrelatie mee kunt nemen in de schatting van boomhoogten. Het richt zich op de gevoeligheid van het voorgestelde gemodificeerde model bij een keuze voor de berekeningsmethode van de complexe coherentie. De basisstap voor het schatten van de hoogte in een van de toegelichte modellen is de selectie van homogene pixels. Om dit te doen, onderscheiden we polarimetrische van polarimetrisch-interferometrische informatie. Door de selectie van pixels mee te nemen, kunnen we rekening houden met gecombineerde fase- en de amplitude-waarden van de pixels. Twee adaptieve methoden zijn gebruikt om statistisch homogene pixels te definiëren. De nauwkeurigheid van van de hoogte nam toe na het toepassen van de adaptieve methoden. Omdat de voorgestelde adaptieve methoden rekenkundig intensiever zijn, is een afweging tussen de gewenste nauwkeurigheid en berekening vereist die vooraf moet gaan aan de selectie van een methode. Samenvattend laat dit proefschrift zien dat de nauwkeurigheid verbeterde van de schatting van de boomhoogte door middel van volledig gepolariseerde InSAR-gegevens die vanaf een vliegtuig zijn opgenomen door de temporele decorrelatie zorgvuldig te behandelen. Dit is wellicht nuttig voor toekomstige SAR-satellietmissies.

Acknowledgments

I would like to thank the European Space Agency for providing data and helping me whenever I faced an obstacle to process the data and getting results. I am also grateful to Dr.Marco Lavalle for providing AfriSAR campaign data as an early access and AfriSAR team at NASA and ESA for organizing and distributing the data acquired during the 2016 AfriSAR Campaign. I also thank the UAVSAR and ISCE teams at the Jet Propulsion Laboratory, California Institute of Technology for collecting and processing the radar images, and the LVIS team at the Goddard Space Flight Center for collecting and processing the lidar data used in this publication.

I would like to thank my fellow doctoral students for their feedback, cooperation and of course friendship. In addition I would like to express my gratitude to the staff of ITC for their support and help during all these years.

I would like to thank my friends for accepting nothing less than excellence from me. Last but not the least, I would like to thank my family: my parents and to my sisters for supporting me spiritually throughout writing this thesis and my life in general.

Contents

List of Figures

List of Tables

List of Nomenclatures

Abbreviations

AGB	Above ground biomass
Caltech	California institute of technology
CDF	Cumulative distribution function
CHM	Canopy height model
DBH	Diameter at breast height
DEM	Digital elevation model
DS	Double similarity
DSM	Digital surface model
ESA	European space agency
FAO	Food and agriculture organization
FP	Fixed point
Interp	Interpolation
JPL	Jet propulsion laboratory
KS–test	Kolmogorov Smirnov test
LiDAR	Light detection and ranging
NASA	National Aeronautics and Space Administration
ONERA	Office National d'Etudes et de Recherches Aérospatiales
OVoG	Oriented volume over ground
PCT	Polarization coherence tomography
PDF	Probability density function
PolInSAR	Polarimetric interferometric SAR
PolSAR	Polarimetric SAR
REDD	Reducing emissions from deforestation and forest degradation
RMoG	Random motion over ground
RMoG_L	Random motion over ground-Legendre
RMSE	Root mean square error
RV	Random volume
RVoG	Random volume over ground
SAR	Synthetic aperture radar
SCR	Signal to clutter ratio
SHP	Statistically homogeneous pixel
SLC	Single look complex

SNR	Signal to noise ratio
SRTM	Shuttle radar topography mission
UAV	Unmanned aerial vehicle
UN	United nations

Symbols

$\alpha_i, i = 1, 2, 3, 4$	Coefficients of fitted polynomial model
α_g	Average backscatter per unit length
$\beta_i, i = 1, 2$	Coefficients of fitted exponential model
γ	Complex coherence
γ_s	Spatial decorrelation
γ_t	Temporal decorrelation
γ_v	Volume decorrelation
γ_{vg}	RVoG model complex coherence
γ_{vt}	Temporal component of the RVoG model
γ_{rvt}	Temporal coherence of the RV model
γ_{gt}	Temporal decorrelation of ground layer
γ_{vt}	Temporal decorrelation of vegetation layer
γ_{M_g}	Complex coherence of the ground layer
γ_M	Complex coherence of RMoG model
γ_{M_L}	Complex coherence of the RMoG$_L$ model
$\delta(.)$	Dirac delta function at z_g
ε	Pre-defined threshold
$\zeta(z, t)$	Structure function of the RMoG model
$\zeta_i, i = 1, 2$	Coefficients of fitted power series
θ, $\delta\theta$	Look angle and local look angle
θ_s	Terrain slope angle
κ_e	Wave extinction factor
λ	Wavelength
μ	Ground-to-volume ratio
ν, ν_g, ν_v	Degradation function of coherence for different layers
φ	Phase element of the PolInSAR images
φ_g	Ground phase
ξ^2	Distance between reference height and calculated height
$\varrho(z)_i, i = 1, 2$	Complex reflection function of two SAR images
ρ	Species-related wood density
ρ_{dv}	Total backscattering per each unit length
ρ_g	Ground scattering per unit length
ρ_{gv}	Ground-to-volume scattering per unit length
$\rho_v(z)$	Structure function of the canopy layer
$\rho(z)$	Structure function
σ_b	Standard deviation of motion
$\sigma(z)$	Radar cross section
τ	texture descriptor
ω_{12}	Correlation matrix of PolInSAR phase
a_n	Legendre coefficients for $n = 0, 1, 2, ...$

∂a	Partial derivative matrix
B	Biomass
B_s	Spatial baseline
C_{11}, C_{22}	Covaraince matrix of two PolInSAR images
card(.)	Cardinality operator
$*$	Complex conjugate transpose
f	Form factor of trees
$f_i, i = 0, 1, 2, ...$	Legendre normalized functions
$f(z')$	Structure function of RMoG$_L$ model
$F(\hat{x})$	Calculated cumulative distribution function
$G(\hat{x})$	hypothesized cumulative distribution function
h, p, D	Parameters of KS-test
h_{CA}	Calculated height for ξ^2 test
h_r	Reference height for RMoG and RMoG$_L$ models
h_{RF}	Reference height for ξ^2 test
h_v	Canopy height
H	Sensor height
k_z	Vertical wave-number
$K_i, i = 1, 2$	Target vector of two SAR images
L	Number of effective looks
$L(z)$	Power loss function after attenuation
$n(z)$	density of the scatterers per unit length
N	Number of trees per hectare
$\|\|.\|\|_F$	Frobenius norm
P_n	Legendre polynomials for $n = 0, 1, 2, ...$
$P, E, andL$	Parameters of generalized extreme value distribution function
Q	Set of statistically homogeneous pixels
R^2	Coefficients of determination
$rect(.)$	Rectangular function for zero backscattering
$S_i, i = 1, 2$	Scattering matrices of two SAR images
t	Temporal baseline
T	Coherency matrix of PolInSAR
(x_p, y_p)	Candidate pixel for SHP selection
X, Y	Initial values of SHP sets
$\mathbf{z}$	Speckle vector
z_g	Ground layer height
$\langle . \rangle$	Expectation operator

1 Introduction

1.1 Background

Synthetic Aperture Radar (SAR) is an imaging method to reconstruct the scattering properties of the Earth's surface in microwave wavelengths. SAR has the ability to operate almost independent of the daylight and weather conditions. Moreover, SAR imaging is sensitive to dielectric and morphological properties of objects and therefore complementary to optical images. After the launch of the first space borne SAR (SeaSat, L-band) by the Jet Propulsion Laboratory, several SAR missions have been operating and some are planned in the near future. A feature of SAR imaging is the ability to retrieve the third dimension of objects from a two-dimensional image. In the past two decades, it has been recognized that multi-polarization, multi-frequency, multi-pass and multi-angle observations have the potential to retrieve the lost dimension and identify the structural properties of objects. Integrating polarimetric and interferometric information makes it possible to retrieve the vertical profile of objects and scattering mechanism are determined.

Using SAR image has been widely done for biomass estimation because of its unique ability to penetrate underlying layers of vegetation cover as well as being independent of weather conditions. In the past several years different methods have been used to estimate biomass from SAR images. These methods can be categorized in four groups: backscatter values, polarimetry, interferometry, and Polarimetric Interferometric SAR (PolInSAR).

During the past years, methods based on backscattering have been frequently used for estimating biomass. These methods, however, are severely affected by limitations like: the problem of registering, the effect of weather conditions and the saturation problem (Zhou et al., 2008). An assessment of estimating biomass using backscatter value has been performed by Fransson et al. (2008). They reported using backscatter value has an insufficient accurate result for estimating biomass.

SAR polarimetry (PolSAR) is the technique of processing and analyzing of multiple polarized waves that are received during SAR imaging. The result of this process yields a matrix instead of a scalar that is typical for the single channel SAR. The advantage of polarimetry is the ability to identify the scattering mechanisms and decompose the complex scattering from objects into elementary scattering processes. This is useful for detection, segmentation, classification and solving inverse problems (Cloude and Pottier, 1996; Lee and Pottier, 2009).

A comprehensive evaluation of using SAR interferometry and phase information in forest biophysical parameter estimation has been performed by (Balzter et al., 2007). They evaluated the accuracy of canopy height retrieval and biomass estimation using SAR interferometry in different test sites and different SAR sensors. They concluded that multi-band and multi-polarimteric information are necessary to overcome the problems of interferometry in estimating biomass.

The application of PolInSAR in forest studies has been further considered after the launch of Terra-SAR-X and TanDEM-X satellites. With these sensors, the multi-pass SAR data in many parts of the world is available for research purposes. PolInSAR makes it possible to retrieve accurate height estimation in forest areas. The results showed a high correlation ($R^2 \geq 0.7$) with LiDAR DSM. The height estimation accuracy is reported to be equal to about 80-90% by most of the researchers (Mette et al., 2004; Balzter et al., 2007; Garestier et al., 2008; Neumann et al., 2010; Hajnsek et al., 2016).

The allometric equations which use height information for estimating biomass leads to accurate biomass estimation especially in tropical and temperate forests. Thus it is a good solution to extract height information using PolInSAR and use it as an input for allometric equations. Since the longer wavelengths have deeper penetration into vegetation layers, the P- and L-bands are the most selected bands for height retrieval. Moreover, these bands have been combined with X-band to extract Digital Surface Model (DSM) of the forests.

To retrieve height from PolInSAR, the main observation is the scattering matrix. We can obtain the complex coherence for each polarization from the scattering matrix. These matrices are defined as the combination of both real (amplitude) and imaginary (phase) components of the signal and fall within the unit circle of the complex plane (Cloude, 2005). As a physical interpretation, coherence shows the homogeneity of an area. Estimating coherence is the basic step in PolInSAR and estimating vertical structure of the objects as it can be performed by different approaches is discussed in Chapter 6.

Various phenomena lead to the reduction of coherence. This effect is called "decorrelation" and it is a severe limitation of using PolInSAR. The decorrelation sources can be categorized as systematic noise (thermal decorrelation), changes in the imaging scene according to the difference in image acquisition times (temporal decorrelation), errors in image registration, un-focusing, and decorrelation due to the baseline (geometric decorrelation). The thermal and system related decorrelations can be taken under control. An example of handling thermal decorrelation and other systematic errors is described in Touzi et al. (1999) and for geometric decorrelation and un-focusing a good explanation is provided by Neumann et al. (2010); Treuhaft and Siqueira (2000). The first two sources however have been considered to be unsolvable for a long time, hence making interferometry almost inapplicable in vegetated areas. Several studies confirmed that application of PolInSAR to satellite images is limited mainly because of the temporal decorrelation.

It is caused by temperature variation, change of direction of backscattering components and changing of moisture content during the time interval between two images that can vary between minutes and months (Papathanassiou and Cloude, 2003; Zhou et al., 2008; Lee and Pottier, 2009). This is not a constant value but depends upon the height of the trees and movements of objects caused by wind. In longer time intervals, the variation of moisture content and clear cutting trees may cause larger errors. In order to achieve best possible accuracy using PolInSAR, one should find a way to handle the main sources of errors. Moreover, the use of multi-baseline PolInSAR has been examined for forest height estimation recently (Florian et al., 2006; Li et al., 2014; Huang et al., 2011). Although using multi-baseline PolInSAR can improve the accuracy of height retrieval, one must find a solution for the errors caused by signal side lobes and phase ambiguity as well as decorrelation sources(Bamler and Hartl, 1998).

In the reviewed research papers (Mette et al., 2004; Balzter et al., 2007; Garestier et al., 2008; Hajnsek et al., 2016) it is reported that while thermal noise and geometric decorrelation can be removed when generating a height map for vegetated areas, temporal decorrelation is difficult to be estimated. Up to now has been the major limitation of PolInSAR especially in forests (Cloude and Papathanassiou, 2003). A few methods have been developed to handle the temporal decorrelation in PolInSAR.

When using airborne images, usually a few extra images with zero spatial baseline are captured and these images are used for removing temporal decorrelation from other images. This method is not applicable for already acquired images, it is time and money consuming, and does not lead to accurate results. Hence, it has been tried to develop analytical methods to mitigate temporal decorrelation. The first method was introduced by Zebker and Villasenor (1992). They characterized various decorrelation sources in SAR echoes and separated the term which was related to temporal changes of scatterers. This method was specifically developed for vegetated areas with the assumption that movement of scatterers is larger in the vertical direction. They tested it on repeat-pass single channel L-band SAR images from SeaSat successfully. This method was later extended to include Brownian motion of scatterers and was tested and validated with airborne L-band data by Neumann et al. (2010). An assumption to model the effects of wind in forest areas was proposed in Lavalle and Hensley (2015). They assumed that the movement of backscattering components is different in the vertical direction of the vegetation layer (Lavalle, 2009; Lavalle et al., 2010, 2012; Lavalle and Hensley, 2015). Their method was called the Random-Motion-over-Ground (RMoG) model and was tested on single-baseline UAVSAR and airborne SAR L-band data (Lavalle et al., 2012; Lavalle and Khun, 2014).

The RMoG model is a recent and complete model for handling temporal decorrelation in forest areas. The basis of this model is similar to the one described in Zebker and Villasenor (1992). The proposed model in Lavalle et al. (2012) combines “Random Volume (RV)” and “Random Volume over Ground (RVoG)” scattering function. In RV backscattering model the forest is considered as randomly located backscattering components (Cloude and Papathanassiou, 2003). In the RV model no ground backscattering is included, whereas the RVoG model includes both volumetric and ground backscattering. The RVoG model assumes that the dominated backscattering mechanism is from the canopy layer and the backscattering from underlying layer is such small that can be ignored. Different studies have shown that this basic assumption is far from the real scattering mechanism in most vegetated areas (Treuhaft and Siqueira, 2000; Cloude, 2007a; Garestier et al., 2008).

There are alternative models to retrieve vertical structure. One of these models is described in Treuhaft and Siqueira (2000), and Garestier et al. (2008). The next alternative was suggested in Cloude (2006, 2007a). They developed a model based upon Fourier-Legendre series and tested it in a radar chamber. The test was later applied on SAR airborne images as well, and the result showed that the vertical reconstruction obtained by the

Fourier-Legendre series best coincides with measurement in the chamber.

The temporal coherence model developed in Lavalle et al. (2012) is the most complete model for temporal decorrelation up to now. However, it has been built on the RVoG model. It would be of interest to see if we can change the temporal decorrelation model and employ more accurate structure function for the canopy reconstruction. By applying this change, we expect to increase the height estimation accuracy and consequently the biomass estimation accuracy.

1.2 Problem statement

The main problem statement addressed in this research is: “Does improving the structure function approximation along with taking into account temporal decorrelation increase tree height and consequently biomass estimation accuracy?”. The main problem statement is divided into four specified problems used to structure research questions and objectives. These specified problems are:

1. **General structure function for all vegetation types in temporal decorrelation modeling**
   Temporal decorrelation is a main source of error that has been considered mainly after the introduction of new polarimteric interferometric images. It has been subject of a few important recent studies. One of the most recent models for dealing with temporal decorrelation is the RMoG model which is developed based on one of the analytical scattering models, namely the RVoG model. The RVoG backscattering model is inadequate in modeling backscattering in forest areas especially in tropical and heterogeneous dense forests. Therefore exploring the possibilities of improving tree height estimation in the presence of temporal decorrelation is required. This can be done by using more accurate backscattering scenarios. In the literature, modeling the vertical structure by applying Fourier-Legendre series is recommended. In practice, however, this has not been used along with temporal decorrelation models. Additionally, it is not clear how this can affect the forest height estimation accuracy. This could be explored to potentially improve the height estimation accuracy in forested areas using PolInSAR data. Moreover, it is unclear how many terms of the Fourier-Legendre series should be selected to have a trade-off between vertical reconstruction accuracy and number of unknown parameters. Thus it should have been investigated as well.
2. **Tackling temporal decorrelation in SAR tomography**
   SAR tomography has been proposed and developed for reconstructing vertical profiles with high level details. It is similar to PolInSAR with the difference that the synthetic aperture is rebuilt in the vertical direction using multiple SAR images. A well-studied model for processing tomographic data is the Polarimetric Coherence Tomography (PCT) model. Results of the PCT model are more accurate than using single-baseline PolInSAR, although temporal decorrelation is ignored. It leads

to biased height estimation especially in tropical forests that have much interaction between vegetation and ground, whereas the forest has multiple layers. Most literature suggests to take into account the temporal decorrelation using a separate procedure that doubles the computational time or acquire extra images with zero spatial baseline. Both ways, however, are inefficient and even often impossible. Thus, modifying the PCT model and adding the temporal decorrelation component to the structure function can potentially improve the height estimation accuracy without the need to add extra steps to data capturing and analysis.

3. **Effect of biased height mapping on biomass estimation accuracy**
A major purpose for mapping forest height is to use it as an estimator for Above Ground Biomass (AGB). It has been shown in the literature that tree height has a strong and positive correlation with the total AGB. Remote sensing and especially PolInSAR has been employed to estimate biomass via obtaining height maps. The effect of ignoring temporal decorrelation and the resulting bias, however, is unknown. This is an important issue since some future satellite missions like BIOMASS are aimed to provide biomass maps of forests in a global scale. Thus, the major sources of errors in obtaining biomass and their contribution to the final products should be studied. Therefore, the next step after developing a modified model for estimating height for single- and multi-baseline SAR images should be exploring the effect on biomass estimation accuracy. After examining the impact of taking temporal decorrelation into account, we can determine how the modified model should be applied on the current and future PolInSAR and tomographic SAR data. The tomographic SAR data is the set of images captured to extend the SAR aperture in vertical direction as to reconstruct the vertical structure.

4. **Sensitivity of height estimation accuracy to the choice of coherence estimation method**
Most PolInSAR and tomoSAR applications are based upon complex coherence. Conventionally, complex coherence is estimated by first defining a constant neighborhood then, averaging the magnitude of the pixels inside that neighborhood. This method assumes stationarity, i.e. the neighboring pixels are characterized by the same scattering mechanism. In addition, most averaging methods only use polarimetric information content. It has been shown that in case of PolInSAR, some pixels may have similar polarimetric signature but totally different phase elements (Vasile et al., 2010). This means that they can not be considered as homogeneous pixels. Recently, some studies have concentrated on developing new methods which use both magnitude and phase elements in defining the statistically homogeneous pixels. These methods, however, have not been sufficiently explored to make clear how they affect the height and consequently biomass estimation accuracy. The computational costs and time are another issue that

should be considered when applying these methods for obtaining coherence since it is a challenge to optimize more elaborated methods for big datasets. Sensitivity of height estimation accuracy to adaptive coherence obtaining methods should be investigated.

After addressing these problems the tree height estimation accuracy by single- and multi-baseline SAR images should improve, resulting into more accurate forest AGB estimation.

1.3 Research objectives and questions

This PhD dissertation focuses on tackling temporal decorrelation and its impact on forest height and biomass estimation accuracy. The specified objectives are:

1. **First Objective** To explore the possibilities of improving temporal decorrelation modeling by using a more accurate backscattering scenario.
   RVoG backscattering scenario has been shown to be inadequate in modeling backscattering in forest areas. The suggested backscattering scenario for this purpose is the Fourier-Legendre Legendre model. It is hypothesized that using a more accurate backscattering model will increase the accuracy of temporal decorrelation model. To test this hypothesis, the Gaussian function of the RVoG model has been substituted with a finite number of terms of the Fourier-Legendre series. P-band images acquired from a boreal forest area has been selected to apply the new modified model. The height estimation accuracy of the new model is compared with the conventional RVoG and RMoG models and the Lidar height map. This objective tries to answer the research question: “Can using a more accurate structure function improve height estimation accuracy by PolInSAR?”

2. **Second Objective** To modify the PCT model and combine it with temporal decorrelation scenario for processing tomographic SAR data. This objective modifies the PCT model to include temporal decorrelation. It focuses on combining the structure function, which is a finite number of Fourier-Legendre series, and the movement of scatterers in vertical direction. Since it will increase the number of unknown parameters there should be a new strategy to solve the equation system. Additionally, the cost-benefit analysis should be done to determine number of terms in vertical structure function which defines the reconstruction detail. This modification was exploited on a Single-Look-Complex (SLC) tomographic data of a tropical, dense and multi-layer forest in Africa. Moreover, the height estimation accuracy after this modification was compared to the conventional PCT model and with a Lidar height map. In the second objective the following research questions will be addressed: “How can the PCT model be modified to mitigate for temporal decorrelation caused by objects movements in

vertical direction? How many terms are needed to make a trade-off between vertical reconstruction detail and the number of model parameters to be estimated?"

3. **Third Objective** To exploit the effect of taking into account temporal decorrelation in height estimation modeling on biomass mapping accuracy.
   This objective aims to examine the impact of compensation of temporal decorrelation described in previous objectives on biomass mapping. For this purpose, the conventional RVoG, RMoG and the new proposed modified model are applied on single-baseline PolInSAR from a boreal forest located in Sweden. Resulting height maps are converted into biomass. For obtaining biomass by other biophysical parameters i.e. height in this case, allometric equations are required. Developing such equations involves regression analysis. In this objective, the average biomass available from extensive field work is the dependent variable and height is the independent one. Different regression methods have been examined to find the most accurate and efficient one. Accuracy of estimated biomass by the RVoG, RMoG and the new proposed modified models are compared to each other and the measured biomass. The third objective attempts to answer following research questions: "Is biomass estimation accuracy affected by mitigation of temporal decorrelation and if the answer is yes, how much?".

4. **Fourth Objective** To assess sensitivity of PolInSAR height estimation models to different methods of obtaining the complex coherence.
   The fourth objective is to explore the sensitivity of height estimation accuracy to the chosen complex coherence obtaining method. To do this, the conventional averaging method for defining the spatial averaging window is examined first. Moreover, the adaptive methods proposed in my previous studies have been implemented. These adaptive methods take into account not only polarimetric information, but also the phase element. In this way, the window would not be the simple rectangular shape, but it can differ in terms of pixel number and geometrical shape. Applying adaptive methods, however, requires heavy computation and more time. Thus, the improvement in height estimation should be balanced with the chosen coherence derivation method. The fourth objective aims to reply to these research questions: "What is the dependency of height estimation accuracy on the complex coherence estimation method? Does it pay off to invest on using adaptive methods for estimating complex coherence in combination with elaborated PolInSAR height estimation models?"

1.4 Thesis outline

This thesis is structured into seven chapters. In addition to the introduction, theoretical background and synthesis chapters the four technical chapters which focus on the above objectives. They are based on ISI journal articles and conference papers that are published or under review currently.

- **Chapter 1** presents the general introduction to the thesis. It summarizes the importance of taking into account the temporal decorrelation as a source of error in PolInSAR height estimation. Based on this the research objectives and research questions are introduced.
- **Chapter 2** introduces the theoretical background for the methodology used through the thesis.
- **Chapter 3** gives the modified height estimation model which compensates for temporal decorrelation. It evaluates the height estimation accuracy by applying the new developed model on PolInSAR images.
- **Chapter 4** presents the extension of the modified height estimation model to multi-baseline SAR data. It modifies the PCT for processing tomographic data with mitigation of temporal decorrelation.
- **Chapter 5** introduces the assessment of biomass estimation accuracy using only obtained vegetation height by mean of PolInSAR. It also presents new allometric equation for biomass estimation from tree height.
- **Chapter 6** gives the analysis results of sensitivity of tree height estimation accuracy to the complex coherence obtaining method. It compares the conventionally used methods with adaptive ones for selecting homogeneous pixels.
- **Chapter 7** summarizes the results from the research and supplies answers to the research questions described in the introduction section. Reflection on the conclusions is explained and recommendations for future research are provided.

2 Theoretical background

2.1 Introduction

This chapter presents the theoretical background used throughout the dissertation. Section 2.2 explains the PolInSAR and how it is used to acquire structural information on the canopy. Section 2.3 and 2.4 describe the spatial and temporal decorrelation concepts. Additionally, derivation of temporal decorrelation model and how to combine it with the RVoG model is provided. Modifying this temporal decorrelation to reconstruct the vertical profile more accurately and combine it with Brownian motion scenario is the topic of Chapter 3. Its extension to tomographic SAR and estimating biomass are the focus of Chapter 4 and 5 respectively. The effect of changing the input of the temporal decorrelation model and the modified version is then discussed in Chapter 6.

2.2 Polarimetric SAR interferometry (PolInSAR)

For a fully polarimetric coherent radar system that observes the objects from two slightly different positions with look angles θ and $\theta + \Delta\theta$, the geometrical scenario is displayed in Figure 2.1.

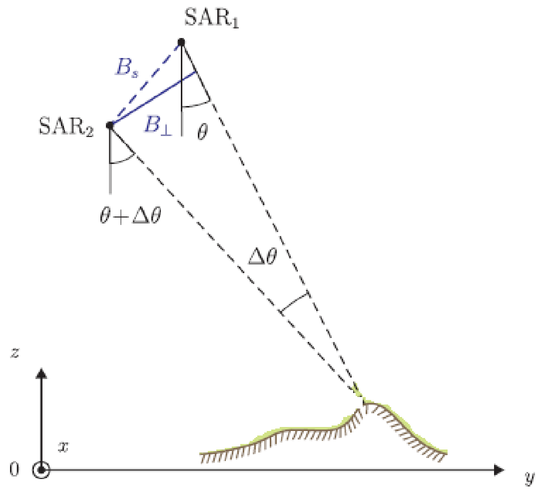

Figure 2.1: Geometrical representation of SAR interferometry

In Figure 2.1, B_s is the distance between two acquisition points and is named spatial baseline, $B_\perp$ is the projection of spatial baseline on the slant range. If the observations are acquired simultaneously, it is called single-pass interferometry and otherwise, it is named repeat-pass interferometry. In the latter case, there is a temporal baseline between two acquisitions that can be shown by two matrices S_1 and S_2. The matrices are related to the backscattered energy from the scene and under reciprocity condition, they are symmetric, i.e. $S_{HV_i} = S_{VH_i}, i = 1, 2$. Here, H stands for horizontal and

V stands for vertical polarizations. For separation of scattering mechanisms , a handy way is to vectorize them. For this purpose, we need to select a basis. A common choice is the three-dimensional Pauli basis, where the target vector $K_i, i = 1, 2$ of each matrix equals

$$K_i = \frac{1}{\sqrt{2}} \left(S_{hh_i} + S_{vv_i}, S_{hh_i} - S_{vv_i}, 2S_{hv_i}\right)^t, \tag{2.1}$$

where ^{t} is the transpose, $i = 1, 2$ and the elements reflect canonical scattering mechanisms (Cloude and Pottier, 1996). For selecting the scattering mechanism, generally, a projection vector w is used that represents the scattering properties related to the polarimetric interferometer. The scattering matrices can be presented as

$$S_i = {w_i}^{*t} K_i, i = 1, 2. \tag{2.2}$$

Matrices $S_i, i = 1, 2$ are the main elements of PolInSAR as the polarimetric properties are reflected in w_i and the interferometric properties are represented by two repeating observations, S_1 and S_2. S_i is distributed as a circular Gaussian matrix. The degree of coherence γ, between two observations, represents the synergy of the polarimetric and interferometric properties. An estimator of γ value is obtained by

$$\gamma = |\gamma| \exp(j\varphi) = \frac{\langle S_1 S_2^* \rangle}{\sqrt{\langle S_1 S_1^* \rangle \langle S_2 S_2^* \rangle}}. \tag{2.3}$$

Here, $0 \leq |\gamma| \leq 1$, $-\pi \leq \varphi \leq \pi$, and $\langle . \rangle$ is expectation. Assuming ergodicity which means that spatial and temporal averaging lead to identical result, it can be estimated by averaging over a spatial ensemble. Reliability of estimating γ depends on the used averaging method. Several methods have been explored for this purpose (Lee and Pottier, 2009) and Chapter 6 in this dissertation has been dedicated to this aspect.

PolInSAR relates γ to the characteristics of the objects, in our case, the forest. The value of the γ depends on many factors namely, decorrelation sources (Zebker and Villasenor, 1992). In absence of these factors, $\gamma = 1$, otherwise these decorrelation factors should be estimated to obtain γ value. The effect of these factors reduces γ. Decorrelation sources are usually modeled as multiplicative factors that affect both the magnitude and phase of γ. These multiplicative factors can be identified according to their origin and listed as:

1. Scattering decorrelation which is related to the geometry of the observation and time interval between repeating image;
2. Atmospheric decorrelation that is mostly affecting lower frequencies, i.e. P- and L-bands;
3. Decorrelation caused by the system like thermal noise, calibration, and co-registration errors, and sampling bias (Lee et al., 1999).

The most important sources of decorrelation for estimating height by PolInSAR are spatial decorrelation γ_s, temporal decorrelation γ_t, and system decorrelation γ_{snr}. The first two decorrelation sources belong to the first category explained before whereas the system noise decorrelation belongs to the last one. Considering these three sources are known in every polarization, γ can be estimated as

$$\gamma = \gamma_s \gamma_t \gamma_{snr}. \tag{2.4}$$

Estimating these sources is the main objective in PolInSAR (Cloude, 2010). Assuming the known signal-to-noise ratio (SNR) of the SAR system, γ_{snr} that is a real-value decorrelation and impacts the magnitude of γ, equals

$$\gamma_{snr} = \frac{1}{1 + SNR^{-1}}. \tag{2.5}$$

The typical value of γ_{snr} is small comparing to the other sources of decorrelations (Zebker and Villasenor, 1992; Bamler and Hartl, 1998).
Spatial and temporal sources are related to the structure of the objects and thus are the most important to estimate. The value of these two sources is affected by the selected scattering mechanism and the scene characteristics. For example, if the observed forest is semi-transparent to the SAR signal, the spatial correlation becomes larger. Temporal decorrelation depends on the dynamic changes of the objects caused by weather condition and seasonal changes. Elaborating the models for spatial and temporal correlation is the main focus of this dissertation and the following sections.

2.3 Spatial correlation model

Let us consider the objects as vertically aligned scatterers, thus the interferometric coherence should be derived for such geometrical shapes. According to Treuhaft and Siqueira (2000), total spatial correlation of such scatterers is expressed as the sum of correlation among pairs of small units of d_z in the vertical direction and estimated as

$$\gamma_s = \frac{\int \langle \varrho_1(z)\varrho_2(z)^* \rangle dz}{\sqrt{\int \langle \varrho_1(z)\varrho_1(z)^* \rangle \langle \varrho_2(z)\varrho_2(z)^* \rangle dz}}. \tag{2.6}$$

here, $\varrho(z)_i, i = 1, 2$ represents the complex reflection for each length unit and has the dimension of $\mathrm{dBm}^{-0.5}$, $\langle . \rangle$ is the averaging over the spatial ensemble, and the integral range extends from the ground to the top of the canopy layer. For the objects that are observed from two slightly different positions, the relation between $\varrho_2(z)$ and $\varrho_1(z)$ is expressed as

$$\varrho_2(z) = \varrho_1(z) \exp(-jk_z z), \tag{2.7}$$

where, $k_z = \frac{4\pi\Delta\theta}{\lambda \sin\theta}$ is called vertical wave-number and depends on the system properties and observation geometry. Thus the spatial correlation equals

$$\gamma_s = \frac{\int \langle \varrho_1(z)\varrho_1(z)^* \rangle \exp(jk_z z) dz}{\int \langle \varrho_1(z)\varrho_1(z)^* \rangle dz} = \frac{\int \rho(z) \exp(jk_z z) dz}{\int \rho(z) dz}. \tag{2.8}$$

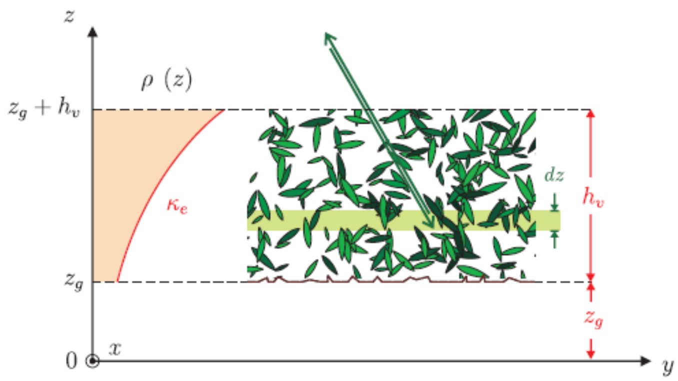

Figure 2.2: Simplified representation of the vegetation layer as we assume in RV model.

Here, $\rho(z) = \langle|\varrho_1(z)^2|\rangle$ is called the structure function and models the average received backscatter from each length unit of the object. Information on the geometry, position and backscattering properties of the object is mixed in the structure function. Determining the structure function is discussed throughout this dissertation and has been investigated broadly in tomographic SAR studies (Reigber and Moreira, 2000; Cloude, 2006).

To obtain function $\rho(z)$ in the closed form for forests, we assume the vegetation layer consists of randomly oriented objects that are located on top of a rough surface as shown in Figure 2.2. For modeling this layer, we assume there is no surface below the vegetation. This model is called Random Volume (RV) and is characterized by h_v which is the thickness of the volume layer, $n(z)$ that is the density of the scatterers per unit length, and radar cross section $\sigma_s(z)$. Both $\sigma_s(z)$ and $n(z)$ depend on the depth of the signal penetration. Generally, the function $\rho(z)$ is estimated as

$$\rho(z) = n(z)\sigma_s(z)L(z), \tag{2.9}$$

where $L(z)$ defines how much is the power loss after attenuation through the canopy layer. Assuming homogeneity of the canopy layer i.e. $\sigma_s(z)$ and $n(z)$ are constant values within $z_g \leq z \leq z_g + h_v$ range then

$$n(z)\sigma_s(z) = \rho_{dv}\mathrm{rect}\left(\frac{z - z_g - \frac{h_v}{2}}{h_v}\right), \tag{2.10}$$

and

$$L(z) = \exp\left(\frac{2\kappa_e}{\cos\theta}\,(z - z_g - h_v)\right). \tag{2.11}$$

Here, ρ_{vd} defines the total backscattering for each unit length of the canopy layer and function rect(.) represents zero backscattering outside of the vegetation layer. After substituting $L(z)$ into (2.9), the structure function of the RV model is obtained as

$$\rho_v(z) = \rho_{dv} \exp\left(\frac{2\kappa_e}{\cos\theta}(z - z_g - h_v)\right), \qquad z_g \leq z \leq z_g + h_v. \tag{2.12}$$

Thus the numerator of (2.8) in the closed form is obtained by

$$\begin{aligned}
&\int_{z_g}^{z_g+h_v} \rho_{dv} \exp\left(\frac{2\kappa_e}{\cos\theta}(z - z_g - h_v)\right) \exp(jk_z z) dz \\
&= \rho_{dv} \exp(jk_z z_g) \exp\left(-\frac{2\kappa_e}{\cos\theta} h_v\right) \frac{\exp\left(\frac{2\kappa_e}{\cos\theta}\right) h_v - 1}{\frac{2\kappa_e}{\cos\theta} + jk_z},
\end{aligned} \tag{2.13}$$

whereas $\sigma_s(z)$ that represents the total backscatter equals

$$\begin{aligned}
\sigma_s(z) =& \int_{z_g}^{z_g+h_v} \rho_{dv} \exp\left(\frac{2\kappa_e}{\cos\theta}(z - z_g - h_v)\right) dz \\
=& \rho_{dv} \frac{\cos\theta}{2\kappa_e}\left(1 - \exp\left(-\frac{2\kappa_e}{\cos\theta} h_v\right)\right).
\end{aligned} \tag{2.14}$$

Thus the spatial correlation of the γ_v that is defined for the canopy layer with the structure function of $\rho_v(z)$ can be expressed as

$$\begin{aligned}
\gamma_v(z) =& \frac{\int \rho_v(z) \exp(jk_z z) dz}{\int \rho_v(z) dz} \\
=& \exp(jk_z z_g) \frac{\frac{2\kappa_e}{\cos\theta}}{\frac{2\kappa_e}{\cos\theta} + jk_z} \frac{\exp\left(\frac{2\kappa_e}{\cos\theta} + jk_z\right) h_v - 1}{\exp\left(\frac{2\kappa_e}{\cos\theta}\right) h_v - 1}.
\end{aligned} \tag{2.15}$$

Assuming $P_1 = \frac{2\kappa_e}{\cos\theta}$ and $P_2 = \frac{2\kappa_e}{\cos\theta} + jk_z$, γ_v can be re-formulated as

$$\gamma_v = \exp(j\varphi_g) \frac{P_1(\exp(P_2 h_v) - 1)}{P_2(\exp(P_1 h_v) - 1)}, \tag{2.16}$$

where $\varphi_g = k_z z_g$ is the ground phase. According to (2.16) the coherence magnitude reaches its maximum when $\kappa_e = 0$ and the phase center has its minimum when $h_v = 0$. Additionally, when κ_e increases, the wave penetration decreases and volume correlation is higher and consequently, the phase center elevates.

In the RVoG model scenario as shown in Figure 2.3 a rough surface is assumed to be located at $z = z_g$ where z_g is the height of ground layer. Thus the structure function needs two more parameters which are attenuated from the surface and from the interaction between surface and canopy layer. Assuming $z_g < z \leq z_g + h_v$ then

$$\begin{aligned}
\rho_{vg}(z) =& (\rho_g + \rho_{vg}) \exp\left(-\frac{2\kappa_e}{\cos\theta} h_v\right) \delta(z - z_g) \\
&+ \rho_v \exp\left(\frac{2\kappa_e}{\cos\theta}(z - z_g - h_v)\right).
\end{aligned} \tag{2.17}$$

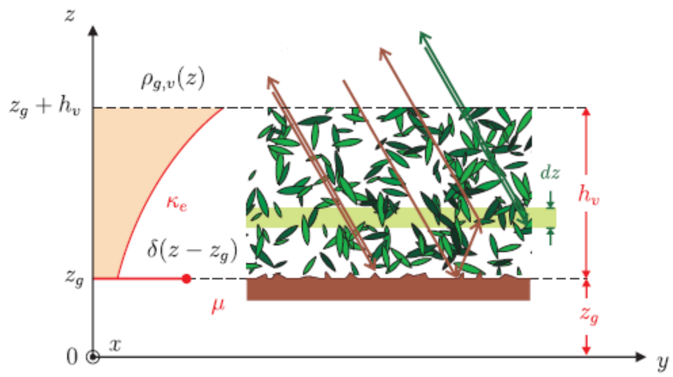

Figure 2.3: Simplified representation of the vegetation layer as we assume in RVoG model.

Here, ρ_g and ρ_{gv} are the ground and ground-to-volume scattering per unit length and $\delta(.)$ is the Dirac delta function located at $z = z_g$. Function ρ_g represents the ground and volume layer characteristics and is obtained similarly by (2.9) and (2.10). After substituting (2.17) into (2.8) the complex coherence for the RVoG model γ_{gv} equals

$$\begin{aligned}\gamma_{gv} &= \exp(jk_z z_g)\frac{\sigma_g + \sigma_{vg} + \rho_v \exp(-P_1 h_v)(\exp(P_2 h_v) - 1)/P_2}{\sigma_g + \sigma_{vg} + \rho_v(1 - \exp(-P_1 h_v))/P_1} \\ &= \exp(j_z z_g)\frac{\mu + \gamma_v \exp(-jk_z z_g)}{\mu + 1}.\end{aligned} \tag{2.18}$$

Here, μ is a real-valued parameter and represents ground-to-volume scattering ratio and obtained as

$$\mu = \frac{\sigma_g + \sigma_{gv}}{\sigma_v} = \frac{\sigma_g + \sigma_{gv}}{\rho_{vg}\frac{\cos\theta}{2\kappa_e}\left(1 - \exp\left(-\frac{2\kappa_e}{\cos\theta}h_v\right)\right)}, \tag{2.19}$$

where the numerator is the ground and ground-to-volume scattering and the denominator is the volume scattering. According to (2.18), the complex coherence for the RVoG model is defined based on four real-values parameters i.e. z_g, h_v that shows the structure of vegetation layer and κ_e, and μ that depend on the geometry of the sensor and dielectric constant of the canopy. We should notice that μ is dependent on the polarization and consequently the effect of polarization on the complex coherence reveals in μ. If $\mu >> 1$ the volume correlation becomes negligible and it happens in case of direct scattering from the ground layer only. Figure 2.4 displays the changing attitude of RVoG coherence phase and magnitude versus varying μ values.

As Figure 2.4 implies, coherence magnitude does not decrease constantly by increasing ground-to-volume ratio. It decreases up to a minimum value that depends on the mean value of κ_e value. This implies that there is no direct way for maximization of coherence magnitude by polarization selection.

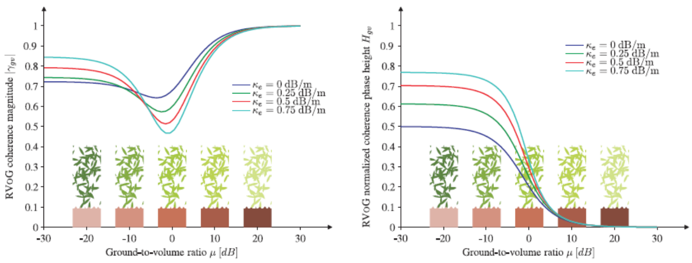

Figure 2.4: Magnitude and phase of RVoG coherence against varying μ values (Lavalle, 2009).

To demonstrate a geometrical interpretation of the RVoG model, we assume $m = \frac{\mu}{\mu+1}$ where $0 \leq m < 1$, thus RVoG coherence equals

$$\begin{aligned}\gamma_{vg} &= \exp\left(jk_z z_g\right) \frac{\mu + \gamma_v \exp\left(-jk_z z_g\right)}{\mu + 1} \\ &= \exp\left(j\varphi_g\right) \left[\gamma_v \exp\left(-j\varphi_g\right) + m\left(1 - \gamma_v \exp\left(-j\varphi_g\right)\right)\right].\end{aligned} \tag{2.20}$$

Equation (2.20) can be interpreted as the equation of a straight line on a the complex plain where the axis are the real and imaginary component of the γ_{gv} respectively. This geometrical interpretation has been validated and tested in several studies as discussed in Chapter 1.

2.4 Temporal correlation model

The temporal decorrelation is usually accounted by multiplying the volume correlation by a constant factor (Papathanassiou and Cloude, 2003). Another way is based on dividing the temporal decorrelation into the ground and volume components. Both components are assumed to have real values and usually, the ground component is removed due to the stability of the ground layer in short time intervals. The temporal component of the canopy layer as γ_{vt}, it can be defined as the sum of scatterers movements in the time interval between acquisition times. The motion can be approximated as

$$\gamma_{vt} = \exp\left(-\frac{t}{\nu}\right), \qquad \nu = \frac{2}{{\sigma_b}^2}\left(\frac{\lambda}{4\pi}\right). \tag{2.21}$$

Here, t is the temporal baseline, σ_b is the standard deviation expressed in $\sqrt{\frac{\mathrm{m}}{\mathrm{day}}}$ and ν represents the degradation of coherence over time expressed in day unit (Rocca, 2007). Equation (2.21) implies that coherence decreases over time and with increasing the scatterers motions and system wavelength. As an improvement to modeling temporal decorrelation, a new temporal correlation function was proposed by Lavalle and Hensley (2015). In this model, the vertical movement of scatterers is considered in the vertical direction of the

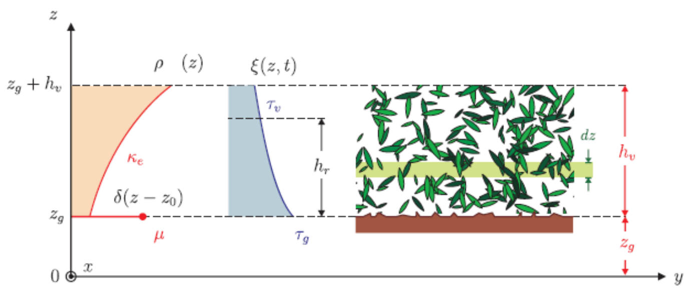

Figure 2.5: Representation of the new structure function $\xi(z,t)$. Parameters of (2.18) are displayed.

vegetation layer. The complex coherence including temporal decorrelation function is defined as

$$\gamma_{vt} = \exp{(j\varphi_g)} \frac{\int_0^{h_v} \rho(z)\xi(z,t)\exp{(jk_z z)}dz}{\int_0^{h_v} \rho(z)dz}, \tag{2.22}$$

where $\xi(z,t)$ is the modified structure function that accounts for the scatterers movements. To define $\xi(z,t)$ we assume the motion is a continuous function that increases when z increases from ground level to the top of the canopy. Thus $\xi(z,t)$ can be obtained by

$$\xi(z,t) = \exp\left(-\frac{t}{\nu(z)}\right). \tag{2.23}$$

Hypothetically, the motion has a linear trend from bottom to the top along the vertical direction of the canopy layer and the $\nu(z)$ becomes (Lavalle and Hensley, 2015)

$$\frac{1}{\nu(z)} = \frac{1}{2}\left(\frac{4\pi}{\lambda}\right)^2 \left[\sigma_{bg}^2 + \left(\sigma_{bv}^2 - \sigma_{bg}^2\right)\frac{z}{h_r}\right] = \frac{1}{\nu_g} + \left(\frac{1}{\nu_v} - \frac{1}{\nu_g}\right)\frac{z}{h_r}. \tag{2.24}$$

Here, σ_{bg} and σ_{bv} are motion standard deviation per day for ground and canopy layers, h_r is the reference height and ν_g and ν_v are time function with the condition that $\nu_g \geq \nu_v$. The hypothesis of linear function in (2.24) should be verified experimentally. Substituting (2.24) into (2.23) we obtain

$$\xi(z,t) = \exp\left(\frac{t}{\nu_g} - \left(\frac{t}{\nu_v} - \frac{t}{\nu_g}\right)\frac{z}{h_r}\right), \qquad \nu_g \geq \nu_v. \tag{2.25}$$

In case of zero temporal baseline i.e. $t = 0$ from (2.25) we obtain $\xi(z,t) = 1$. The value of the temporal motion value is smallest at $z = 0$ and increases with higher z values. Figure 2.5 shows a simplified representation of the modified structure function.

After substituting (2.25) into (2.22), the new equation for complex coherence accounting for temporal decorrelation, γ_{vt}, equals

$$\gamma_{vt} = \exp{(j\varphi_g)} \frac{\int_0^{h_v} \rho(z)\exp\left(\frac{t}{\nu_g} - \left(\frac{t}{\nu_v} - \frac{t}{\nu_g}\right)\frac{z}{h_v}\right)\exp{(jk_z z)}dz}{\int_0^{h_v} \rho(z)dz}. \tag{2.26}$$

Here, ν_g and ν_v stand for temporal decorrelation of the scatterers. By combining (2.25) and (2.22), the temporal decorrelation version of the RV model is obtained by

$$\begin{aligned}\gamma_{rvt} =& \exp\left(j\varphi_g\right)\frac{2\kappa_e \exp\left(-\frac{t}{\nu_g}\right)}{\cos\theta\left(\exp\left(\frac{2\kappa_e h_v}{\cos\theta}\right)-1\right)}\times \\ &\int_0^{h_v} \exp\left(\frac{2\kappa_e}{\cos\theta}\right)\exp\left(-\left(\frac{t}{\nu_v}-\frac{t}{\nu_g}\right)\right)\frac{z}{h_r}\exp\left(jk_z z\right)dz,\end{aligned} \tag{2.27}$$

where γ_{rvt} is similar to (2.8) with the difference of accounting for temporal decorrelation. Defining $P_1 = \frac{2\kappa_e}{\cos\theta}$, $P_2 = \frac{2\kappa_e}{\cos\theta} + jk_z$, and $P_3 = -\frac{1}{h_r}\left(\frac{t}{\nu_v} - \frac{t}{\nu_g}\right)$ the temporally decorrelated complex coherence of the RV model γ_{rvt} is represented as

$$\gamma_{rvt} = \exp\left(j\varphi_g\right)\exp\left(-\frac{t}{\nu_g}\right)\frac{P_1\left(\exp\left((P_2+P_3)h_v\right)-1\right)}{(P_2+P_3)\left(\exp\left(P_1 h_v\right)-1\right)}. \tag{2.28}$$

The difference between γ_s and γ_{rvt} is due to the term P_3 that contains temporal decorrelation information. If no temporal decorrelation occurs then $\nu_v \to \infty$ and $\nu_g \to \infty$ and thus $P_3 \to 0$ and $\gamma_{rvt} = \gamma_s$. If $B_s = 0$, then the complex coherence becomes

$$\gamma_{rt} = \exp\left(\frac{-t}{\nu_g}\right)\frac{P_2\left(\exp\left((P_2+P_3)h_v\right)-1\right)}{(P_2+P_3)\left(\exp\left(P_2 h_v\right)-1\right)}. \tag{2.29}$$

Because of the exponential functions (2.29) implies that when the motion increase from bottom to the top of the canopy layer, the coherence decreases and phase center height lifts. In the case of the RVoG model, the temporally decorrelated complex coherence equals

$$\begin{aligned}\gamma_{rvgt} &= \exp\left(j\varphi_g\right)\frac{\int_0^{h_v}\rho_{vg}(z)\xi(z,t)\exp\left(jk_z z\right)dz}{\int_0^{h_v}\rho_{vg}(z)dz} \\ &= \exp\left(j\varphi_g\right)\frac{\mu\exp\left(\frac{-t}{\nu_g}\right)+\gamma_{gt}\exp\left(-j\varphi_g\right)}{\mu+1} \\ &= \exp\left(-j\varphi_g\right)\times \\ &\left(\gamma_{vt}\gamma_s\exp\left(-j\varphi-g\right)+\frac{\mu}{\mu+1}\left(\gamma_{gt}-\gamma_{vt}\gamma_s\exp\left(-j\varphi_g\right)\right)\right),\end{aligned} \tag{2.30}$$

where the role of ground scattering mechanism is represented by the Dirac delta function located at $z = z_0$ (Lavalle, 2009) used for obtaining μ that has a weight of σ_g. Here, $\gamma_{gt} = \exp\left(\frac{-t}{\nu_g}\right)$ is the temporal decorrelation of the ground layer that is real-valued and γ_{vt} is the complex-valued temporal decorrelation of the vegetation layer. Since in the RMoG model temporal decorrelation is assumed to be caused only by the motion of scatterers, μ does not reflect temporal changes. We used the information provided in this chapter about the RMoG model and modified it to explore the possibility of reconstructing of the vegetation layer accurately in Chapter 3. Later on, the idea of including temporal decorrelation component was extended to tomographic SAR data in Chapter 4 followed by estimating biomass by the proposed modified model in Chapter 5.

3

A Modified Model for Estimating Tree Height from PolInSAR with Compensation for Temporal Decorrelation

This chapter is based on the published paper: Ghasemi, N., Tolpekin, V. and Stein, A., (2018). A modified model for estimating tree height from PolInSAR with compensation for temporal decorrelation. International Journal of Applied Earth Observation and Geoinformation, 73, pp.313–322.

Abstract

The RMoG (Random-Motion-over-Ground) model is commonly used to obtain tree height values from PolInSAR images. The RMoG model borrows its structure function from conventional RVoG (Random-Volume-over-Ground) model which is limited for modelling structural variety in canopy layer. This chapter extends the RMoG model to improve tree height estimation accuracy by using a Fourier-Legendre polynomial as the structure function. The new model is denoted by the RMoG_L model. The proposed modification makes height estimation less prone to errors by enabling more flexibility in representing the vertical structure of the vegetation layer. We applied the RMoG_L model on airborne P- and L-band PolInSAR images from the Remingstorp test site in southern Sweden. We compared it with the RMoG and the conventional RVoG models using Lidar height map and field data for validation. For P-band, the relative error was equal to 37.5% for the RVoG model, to 23.7% for the RMoG model, and to 18.5% for the RMoG_L model. For L-band it was equal to 30.54% for the RVoG model, to 20.02% for the RMoG model, and to 21.63% for the RMoG_L. We concluded that the RMoG_L model estimates tree height more accurately in P-band, while in L-band the RMoG model was equally good. The RMoG_L model is of a great value for future SAR sensors that are more focused than before on tree height and biomass estimation.

Keywords: Vegetation height, Temporal decorrelation, Fourier-Legendre series, P-band, L-band, PolInSAR

3.1 Introduction

Polarimetric SAR interferometry is an advanced method for measuring vegetation height from remote sensing images (Cloude and Papathanassiou, 1998a; Bamler and Hartl, 1998). In this chapter, we use a full polarimetric interferometric SAR system. Such an image enables us to consider two 2×2 complex scattering matrices representing complex scattering coefficient. These matrices are used to obtain complex coherence (Cloude and Papathanassiou, 1998a) from two slightly different orbital positions. The complex coherence represents consistency of objects when illuminated from two different orbital positions at two different times (Papathanassiou and Cloude, 2001). A change in the objects is reflected in the form of signal decorrelation when generating interferograms. Therefore, by reversing the process of interferogram generation, the sources of these decorrelations can be identified. Main decorrelations occuring in vegetated areas are volumetric, temporal, geometric and systematic decorrelation (Zebker and Villasenor, 1992). In the past, the only source of decorrelation used for modeling vegetation height was volumetric decorrelation. This was based upon the assumption that the other decorrelations were negligible. The same assumption was made for the RVoG (Random-Volume-over-Ground) model (Cloude and Papathanassiou, 2003). This assumption, however, leads to biased estimation (Cloude and Papathanassiou, 2003; Neumann et al., 2010; Lavalle et al., 2012).

Several studies focused on understanding and quantifying the temporal decorrelation on repeat-pass InSAR and PolInSAR data. One of the first models was suggested by Papathanassiou and Cloude (2003) called RVoG+VTD (Volumetric Temporal Decorrelation) Other researchers used external ancillary data e.g. Lidar and field data to quantify temporal decorrelation (Simard et al., 2012).

Recently, the RMoG (Random-Motion-over-Ground) model has been introduced to obtain the vegetation height using PolInSAR images in the presence of temporal decorrelation (Lavalle et al., 2012). It uses the Gaussian-statistic motion model explained in Zebker and Villasenor (1992) that increases from the bottom to the top of the canopy layer. This function is responsible for modelling temporal decorrelation e.g. caused by wind (Lavalle and Khun, 2014; Lavalle and Hensley, 2015). A recent study has analyzed different algorithms for compensating temporal decorrelation and compared those with ancillary field and Lidar data (Simard and Denbina, 2018). The RMoG model showed promising results in estimating canopy height in the presence of temporal and performed better than the VTD model.

The RMoG model considers the vegetation layer as randomly distributed vertical objects over the ground and can be characterized by two selected polarization channels. The selected channels are assumed to represent one type of a scattering mechanism, with the highest backscattering occuring at the top of the canopy layer. Such an assumption, however, falls short especially for complex vegetation layers like in dense forests (Cloude, 2010). The main objective of the current chapter is to modify the RMoG model suggested in Lavalle et al. (2012) and generalize it in modeling the vertical structure of the vegetation layer.

To achieve this objective, we replaced the exponential function applied in the RVoG and RMoG models with a function that is able to reconstruct various types of underlying vertical structures. An expansion of the Fourier-Legendre series used in Polarization Coherence Tomography (PCT) (Cloude, 2006) is a substitute able to accurately reconstruct the vertical structure (Cloude, 2010). It allows the maximum of the structure function to occur at any place between the surface and the top of the canopy layer. This may lead to height estimation of a higher accuracy. We will denote the modified model as the RMoG_L model, indicating that it uses the motion scenario of the RMoG model and a Legendre polynomial as the structure function. We selected data from the BioSAR2010 campaign obtained at the Remingstorp test site in southern Sweden to demonstrate how the modified temporal decorrelation model can be used on a future BIOMASS mission by ESA (Ulander et al., 2011b). The RMoG_L model was tested on P- and L-band images and Lidar as well as field data were used as the reference for accuracy assessment. Resulting vegetation height values of the RMoG_L model were compared to those from the RMoG and RVoG models to reveal how the height estimation accuracy changed after modifying the structure function.

The chapter is structured as follows. First we give a short introduction to height estimation models, in particular the RVoG, RMoG and RMoG_L models. The second part presents the data and the study area. Next, we explain the implementation of the models and accuracy assessment. This is followed by presenting and discussing the results. The chapter ends with the conclusions.

3.2 Materials and Methods

We employed BioSAR2010 data for this study as it covers a large forested area. A complete report about the BioSAR2010 campaign and Remningstorp area has been published previously (Ulander et al., 2011a). Here, a summary is provided that is relevant for this study.

3.2.1 Data description

The Remningstorp estate in southern Sweden is located at 58°30′ N and 13°40′ E and has an area of over 1500 ha. Approximately 1200 ha is covered by productive forest and the rest with lakes. The area is generally flat with height variations between 120 m and 145 m above mean sea level. During the BioSAR 2010 campaign, P and L-band PolInSAR data were collected with the SETHI airborne sensor, developed by the Office National d'Etudes et de Recherches Aérospatiales (ONERA). Moreover, the Lidar CHM (Canopy-Height-Model) with a cell size of 0.5×0.5 m^2 was available for this area. It was derived from the differences between the first and the last returns of the Lidar pulses.

The field data used in this study include 214 circular plots with the radius of 10 m. Measurements inside each plot include: H100 height, defined as the basal area weighted average of the 100 highest trees in each plot, Diameter

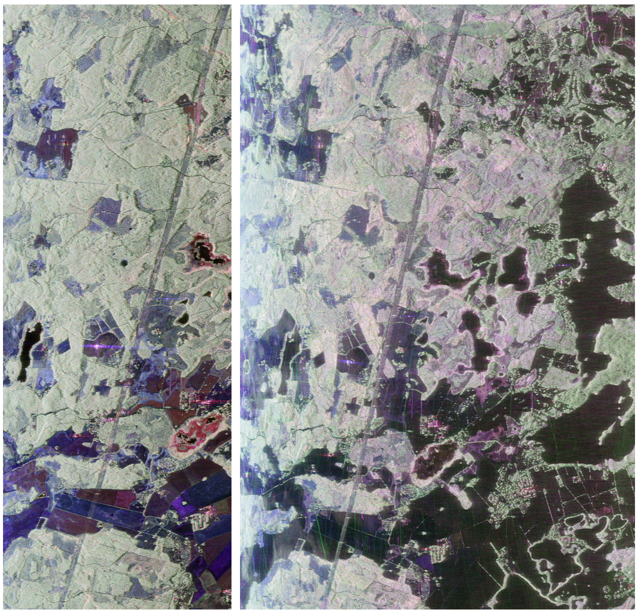

(a) (b)

Figure 3.1: The Pauli RGB (blue: $S_{hh} + S_{vv}$, green: $S_{hv} + S_{vh}$, red: $S_{hh} - S_{vv}$) of: (a) L-band and (b) P-band images. The color of each pixels represents the density of the vegetation cover and different scattering mechanisms. The agricultural fields, bare lands and water are shown as black or dark pixels.

at Breast Height (DBH), e.g. diameter at 1.3 m above the ground, and the dominant tree species (Ulander et al., 2011b). H100 is used generally as the reference height in estimating canopy height from PolInSAR (Mette et al., 2004). In this chapter, we used H100 and Lidar height averaged inside each field plot as the reference height.
We used one pair of P-band image and one pair of L-band image for the analyses. For both pairs, the spatial baseline equals 30 m, the temporal baseline is around 45′, and the heading angle is equal to 199°. The sensor height is approximately 4000 m^2, the ground-range resolution for the P-band pair is 0.5×0.5 m^2 while for L-band is 0.75×0.75 m^2(Ulander et al., 2011b). They were re-sampled to 1 m^2 for further analysis.

The top left coordinate for the L-band image is: 58.49398° E, 13.54952° N and covers an area of approximately 24.67 km^2. The top left coordinate for P-band is: 58.49398 ° E, 13.54952° N and covers an area of approximately 85.75 km^2 (Figure3.1). Due to deeper penetration into the canopy layer, the P-band image shows a variety of scattering mechanisms which is different from L-band. Within this campaign fieldwork, 117 plots fall within in the overlapping area between P and L band images (Figure 3.2). The images have been delivered in Single Look Complex (SLC) format and have four polarization channels: HH, HV, VH and VV with $HV = VH$ as the system

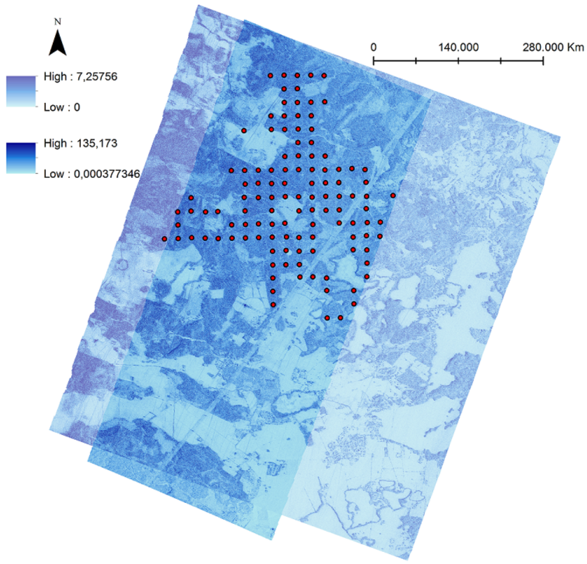

L band P band

Figure 3.2: Dark circles show the location of field plots on the overlapping area of P and L-band magnitude component. The top left coordinate for L-band is: 58.49398° E, 13.54952° N, number of pixels:2600×9490. The top left coordinate for the P-band is: 58.49398 ° E, 13.54952° N, number of pixels:12250×7000.

is mono-static.

We determined the scale factor or vertical wavenumber following Boerner et al. (1992). The complex coherence was obtained for all polarization channels including linear polarizations (HH, HV and VV), circular polarization (LL, LR and RR) and the Pauli decompositions ($HH + VV$ and $HH - VV$) (Lee and Pottier, 2009). The outcome served as input for the RVoG, RMoG and RMoG$_L$ models.

3.2.2 Height estimation using PolInSAR

3.2.2.1 The RVoG model

The conventional RVoG model has been used over the past decade for extracting forest parameters (Dobson et al., 1995; Cloude and Papathanassiou, 2003; Cloude, 2010). The RVoG model relates the observed complex volumetric coherence to the height of the vegetation layer and expresses the volumetric coherence γ_v as

$$\gamma_v = \frac{P_1}{P_2}\frac{e^{P_2 h_v} - 1}{e^{P_1 h_v} - 1}, \tag{3.1}$$

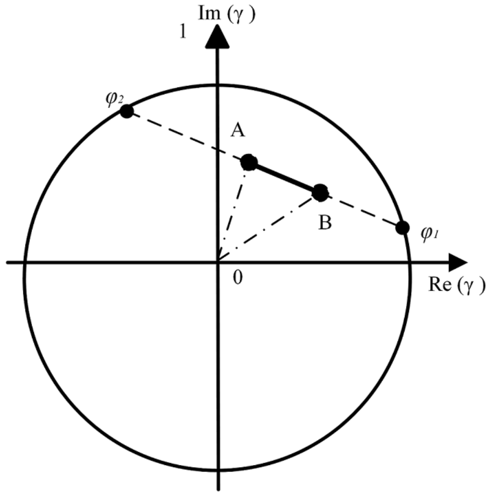

Figure 3.3: The geometrical representation of coherence line inside the unit circle of the complex plane. Point A and B are equal to the volume coherence and ground phase respectively and AB is the visible part of coherence. Only a segment of this line is observable from data.

where $P_1 = \frac{2\sigma}{\cos\theta}$, h_v is vegetation height, $P_2 = P_1 + jk_z$, and $k_z = \frac{4\pi B}{\lambda H \tan\theta}$. Here σ is the mean wave extinction coefficient, θ, $(0 < \theta < 90°)$ is the incidence angle, B is the spatial baseline, λ is the wavelength, and H is the sensor height (Cloude and Papathanassiou, 2003).
For the RVoG model, both ground and volume coherence are taken into account. For this purpose the ground phase φ_g and γ_v are combined with a parameter (μ) to compensate for the surface scattering mechanism effects on the observed coherence. Parameter μ can have any value between 0 and ∞ (Cloude and Papathanassiou, 2003) but it is small (< 1) in the cross-polarized channels in P and L-bands. According to Cloude (2005), the complex coherence γ_R equals

$$\gamma_R = e^{j\varphi_g}\frac{\gamma_v + \mu}{1+\mu} = e^{j\varphi_g}\left[\gamma_v + \frac{\mu}{\mu+1}(1-\gamma_v)\right]. \tag{3.2}$$

To solve (3.2) for φ_g, we need a polarization channel as the volume scattering and another channel as the ground scattering representation. Solving (3.2) is done in a multi-step procedure (Cloude and Papathanassiou, 2003).
Equation (3.2) implies that the complex coherence can be interpreted as a straight line inside the complex plane by varying μ values. If $\mu = 0$, then $\gamma_R = \gamma_v$, whereas if $\mu \to \infty$, γ_R equals the surface coherence. The geometrical representation of (3.2) is shown in Figure 3.3, where the straight line cuts the unit circle in the complex coherence plane at two points, denoted by φ_1 and φ_2. One of these points is equal to φ_g whereas the other point is an invalid solution, i.e. outside the meaningful physical range.

Point A equals the volume coherence and is determined from the data. The length of AB which is the observable coherence, depends upon the

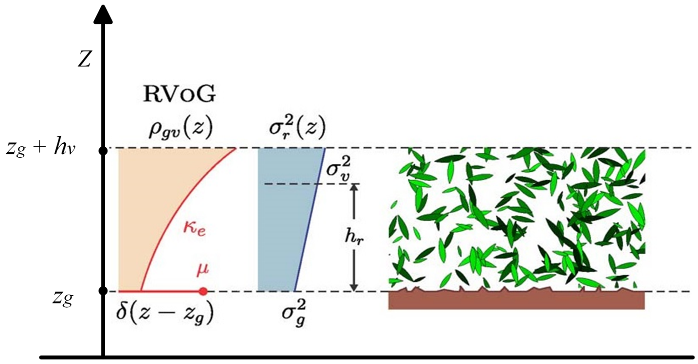

Figure 3.4: A simple representation of RVoG model structure function and motion variance of the RMoG model. The surface layer is located at $z = z_g$ and volume layer is distributed between z_g and $z_g + h_v$. Where h_v is the vegetation layer thickness, adopted from Lavalle et al. (2012).

baseline, the wavelenght of the SAR system and the vegetation structure (Papathanassiou and Cloude, 2001).
To identify A, total least square line fitting (Cloude and Papathanassiou, 1998a), maximum likelihood estimation using the complex Wishart distribution and the ESPIRIT algorithm (Lee and Pottier, 2009) have been suggested. We used the first method as it provides stable results (Cloude and Papathanassiou, 1998a). In this way, we determined the distance between φ_1 and φ_2 and the phase value of the HV channel as the representative of volume scattering. The φ value with the largest distance to the HV channel is recognized as φ_g (Cloude and Papathanassiou, 2003).
As the next step, a hybrid method estimates the height based on the obtained φ_g (Cloude and Papathanassiou, 2003). This method is fast, easy to implement and robust. Its basic assumption is that the selected channels contain pure volumetric and ground scattering. This is a valid assumption in case of L-band. However, for P-band this is not generally true because of deeper penetration (Garestier et al., 2008). Previous studies have shown that if we have a dense forest with at least one channel with ground-to-volume-ratio less than 10 dB as we have in our study area (Askne and Santoro, 2012), it is still reasonable to use the RVoG model for P-band (Wang et al., 2016).
As the RVoG model is a model of volume coherence and ignores temporal decorrelation, it provides biased results if the temporal decorrelation is high, e.g. due to wind (Simard et al., 2012). To tackle this limitation, the RMoG model has been proposed (Lavalle et al., 2012).

3.2.2.2 The RMoG model

The RMoG model assumes that the vegetation layer consists of vertical objects randomly located on a rough dielectric layer. Both layers have a random movement along the vertical axis (Figure 3.4).

Based upon this assumption, the complex coherence obtained by the

RMoG model γ_M is formulated as (Lavalle et al., 2012)

$$\gamma_M = \frac{\int_{z_g}^{z_g+h_v} \rho\,(z) \exp(jk_z z) \exp\left(-\frac{1}{2}\left(\frac{4\pi}{\lambda}\right)^2 \sigma^2(z)\right) dz}{\int_{z_g}^{z_g+h_v} \rho\,(z)\, dz}. \tag{3.3}$$

Here, $\sigma_r^2(z)$ is the first order approximation of the motion variance along the vertical axis (Lavalle and Khun, 2014) and is defined as

$$\sigma_r^2(z) = \sigma_g^2 + (\sigma_v^2 - \sigma_g^2)\frac{z - z_g}{h_r}, \tag{3.4}$$

where h_r is the reference height, λ is the SAR system wavelength and σ_g and σ_v are the surface and canopy layer motion standard deviations, respectively. The function $\rho(z)$ is the structure function, which defines the scattering properties of the vegetation and ground layers. Similar to the RVoG model, the structure function can be written as the sum of two components:

$$\rho(z) = \rho_v(z) + \alpha_g e^{-\frac{2K_e}{\cos\theta}} \delta\,(z - z_g)\,, \tag{3.5}$$

where $\rho_v(z)$ represents the canopy layer, defined as

$$\rho_v(z) = \alpha_g \exp\left[-\frac{2K_e}{\cos\theta}(z - z_g - h_v)\right]. \tag{3.6}$$

Here, α_g is the average backscatter per unit length of the vegetation layer. The second component includes $\delta(.)$, the Dirac delta function which is associated with the ground layer. This component characterizes the effect of surface scattering in the two-layer vegetation model (Cloude and Papathanassiou, 2003). The final form of the complex coherence obtained by the RMoG model $\tilde{\gamma}_M$ is obtained by replacing (3.5) and (3.6) into (3.3) and solve the integral. In the solved form of (3.3) the two-component structure function is expanded as a Gaussian function (Lavalle et al., 2012).

$$\tilde{\gamma}_M = e^{j\varphi_g} \frac{\mu\gamma_{M_g} + \gamma_M e^{-j\varphi_g}}{\mu + 1}, \tag{3.7}$$

where γ_{M_g} is the complex coherence for the ground layer (Lavalle and Khun, 2014). As can be deduced from (3.3) to (3.7), the complex coherence is a function of h_v, K_e, φ_g, σ_g, σ_v, k_z and λ. Following Cloude and Papathanassiou (2003), and Lavalle and Hensley (2015), at least five different polarization states are needed to find the unknown parameters. As μ is different for each polarization channel, two more unknown parameter are added to the equation system for each channel. Since then the number of unknown parameters exceeds the observations, the solution should be a multi-step procedure (Lavalle and Hensley, 2015). According to (3.3) to (3.5), it is assumed that the backscattering and consequently the structure function increases exponentially from the bottom to the top of the canopy layer. It implies that the maximum of the backscattering occurs always at the top or close to the top of the vegetation layer. This assumption leads to a non-flexible model when it comes to multi-layer and complex vegetated areas. Inspired by the PCT model and its structure function explained in Cloude (2010), we modified the RMoG model to overcome this limitation.

3.2.2.3 The RMoG$_L$ Model

The modified RMoG model, denoted as the RMoG$_L$ model, uses Fourier-Legendre polynomials as its structure function. Fourier-Legendre polynomials are commonly used in the PCT model to estimate the underlying vertical structure of the objects (Cloude, 2006). For using Fourier-Legendre series as the structure function, we need to first re-scale the vertical axis as

$$z' = \frac{2(z - z_g)}{z_g + h_v} - 1, \tag{3.8}$$

where $z' \in [-1, 1]$. Based on Cloude (2010) the new structure function $f(z') \simeq \rho(z) - 1$, equals

$$f(z') = \sum_{n=0}^{\infty} a_n P_n(z'), \tag{3.9}$$

where

$$a_n = \frac{2n+1}{2} \int_{-1}^{1} f(z') P_n(z') dz'. \tag{3.10}$$

Here, the a_n, $n = 0, 1, 2, ...$ are the Legendre coefficients and the P_n are the Legendre polynomials. The structure function of the RMoG$_L$ model is compared with the exponential function used in the RVoG and RMoG models in Figure 3.5. The functions are normalized to the interval $0 \leq z' \leq 1$. The differences between the structure functions show the flexibility of Fourier-Legendre expansion in modeling the vertical structures. If f_0 is larger than the higher orders, it represents strong surface backscattering, whereas larger higher terms signify a strong volume scattering and complex vertical structure. The first three terms of P_ns equal (Cloude, 2006)

$$\begin{aligned} P_0(z') &= 1, \\ P_1(z') &= z', \\ P_2(z') &= \frac{1}{2}(3z'^2 - 1). \end{aligned} \tag{3.11}$$

By substituting (3.9) as $\rho(z)$ in (3.3) and re-scaling the integral limits, the complex coherence obtained by the RMoG$_L$ model γ_{M_L}, equal

$$\begin{aligned} \gamma_{M_L} =& \exp(jk_v) \times \\ & \frac{\int_{-1}^{1} \exp(1 + f(z')) \exp(jk_v z') \exp\left(-\frac{1}{2}\left(\frac{4\pi}{\lambda}\right)^2 \sigma'^2(z')\right) dz'}{\int_{-1}^{1} (1 + f(z')) dz'}, \end{aligned} \tag{3.12}$$

where $k_v = \frac{k_z h_v}{2}$, $\sigma'^2(z')$ is obtained from (3.4) by using (3.8). To solve (3.12), we need to use an expansion of (3.9) with a limited number of Legendre coefficients. In general, the number of terms of the structure function depends upon the number of available PolInSAR images and complexity of

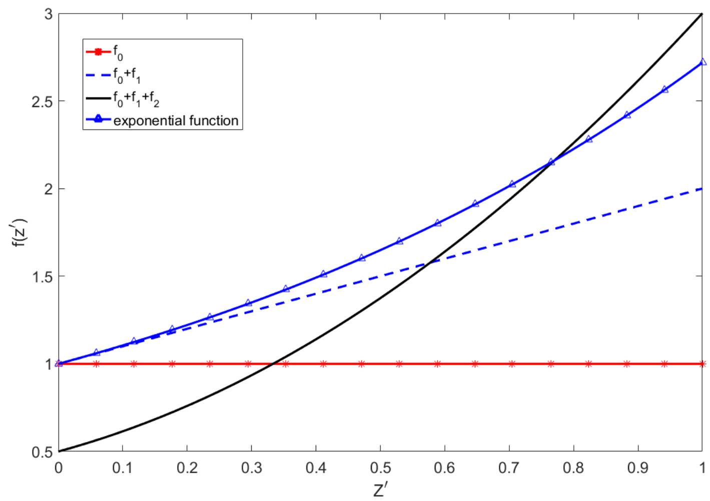

Figure 3.5: Fourier-Legendre expansion up to the second order vs. the exponential function used in the RVoG and RMoG models in [0 1] interval. The solid black line shows the structure function of the RMoG$_L$ model.

the vegetation layer. Since we are using single-baseline PolInSAR images we can only estimate the first and second terms of the series (Cloude, 2010). Thus (3.12) can be expanded as

$$\gamma_{M_L} = \exp(jkv)\times \frac{\int_{-1}^{1}(1+\sum_{n=0}^{\infty} a_n P_n(z'))\exp(jk_v z')\exp(\frac{-1}{2}(\frac{4\pi}{\lambda})^2\sigma^{2\prime}(z'))dz'}{\int_{-1}^{1}(1+\sum_{n=0}^{\infty} a_n P_n(z'))dz'}, \tag{3.13}$$

here we assume $C = \exp(\frac{-1}{2}(\frac{4\pi}{\lambda})^2\sigma^{2\prime}(z'))$. Appendix A.2 includes the expansion up to $n = 3$. The total complex coherence $\tilde{\gamma}_{M_L}$ is then obtained by replacing (3.13) in (3.12). For simplification and according to the short time interval between the image acquisitions, we may assume that $\sigma_g = 0$ in (3.4). Then C is only related to the motion of the vegetation layer and γ_{M_L} equals

$$\tilde{\gamma}_{M_L} = \frac{\gamma_{M_L}}{\mu+1}. \tag{3.14}$$

After normalizing the Legendre coefficients as $a_n = \frac{a_n}{1+a_0}$ the unknown parameters to be estimated include φ_g, h_v, C, a_1 and a_2. We considered C as a scalar when solving the equation system. The last two parameters are different for each polarization channel. This means that when adding a new polarization channel, two more unknown parameters are included. The matrix form of (3.13) equals

$$\begin{bmatrix} f_1 C & 0 \\ 0 & f_2 C \end{bmatrix} \times \begin{bmatrix} a_1 \\ a_2 \end{bmatrix} = \begin{bmatrix} \mathrm{Im}(\tilde{\gamma}_{M_{LK}}) \\ \mathrm{Re}(\tilde{\gamma}_{M_{LK}}) - f_0 \end{bmatrix}, \tag{3.15}$$

where $\tilde{\gamma}_{M_{LK}} = \tilde{\gamma}_{M_L} e^{-jk_v}$ and the $f_i, i = 0, 1, 2$ are

$$\begin{aligned}
f_0 &= \frac{\sin k_v}{k_v}, \\
f_1 &= j\left(\frac{\sin k_v}{k_v} - \frac{\cos k_v}{k_v}\right), \\
f_2 &= \frac{3\cos k_v}{{k_v}^2} - \left(\frac{6 - 3{k_v}^2}{2{k_v}^3} + \frac{1}{2k_v}\right)\sin k_v.
\end{aligned} \tag{3.16}$$

Since there are more parameters than observations, we can not estimate all parameters within a single step. To solve this issue, we summarize (3.16) as $Fa = g$ and assign a random value between 0 and 1 to C and then solve the equation system as $\hat{a} = F^{-1}g$ (Press, 2007; Cloude, 2010). Then the estimated $\hat{a}$ is used to re-calculate C. This process is repeated until the following condition is satisfied (Cloude, 2006)

$$\frac{\|\partial a\|}{\|a\|} \leq \frac{\sin^2 k_v - k_v^2}{\sqrt{2L}(3\cos k_v - (3 - k_v^2)\frac{\sin k_v}{k_v})}. \tag{3.17}$$

Here, ∂a is the matrix of partial derivatives of a, L is the number of effective looks obtained by Cramér-Rao bound (Touzi et al., 1999). The results of the RVoG model is used to estimate the initial value of k_v. A major part of pre-processing step (besides co-registering) and implementation of the models were performed using PolSARPro and MATLAB respectively.

3.2.3 Accuracy assessment

For evaluating the accuracy of three different height estimation models, the average height inside each plot was compared with the corresponding values on Lidar CHM and with the H100 values. The H100 parameter was acquired from the package provided by ESA and was not obtained during the study. The RMSE and R^2 were used as metrics to compare the height estimation models. Since the physical nature, resolution, and processing approach of the Lidar CHM and PolInSAR height maps are different and additionally, field plots are only available for a part of the images, we compared the histograms and density functions of the overlapping part of the images instead of point by point comparison.

For finding the best describing function, different probability functions were tested and compared using various criteria (Martinez and Martinez, 2007). The generalized extreme function was selected as the best describing function. According to Rolland et al. (2000), Pass and Zabih (1999), and Jia et al. (2006) a good measure to compare two histograms is the χ^2 distance. The χ^2 distance between reference data and other height estimation methods equals

$$\chi^2 = \sum_{i=1}^{n} \frac{(h_{RFi} - h_{CAi})^2}{(h_{RFi} + h_{CAi})}, \tag{3.18}$$

where h_{RF} and h_{CA} are the reference and calculated height values respectively and n is the number of samples.

Table 3.1: The RMSE and relative error of three different height estimation models in comparison to Lidar height.

	P-band		L-band	
	RMSE (m)	Relative error (%)	RMSE (m)	Relative error (%)
RVoG model	7.50	37.50	5.30	30.54
RMoG model	4.17	23.70	4.00	20.02
RMoG$_L$ model	2.50	18.50	3.89	21.63

Table 3.2: R^2 values between PolInSAR height resulting from three different models and H100 for L and P-bands (within 95% confidence interval.)

	RVoG	RMoG	RMoG$_L$
L-band	0.40	0.53	0.45
P-band	0.43	0.47	0.48

3.3 Results

3.3.1 Experimental results

The results of applying the RMoG and RMoG$_L$ models on P band are shown in Figure 3.6. The differences between produced height maps shows better performance of the RMoG$_L$ model especially in shorter trees and clear-cut areas. This is due to the fact that RMoG$_L$ model takes into account the structural parameters. The motion standard deviations of both models have similar ranges, but in Figure 3.6(e) more variation is visible. The ground phase reflects the relatively flat topography in the study area (For full size images and Lidar height map see Appendix B). The difference between φ_g obtained by two models shows the effect of using different structure function in the RMoG$_L$ model. A similar trend was observed when applying RMoG and RMoG$_L$ models on L-band.

For validating the results, we compared the average height values inside the field plots, first to the corresponding H100 values and second, to the Lidar CHM data. The results for the RVoG, RMoG and RMoG$_L$ models are presented in Figure 3.7.

As it can be observed, the RVoG and RMoG models performs slightly better in L-band while the RMoG$_L$ models shows better results in P-band. Finding two polarization channels with only volume and surface scattering mechanisms is a basic assumption of the RVoG model and consequently the RMoG models. This assumption is closer to reality in L-band and this is the reason of the better performance of the RMoG model. In contrary, the RMoG$_L$ model reconstructs the vertical structure and therefore works better with deep penetration of P-band. The RMSE and relative error values for both L and P-bands are listed in Table 3.1.

The RMSE and relative errors confirm a better performance of the RMoG$_L$ model when using P-band. The RMoG model, however, performs better than the other models when using L-band. A similar comparison was performed with H100 values extracted from ESA data package (Table 3.2).

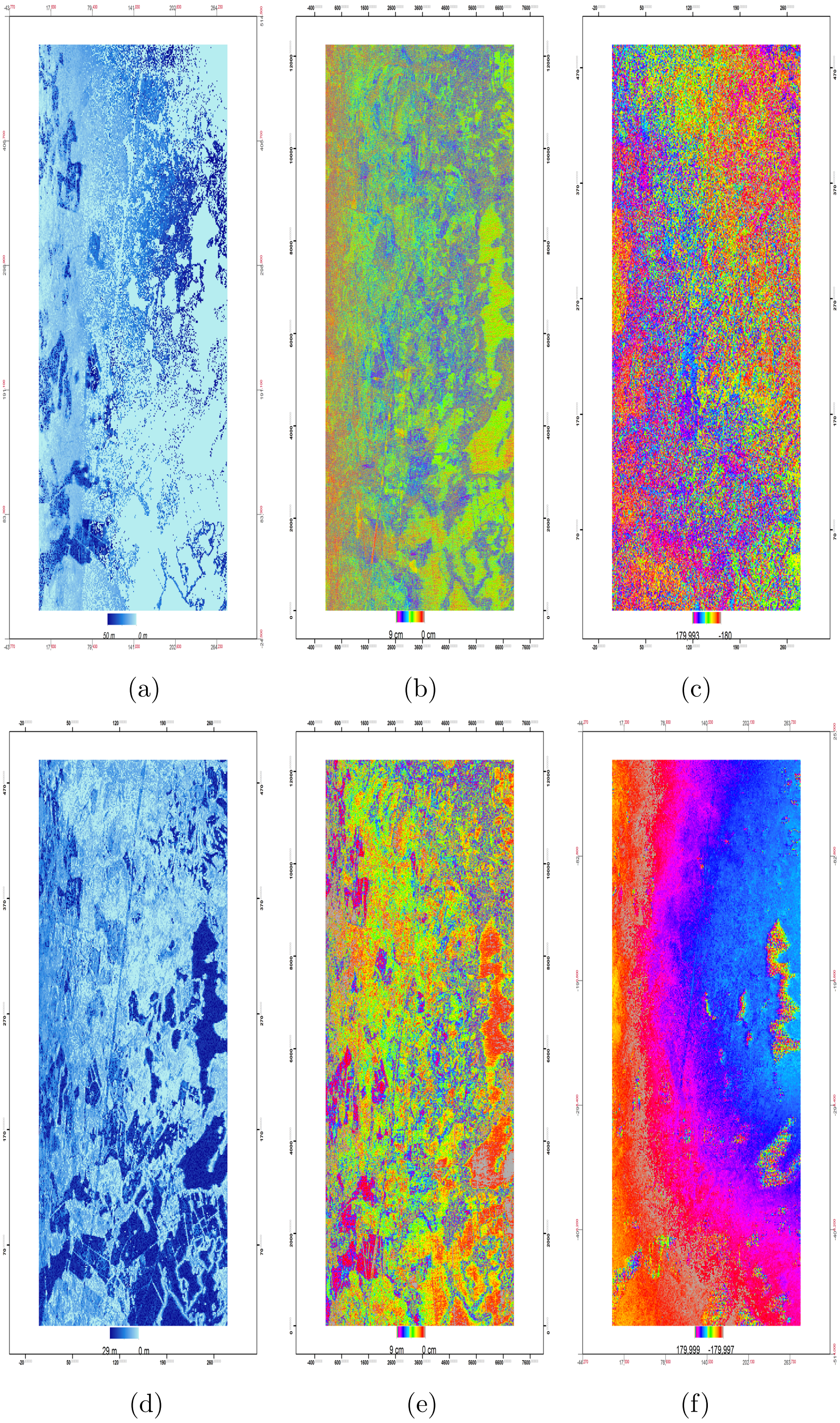

Figure 3.6: Results of applying the RMoG model: (a) height map, (b) $\sigma'(z')$, and RMoG$_L$ model: (c) φ_g. (d) height map, (e) $\sigma'(z')$, and (f) φ_g on P-band. The top left coordinate is: 58.49398 °E, 13.54952° N, number of pixels in original image was: 12250×7000 and pixel size is 1 m. Displayed images are multi-looked using a 25× 25 window.

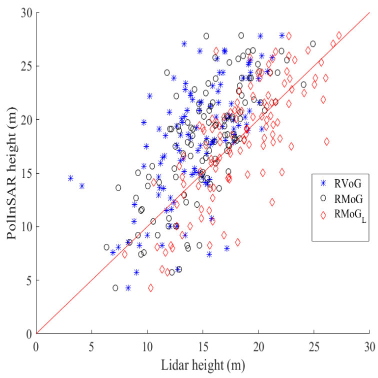

(a)

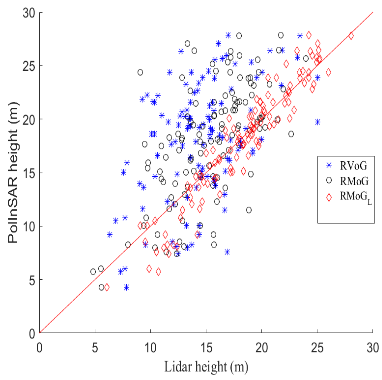

(b)

Figure 3.7: Averaged Lidar CHM vs. estimated canopy height from PolInSAR by the RVoG, RMoG and RMoG$_L$ models for: (a) P-band, and (b) L-band.

Table 3.3: The χ^2 distance between Lidar CHM and the height maps resulting of the RMoG$_L$ and RMoG models.

	RMoG	RMoG$_L$
χ^2 for P-band	4.3	3.2
χ^2 for L-band	3.5	5.7

The low correlations between PolInSAR height and H100 occur because H100 is measured based upon the tallest trees inside each field plot, while the PolInSAR height represents the average canopy height. Therefore, we need the average tree heights inside plots for having a good comparison. Those were not available from the campaign field data.

As a new accuracy assessment approach, based upon the physical nature of the PolInSAR and Lidar data, the histograms of the PolInSAR height maps were plotted against the Lidar CHM (Figure 3.8). The P-band histograms show that the heights of short trees are overestimated by both the RMoG and RMoG$_L$ models. For taller trees, however, the height is underestimated by PolInSAR. The RMoG model performs slightly better for L-band. For taller trees, both RMoG and RMoG$_L$ models showed promising results. To compare the histograms, the χ^2 values are listed in Table 3.3.

It shows that the best model performance belongs to the RMoG$_L$ model when using P-band and to the RMoG model when using L-band. Moreover, the parameters of the generalized extreme value distribution (Hosking et al., 1985) i.e. the shape *(P)*, scale *(E)*, and location of the maximum *(L)* and are listed in Table 3.4. The RMoG$_L$ model has the distribution closest to the Lidar CHM when using P-band, whereas in case of using L-band the RMoG model has the best result.

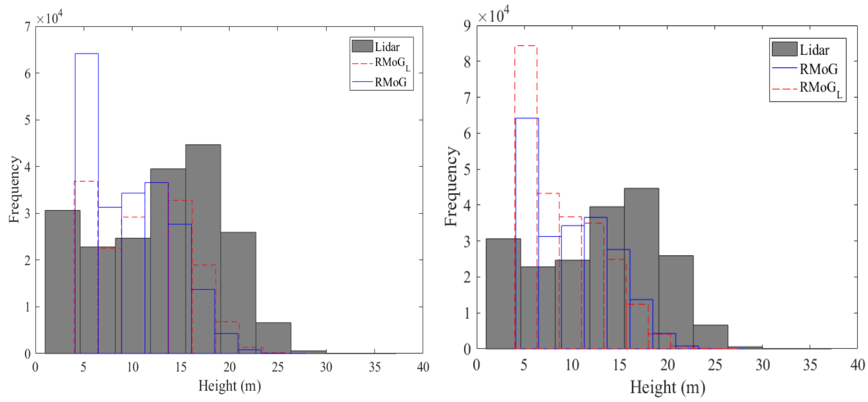

(a) (b)

Figure 3.8: Histograms of RMoG_L and RMoG models vs. Lidar CHM of: (a) P-band, and (b) L-band.

Table 3.4: The parameters of generalized extreme value distribution selected as the best matching distribution for the height maps.

	P-band			L-band		
	P	E	L	P	E	L
Lidar	-0.14	5.50	24.81	-0.14	5.50	24.81
RMoG_L	-0.14	5.68	24.81	-0.15	6.10	25.66
RMoG	-0.15	6.14	26.50	-0.14	5.30	24.30
RVoG	-0.19	4.99	26.79	-0.16	4.02	25.07

3.4 Discussion

Our findings suggest that using a Fourier-Legendre series as the structure function in the RMoG_L model improves the height estimation accuracy. The Fourier-Legendre expansion has been employed in Polarization Coherence Tomography (PCT) (Cloude, 2006, 2010) to estimate underlying structure of the vertical layers. Here, by replacing the exponential function used in the RVoG and RMoG models with the second order Legendre polynomial the accuracy of height estimation by 16% for P-band improved.

According to (3.3), the observed complex coherence depends upon the underlying vertical structure, topographic phase and motion standard deviation. The structure function $\rho(z)$ is defined between z_g and $z_g + h_v$ and it should be selected such that it matches the structure of vegetation layer.

For estimating vegetation height, the special cases of this function are often used, i.e the uniform and the exponential functions (Cloude and Papathanassiou, 2003). If we assume that $\rho(z) = 1$, i.e. a uniform function, the complex coherence can be defined as a function of vertical wave-number, vegetation height, and the surface phase (Cloude, 2010). In this case, the only parameter taken into account from the vegetation structure is h_v that is not changing with polarization. A structure function that equals the expo-

nential function is widely used in the RVoG and RMoG models for estimating vegetation height. This exponential function uses h_v and K_e, where K_e defines the shape of the vegetation layer and changes with polarization and spatial baseline B_n. The spatial baseline is involved in calculating vertical wave number k_z. Since there is no linear relation between changing spatial baseline and PolInSAR height, it is needed to be evaluated separately. A previous study has shown the effects of changing vertical wavenumber on PolInSAR height (Kugler et al., 2015). A fully extincted signal represents strong volume decorrelation at the top of the canopy layer. Hence, the maximum backscattering gets closer to the top of the canopy layer with increasing extinction. Thus, the main assumption is that the maximum backscattering is concentrated on the top of the canopy layer.
To change the structure function of the RMoG model and increase its flexibility, we used the Fourier-Legendre series. Commonly, the lower terms of the series show the general characteristics of the canopy, whereas the higher terms represent the details of the vegetation structure (Cloude and Papathanassiou, 2003). The number of terms that we can use depends upon the number of available images and complexity of the vertical layer. Here, we truncated the expansion up to the second order since we have a single baseline. Additionally, we are working within a hemi-boreal forest where the vertical structure is relatively simple and thus a second order function should be adequate (Cloude, 2006). Moreover, we need no assumption about the location of the maximum backscattering along the vertical direction. This is advantageous if we have multi-layer vegetation as for instance in dense forests. The RMoG_L model showed good results for P-band, whereas its performance was similar to that of the the RMoG_L model on L-band. This shows that the exponential structure function represents the scattering scenario in L-band with good accuracy.
Due to the short time interval between image acquisitions, we assumed that $\sigma_g = 0$. This can be true in general cases of airborne PolInSAR data. In the case of space borne SAR data, however, this assumption can be true if there is no seasonal change and natural phenomena like landslides and earthquakes are absent. If the time interval is too long (several months), we might lose the coherence in vegetated areas and neither of the RVoG, RMoG and RMoG_L models would be applicable.
An important drawback of the RMoG_L model is the number of unknown parameters to be estimated. Polarization channels used in this study are the HH, HV, VV, $HH + VV$, $HH - VV$, LL, LR and RR channels (Lee and Pottier, 2009). These are not independent, although representing different physical characteristics of the vegetation. Also, these channels are more noisy than the original polarization channels acquired by the sensor. It will need further investigation and research on how the noise on these channels affects the overall accuracy and whether adaptive noise filtering on these channels can improve the accuracy. This becomes important if we use additional terms of the Fourier-Legendre series.

For solving the non-linear equation system resulting from applying the RMoG_L model, we took a step-by-step approach. It is important to have good starting values. Here, we used the outcomes of the RVoG model being

the best ones available. Alternatively, we could use arbitrary initial values based upon the physical meaning of these parameters and then get the best result using trial-and-error.
For validating the results, both field data and Lidar CHM were used. The results showed a weak correlation between average height value and H100. Therefore we suggest to use the average tree heights instead of H100. Additionally, since the PolInSAR and Lidar height maps differ in physical nature and they have different resolution, the point to point comparison as we do by field plots may not be comprehensive enough. Thus besides using field plots, histograms and PDF functions were used to compare the resulting height maps with Lidar.
The RMoG$_L$ model has the best matching histogram with the reference data when using P-band, whereas, the RMoG model had slightly better result in L-band. The difference between histograms and scatter plots has two main reasons. First, the scatter plots represent the average of Lidar CHM and PolInSAR height inside the field plots. The plots have been located very carefully during the BioSAR 2010 campaign to be homogeneous in terms of tree types, heights and density. Additionally, the areas with short trees (<10 m) are excluded from field work. Therefore, we see good statistical correlation between Lidar CHM and PolInSAR height maps. The second reason is that in short vegetation cover. The assumption of random-volume-over-ground model is not fully valid. Instead, the Oriented-Volume-over-Ground model should be replaced. This phenomena is explained in (Lopez-Sanchez et al., 2007; Cloude, 2010).

Other estimated parameters like the topographic phase were slightly different for P and L-band images but they had a meaningful physical range. Since we do not have any reference data for validating other parameters, accuracy assessment is restricted to vegetation height. Besides having more unknown parameters, estimating forest parameters using the RMoG$_L$ model takes approximately twice as long as using the RMoG or the RVoG models.

Due to the short time interval between the two images, other phenomena like the dielectric constant and seasonal changes are negligible but should be considered when using PolSAR images collected at larger time intervals. At present, P-band, on which we tested our suggested model, is only available from airborne sensors. In the near future it will also be available from space borne sensors and thus, it would be of value to examine the available PolInSAR coherence models to provide a better understanding of the similarities and differences of applying these models on different wavelengths.

3.5 Conclusions

In this chapter, we proposed to change the structure function of the RMoG model to improve the accuracy of tree height estimation with taking into account the temporal decorrelation. We tested it on P and L-band full polarimetric images acquired from the Remingstorp test site in Sweden. The model improved the height estimation accuracy as compared to the RMoG and RVoG models for P-band, but the RMoG model had a slightly better performance for L-band. Moreover, the RMoG_L model was more flexible in modeling different structure types of the vegetation layer. A challenge we faced when using the RMoG_L model, was the long computation time. Another challenge was the number of unknown parameters. We solved this by taking a multi-step estimation procedure. As a support to the future satellite missions operating in P-band, findings of this study are potentially useful. Further research is needed to reveal the degree of improvement as related to longer computation time and the number of parameters. The RMoG_L model should be further tested on different forest types with multiple baselines and other sensors.

4 Estimating tree heights using multi-baseline PolInSAR data with compensation for temporal decorrelation

This chapter is based on the published paper: Ghasemi, N., Tolpekin, V. A., and Stein, A. (2018). Estimating Tree Heights Using Multi–baseline PolInSAR Data With Compensation for Temporal Decorrelation, Case Study: AfriSAR Campaign Data. IEEE Journal of Selected Topics in Applied Earth Observations and Remote Sensing, Volume: 11, Issue: 10, PP:3464–3477.

Abstract

This chapter presents a multi-baseline method to increase the accuracy of height estimation when using SAR tomographic data. It is based upon mitigating the temporal decorrelation induced by wind. The Fourier-Legendre function of different orders was fitted to each pixel as the structure function in the PCT model. It was combined with the motion standard deviation function from the Random-Motion-over Ground (RMoG) model. L-band multi-baseline data are used that were acquired during the AfriSAR campaign over La Lope national park in Gabon with a height range between 0 and 60 m that has an average of 30 m and standard deviation of 15 m. The results were compared with those from the regular PCT model using the root mean square error (RMSE). Histograms were compared to the one obtained from Lidar height map. The average RMSE was equal to 7.5 m for the regular PCT model and to 5.6 m for the modified PCT model. We concluded that the accuracy of tree height estimation increased after modelling of temporal decorrelation. This is of value for future satellite missions which would collect tomographic data over forest areas.

Keywords: Multi-baseline SAR data, PCT, temporal decorrelation, Fourier-Legendre series.

4.1 Introduction

Monitoring and mapping biophysical parameters of forests play an important role in environmental studies. Carbon stock assessment and the analysis of the global carbon cycle are directly affected by the accuracy and frequency of forest biomass estimation. Many studies in SAR remote sensing have been dedicated to monitor and measure forest parameters especially tree height. Future satellite missions like BIOMASS are designed to map forest from space at a high frequeny of repeat cycles (Le Toan et al., 2011). These missions have been designed to operate in L or P-band and in full-polarimetric mode. They will enable scientists to use polarimetric SAR interferometry (PolInSAR) (Cloude and Papathanassiou, 1998a; Papathanassiou and Cloude, 2001; Mette et al., 2004) and SAR tomography (Tebaldini and Rocca, 2012; Huang et al., 2011; Guillaso and Reigber, 2005) at a large scale with accuracy that meets user requirements. The accuracy, however is affected by factors like wavelength, vegetation structure and decorrelation sources. Despite these limitation factors, the unique ability of PolInSAR data in reconstructing vertical vegetation layer under all weather conditions, makes PolInSAR data the first choice in many forest studies. By using PolInSAR, different scattering mechanisms are identified using various polarization channels. Location of these mechanisms is determined by interferometry.

SAR tomography is comparable to PolInSAR with a major difference that a synthetic aperture is reconstructed in the vertical direction. Several parallel flight tracks are acquired with a relatively small baseline in the vertical direction. Processing tomographic data, however, is difficult because of sampling density and irregularity issues (Cloude, 2006). Polarization Coherence Tomography (PCT) is a hybrid approach (Cloude, 2006, 2007a, 2008) that reconstructs the vertical structure of the vegetation cover by employing PolInSAR height estimation techniques and using a function for the unknown vertical structure (Papathanassiou and Cloude, 2001; Cloude and Papathanassiou, 1998a; **?**). Parameters of that function are estimated using different polarization channels with different spatial baselines. Since PCT can be implemented efficiently, even using a single baseline, it has an advantage over conventional SAR tomography (Cloude, 2006).

Sepveral physical models have been developed for this purose (Cloude and Papathanassiou, 1998a; Papathanassiou and Cloude, 2001; Treuhaft and Siqueira, 2000). The random-motion-over-ground (RMoG) model is developed to estimate tree heights from PolInSAR data with mitigation of temporal decorrelation. It merges the random-volume-over-ground (RVoG) model with a model of temporal decorrelation (Lavalle et al., 2012; Lavalle, 2009). In doing so, obtains more accurate results when applied on airborne L-band data (Lavalle and Hensley, 2012) and multi-baseline PolInSAR data (Lavalle and Khun, 2014). We recently proposed the RMoG$_L$ model, a modified temporal decorrelation model that uses the Fourier-Legendre series to reconstruct the vertical structure in short time intervals (Ghasemi et al., 2018b). The RMoG$_L$ model showed promising results when applied on airborne P-band data (Ghasemi et al., 2018b). In this chapter, we combined PCT with the temporal decorrelation component of the RMoG model, resulting in the modified PCT model. The important difference with the regular PCT model and other multi-baseline height estimating techniques is that it mitigates the temporal decorrelation as a major source of error (Papathanassiou and Cloude, 2003; Neumann et al., 2010; Rocca, 2007; Lee et al., 2012; Li et al., 2014; Zhou et al., 2008). The objective of this chapter is to improve the PCT model by including the temporal decorrelation. The modified PCT model was applied on the L-band UAVSAR data acquired by NASA JPL during the AfriSAR campaign over the La Lope national park in Gabon. For providing a further comparison, the result of single-baseline modified PCT model was compared to both the conventional RVoG and RMoG models.

4.2 Materials and Methods

4.2.1 Study area and data set

The data used in this study are obtained from the AfriSAR campaign on the tropical forests in Gabon (Figure 4.1) (Dubois-Fernandez et al., 2016). The La Lope national park is located in the western semi-evergreen forests of central Africa. Forest boundaries have been advancing into savanna grasslands creating a complex system of forest types. The forest cover in this area can be divided into four types: savanna grasslands, young forest, Okoumé dominated forest, and mature old growth forest (Silva et al., 2018). Annual rainfall averages 1500 mm with two rainy seasons and two dry seasons. The longer dry season lasts from the beginning of June to the middle of September, which is followed by a longer rainy season until mid-December. The terrain elevation changes from terrain 230 to 470 m above-see-level with slopes up to approximately 30° in the western part of the area.
For measuring Above-Ground-Biomass (AGB) several studies have been carried out in this area (Silva et al., 2018). The method for measuring biomass is measuring height, diameter, and wood density and using the allometric equation for moist tropical forests (Silva et al., 2018; Chave et al., 2009).
The AfriSAR campaign was designed and conducted to support future satellite missions that are focused on forest monitoring and vegetation parameters estimation (Hajnsek et al., 2016; Dubois-Fernandez et al., 2016). L-band full polarimetric SAR data were collected with a UAVSAR sensor over the La Lope National Park in Gabon. We used a SLC (Single-Look-Complex) stack of seven full polarimetric SAR data with different spatial baselines. Temporal and spatial baselines and ambiguity heights are listed in Table 4.1. This multi-baseline, multi-frequency data set will allow us to estimate the key parameters for tropical African forests, like vertical height profiles and forest biomass (Hajnsek et al., 2016). In addition to the L-band SLC stack, Lidar data were available for the study area. They were acquired by the LVIS instrument that belongs to Jet Propulsion Laboratory (JPL) of California Institute of Technology (Caltech).

Table 4.1: The spatial and temporal baseline of L-band SLC stack of the Lope national park. These images were collected on March the 8th, 2016 (Lavalle, 2017).

baseline length (m)	Time of Acquisition (GMT)	Temporal baseline (minutes)	Altitude of ambiguity (m)
0	14:06	175	-
20	11:33	22	61
40	11:56	45	30
60	12:18	67	20
80	12:41	90	15
100	13:20	129	12
120	13:43	149	10

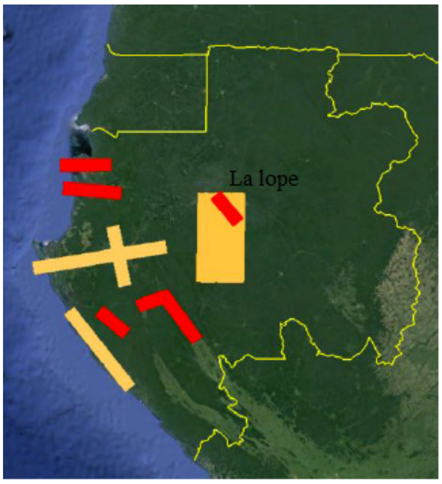

Figure 4.1: The patches of acquired data in AfriSAR campaign using UAVSAR over map of Gabon. The red patches are PolInSAR and TomoSAR data collecting locations and yellow patches show locations of PolSAR data acquisition. The central coordinates of La Lope national park are 0.5 W and 11.5 N and it has an area of 4910 km^2.

4.2.2 Data pre-processing and preparation

The first step for proper data use is calibration and co-registration of fully polarimetric SAR images. All slave images should be registered to the master one to form the SLC stack. This step was completed with the help of an ancillary data set including SRTM DEM and SAR orbital data (Lavalle et al., 2016b). The flowchart of data pre-processing and preparation is pictured in Figure 4.2. We applied coherence optimization for two purposes. First, the optimized channels were used for determining surface and volume scattering channels following Cloude (2006). Second, these polarization channels added the number of observations for estimating unknown parameters during steps. After this step, the SLC stack is ready for applying height inversion models.

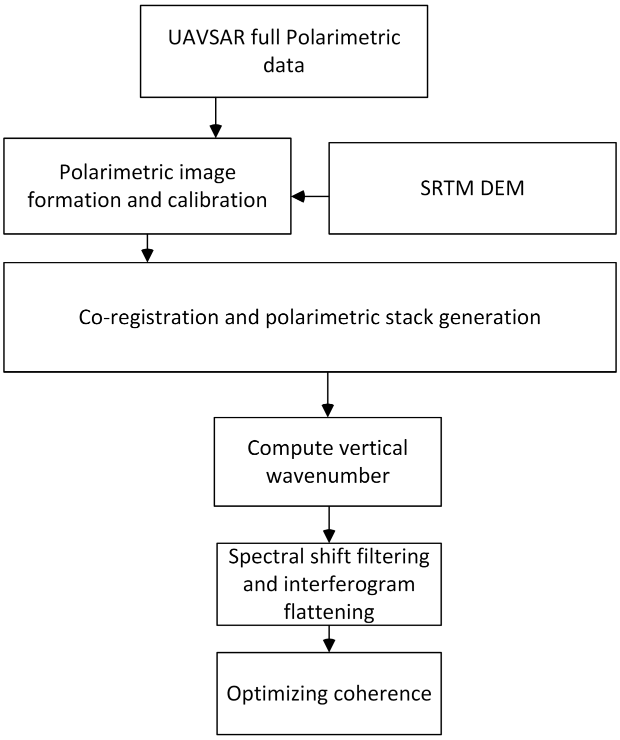

Figure 4.2: The flowchart of data pre-processing and preparation step. The coherence optimization and spectral shift filtering was performed according to the method described in Cloude and Papathanassiou (2002).

4.2.3 Multi-baseline polarization coherence tomography

To model the observed PolInSAR coherence by SAR tomographic data we proceeded as follows. The sensor parameters including wavelength and height are considered to be equal for all images, whereas other geometrical parameters including average look angle θ and vertical wave numbers k_z are different for each pair. The vegetation layer was taken as a vertical layer randomly distributed on the surface. For estimating vegetation height using PCT, we write the complex coherence $\tilde{\gamma}$ as

$$\tilde{\gamma} = e^{j\varphi_g} \frac{\int_0^{h_v} f(z)e^{jk_z z}dz}{\int_0^{h_v} f(z)dz}, \tag{4.1}$$

where φ_g is the ground phase and $f(z)$ is the vertical structure function defined in the range of $[0, h_v]$. Re-scaling the vertical axis as $z' = \frac{2z}{h_v} - 1$, we obtain $z = \frac{z'+1}{2} h_v$. The numerator and denominator of 4.1 can then be re-written in the range of $[-1, 1]$ as

$$\int_0^{h_v} f(z)e^{jk_z z}dz = \frac{h_v}{2}e^{j\frac{k_z h_v}{2}}\int_{-1}^{1} f(z(z'))e^{j\frac{k_z h_v}{2}z'}dz'$$

and (4.2)

$$\int_0^{h_v} f(z)dz = \frac{h_v}{2}\int_{-1}^{1} f(z(z'))dz'.$$

Here $f(z(z')) = 1 + F(z')$ and the new structure function will be called $F(z')$ hereafter. The function $F(z')$ can be developed as a Fourier-Legendre series as

$$F(z') = \sum_{i=1}^{n} a_i P_i(z'), \tag{4.3}$$

where, a_i equals

$$a_i = \frac{2i+1}{i}\int_{-1}^{1} F(z')P_i(z')dz', \tag{4.4}$$

according to Cloude (2006). Here, $P_i, i = 1, 2, ..., n$ are the Legendre polynomials (Cloude, 2007a) and a_i are the corresponding Legendre coefficients. This leads to the following expression for $\tilde{\gamma}$

$$\tilde{\gamma} = e^{j\frac{k_z h_v}{2}} \frac{\int_{-1}^{1}(1 + F(z'))e^{j\frac{k_z h_v}{2}z'}dz'}{\int_{-1}^{1}(1 + F(z'))dz'}, \tag{4.5}$$

To obtain the numerator and denominator of 4.5, function $F(z')$ should be defined according to Cloude (2010). If we can estimate the parameters a_i, we can reconstruct the vertical structure of vegetation layer (Cloude, 2006). This approach is extendable to multi-baseline PolInSAR data, leading to the vertical structure reconstruction with a higher resolution. Equation 4.5 does not take temporal decorrelation into account and it thus results into to over or under estimation of vegetation height (Cloude, 2006, 2008). To overcome this limitation, the RMoG model was proposed (Lavalle et al., 2012; Lavalle and Hensley, 2012, 2015). The equation of the complex coherence by the RMoG model equals

$$\tilde{\gamma} = \frac{\int_0^{h_v} f(z)e^{(jk_z z)}e^{(-\frac{1}{2}(\frac{4\pi}{\lambda})^2\sigma_r^2(z))}dz}{\int_0^{h_v} f(z)dz}, \tag{4.6}$$

where $f(z)$ equals the exponential function in case of the RMoG model (Lavalle and Hensley, 2015). The term $\sigma_r^2(z)$ models temporal decorrelation induced by scatterers movements in the vertical direction, defined as

$$\sigma_r^2(z) = \sigma_g^2 + (\sigma_v^2 - \sigma_g^2)\frac{z - z_g}{h_r}. \tag{4.7}$$

Here, σ_g is the motion standard deviation of surface layer (m) and σ_v is the motion standard deviation of the vegetation layer (m) located at h_r, e.g.

an arbitrary reference height (m) (Lavalle and Hensley, 2012). Solving 4.6 using 4.7 by the method in Lavalle and Hensley (2012, 2015) gives us the final equation of complex coherence by the RMoG model as

$$\tilde{\gamma} = e^{j\varphi_g} \frac{\mu\gamma_g + \tilde{\gamma}e^{-j\varphi_g}}{\mu + 1}, \tag{4.8}$$

where μ is ground-to-volume-ratio and γ_g is the surface coherence defined in Lavalle and Hensley (2015). Recently, we proposed a new model for estimating tree heights using a combination of the PCT structure function and the temporal decorrelation function of the RMoG model. This model was tested on single-baseline P-band data from the Remingstorp test site in Sweden. The results showed that relative error of height estimation decreases from 37.5% by using the RVoG model to 23.7% by using the modified RMoG model, called the RMoG$_L$ model (Ghasemi et al., 2018b). The equation of complex coherence by the RMoG$_L$ model equals

$$\tilde{\gamma} = \exp(jk_v) \frac{\int_{-1}^{1} \exp(1 + F(z')) \exp(jk_v z') \exp(\frac{-1}{2}(\frac{4\pi}{\lambda})^2 \sigma'^2(z'))dz'}{\int_{-1}^{1}(1 + F(z'))dz'}, \tag{4.9}$$

where $k_v = \frac{k_z h_v}{2}$. Here we assumed that $\sigma_g = 0$ and consequently, $\gamma_g = 0$. This assumption is valid if the time interval between images is short, e.g. less than a few hours, and study area is within a dense tropical forests and where the surface is not changing (Lavalle, 2017). Under these assumptions, $\sigma'(z')$ is a function of motion standard deviation of the volumetric layer only and can be obtained as $\sigma'(z') = \sigma(\frac{h_v(1+z')}{2})$. The final form of complex coherence obtained by the RMoG$_L$ model equals

$$\tilde{\gamma} = \frac{e^{j\varphi_g}\tilde{\gamma}e^{-j\varphi_g}}{\mu + 1}. \tag{4.10}$$

Following Cloude (2006); Ghasemi et al. (2018b), 4.9 can be expanded as

$$\begin{aligned} \tilde{\gamma} = & \exp(jk_v)\times \\ & \frac{(1 + a_0)\int_{-1}^{1} A \exp(jk_v z') + a_1 \int_{-1}^{1} P_1(z') A \exp(jk_v z')dz' + ...}{(1 + a_0)\int_{-1}^{1} dz' + a_1 \int_{-1}^{1} P_1(z')dz' + a_2 \int_{-1}^{1} P_2(z')dz' + ...}, \end{aligned} \tag{4.11}$$

with $A = \exp(\frac{-1}{2}(\frac{4\pi}{\lambda}^2)\sigma'^2(z'))$. The matrix form of 4.9 for multi-baseline PolInSAR data equals

$$\begin{bmatrix} F_1^1 A & 0 & F_3^1 A & \cdots & F_{2n-1}^1 A & 0 \\ 0 & F_2^1 A & 0 & F_4^1 A & \cdots & F_{2n}^1 A \\ \vdots & \ddots & \vdots & \vdots & \ddots & \vdots \\ F_1^n A & 0 & F_3^n A & \cdots & F_{2n-1}^n A & 0 \\ 0 & F_2^n A & 0 & F_4^n A & \cdots & F_{2n}^n A \end{bmatrix} \times \begin{bmatrix} a_{10} \\ a_{20} \\ a_{30} \\ a_{40} \\ \vdots \\ a_{2n0} \end{bmatrix} = \begin{bmatrix} Im(\tilde{\gamma_v}^1) \\ Re(\tilde{\gamma_v}^1) - F_0^1 \\ Im(\tilde{\gamma_v}^2) \\ Re(\tilde{\gamma_v}^2) - F_0^2 \\ \vdots \\ Im(\tilde{\gamma_v}^{2n}) \\ Re(\tilde{\gamma_v}^{2n}) - F_0^{2n} \end{bmatrix}, \tag{4.12}$$

where n is the number of baselines and $F_n, n = 1, 2, ...$ are normalized Legendre functions described in (Cloude, 2006). The term $\sigma'^2(z')$ is a scalar unknown parameter to be estimated when solving the equation system. If we summarize 4.12 as $[F_r]\, a = g$, then the unknown parameters are estimated by

$$\hat{a} = [F_r]^{-1}\, g. \tag{4.13}$$

To solve 4.13, we need to determine the number of required Legendre coefficients. This includes choosing the best spatial and temporal set of baselines. Estimation of the unknown parameters is then divided into several steps as described and continues iteratively until convergence is reached.

4.2.4 Single-baseline tomography

To assess the contribution of PCT in increasing the estimation accuracy, the single-baseline tomography with compensation of temporal decorrelation was compared with the conventional RVoG (Cloude and Papathanassiou, 2003) and RMoG models (Lavalle and Hensley, 2015). Equation 4.12 for a single baseline is written as

$$\begin{bmatrix} F_1 A & 0 \\ 0 & F_2 A \end{bmatrix} \times \begin{bmatrix} a_{10} \\ a_{20} \end{bmatrix} = \begin{bmatrix} Im(\tilde{\gamma_v}^1) \\ Re(\tilde{\gamma_v}^1) - F_0^1 \end{bmatrix}. \tag{4.14}$$

Here, we can only estimate two Legendre coefficients and therefore the vertical reconstruction accuracy is limited. After finding the best spatial and temporal baselines, the best baseline is selected and used to solve 4.14.

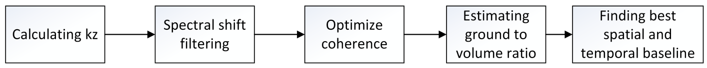

Figure 4.3: The flow of selecting best pair. k_z is the vertical wave number.

4.2.5 Parameter estimation

To find the best spatial and temporal baselines set. We the algorithm shown in Figure 4.3 and explained in Lavalle et al. (2016a).

As the next step, we estimated the unknown parameters. We assigned a random value between 0 and 1 to A. The remaining parameters, are estimated by solving 4.12. We start by adding the maximum possible number of Legendre coefficients that can be estimated using all images. Starting with seven full polarimetric images we added two more coefficients for each different channel resulting into $2np$ coefficients, where n is the number of baselines and p is the number of polarization channels. The Legendre normalized functions from f_1 to f_{2np} are calculated and used for obtaining the condition number of matrix F (Cloude, 2006). The condition number specifies if a matrix problem is ill-posed and therefore if the inversion procedure is prone to error. We reduced the number of Legendre function one by one and computed the condition number at each step. We stopped when the condition number is below a pre-defined threshold, given by the $Cram\acute{e}r - Rao$ bound (Seymour and Cumming, 1994; Touzi et al., 1999).

After obtaining the optimum number of parameters and their estimates, we estimated tree height, ground phase and, at a later step, the motion standard deviation. For validating the final results, the Lidar height map was used as the reference data. We plotted histograms of the obtained and reference height maps. For 36 Regions of Interest (RoIs) covering the full image and dispersed uniformly over the image, height values were compared point to point with the reference height map and the average RMSE for each region was obtained.

4.3 Results

The spatial resolution of each image used in this study is approximately 1.66 m in the range and 1 m in the azimuth direction. The Pauli RGB image of the study area, the obtained vertical wave number and the synthetic interferograms are presented in Figure 4.4. The synthetic interferograms are generated based on orbital information of the sensor and topographic component of the scene extracted from a DEM. The phase component of the interferograms is calculated.

We created interferograms for every possible baselines. The generated interferograms of a randomly selected pair are shown in Figure 4.5.

Next, we optimized the coherence based upon flattened interferograms and we calculated k_z.

Following Figure 4.2, the next step is to optimize coherence for all possible image pairs displayed in Figure 4.6. The optimized coherence of images

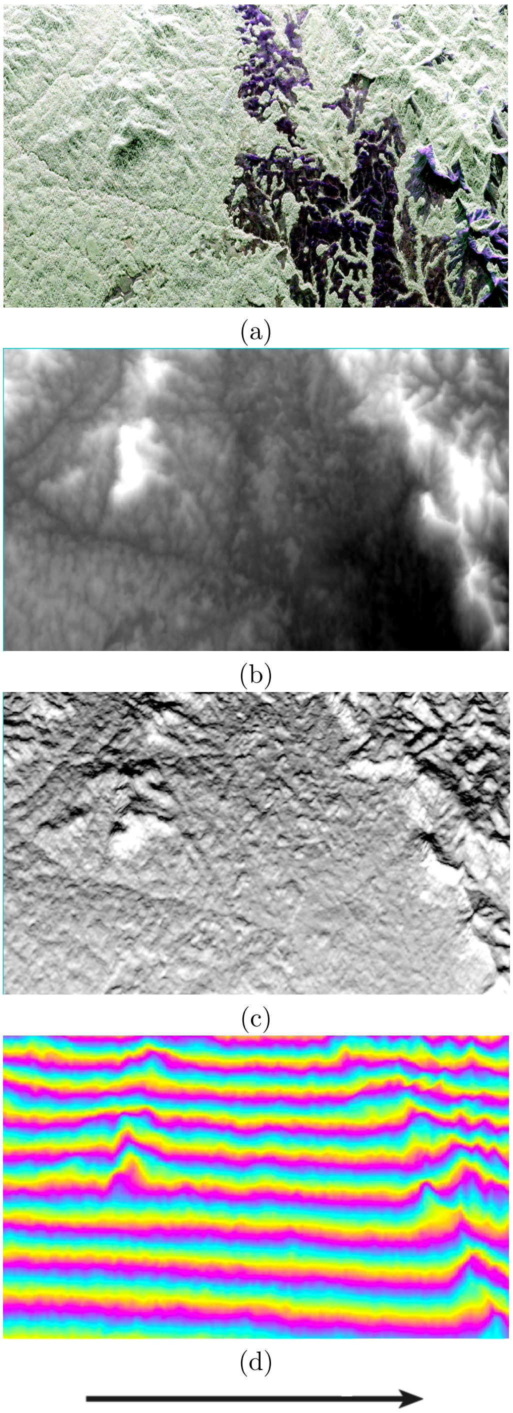

(a)

(b)

(c)

(d)

Figure 4.4: (a) The Pauli RGB image, (b) SRTM DEM, (c) vertical wavenumber, and (d) synthetic interferograms from the selected area of La Lope national park in Gabon calculated based on the ancillary data (Lavalle, 2017). The latitude and longitude of the top left corner coordinates are: 0.154197 W and 11.536575 N. The number of pixels are 600×1000 and each pixel has a size of 1.66×1.66 m^2. The black arrow shows the azimuth direction.

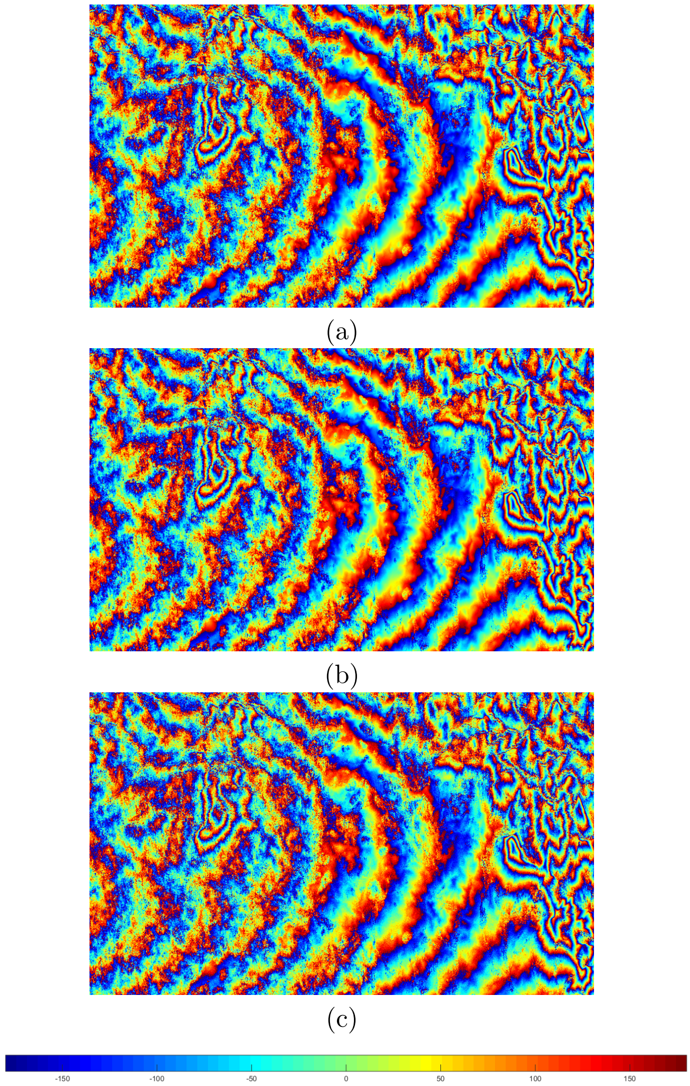

Figure 4.5: The flattened interferograms of images 1 and 2 after correcting for flat earth phase and spectral-shift filtering: (a) $HH--HH$, (b) $HV--HV$, and (c) $VV--VV$. The latitude and longitude of the top left corner coordinates are: 0.154197 W and 11.536575 N. The number of pixels are 600×1000 and each pixel has a size of 1.66×1.66 m^2.

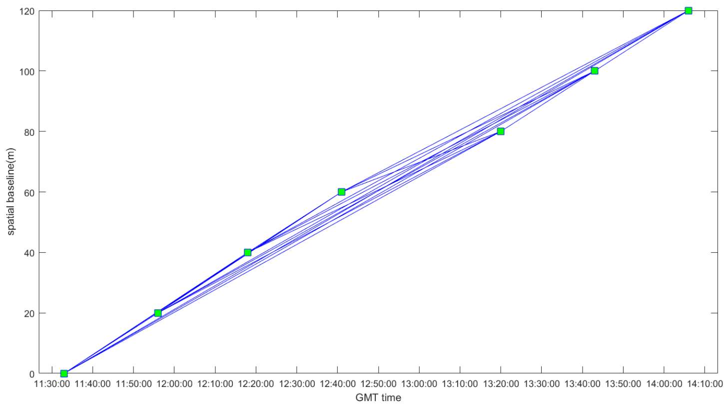

Figure 4.6: The plot of the 21 possible baselines. The green squares are acquired SAR images and blue lines are possible baselines. The best baselines are selected based on both spatial and temporal intervals.

marked with numbers 1 and 2, are displayed in Figure 4.7. Then the volume and the surface dominated channels are determined according to the method explained in **?**. After determining the volume dominated γ_v and surface dominated γ_s channels, the initial values of h_v and φ_g were estimated using the equations described in Cloude (2006). This is followed by obtaining k_v for each pixel. The complex coherence of each arbitrary polarization channel ($\tilde{\gamma}(w)$) was normalized by

$$\tilde{\gamma} = \tilde{\gamma}(w)\exp(-jk_v)\exp(-j\varphi_g). \tag{4.15}$$

Starting with $2 \times 3 \times 7 = 42$ coefficients by solving 4.12, we estimated the normalized Legendre functions f_1^1 to f_{42}^{21}, as described by Cloude (2006, 2010). We summarize 4.12 as $\hat{a} = [F_r]^{-1} g$. If a satisfies

$$||\frac{\partial a}{a}|| \leq \frac{k_v^2(\gamma_v^2 - 1)}{\sqrt{2L}(3\cos k_v - (3 - k_v^2)\frac{\sin k_v}{k_v})}, \tag{4.16}$$

where L is the number of looks (Cloude, 2006), the computations stop, otherwise, one PolInSAR pair is removed and the process is repeated (Cloude, 2006). In order to select the baseline that should be removed first, all possible pairs are ranked based upon the temporal and spatial intervals. The best image pairs are those that have the shortest temporal and longest spatial baseline. Therefore, removing baselines starts from pairs that have the longest temporal and shortest spatial baselines. Removing a pair and re-calculating 4.12 was repeated until the coefficients matrix satisfies 4.15. Then the structure function was defined according to the optimum number of selected baselines. Figure 4.8 shows the height map obtained by solving (13) and the structure functions for different pixels.

The order of the structure function for the whole area changes between zero for pixels with vegetation cover shorter than 10 m and seven for pixels

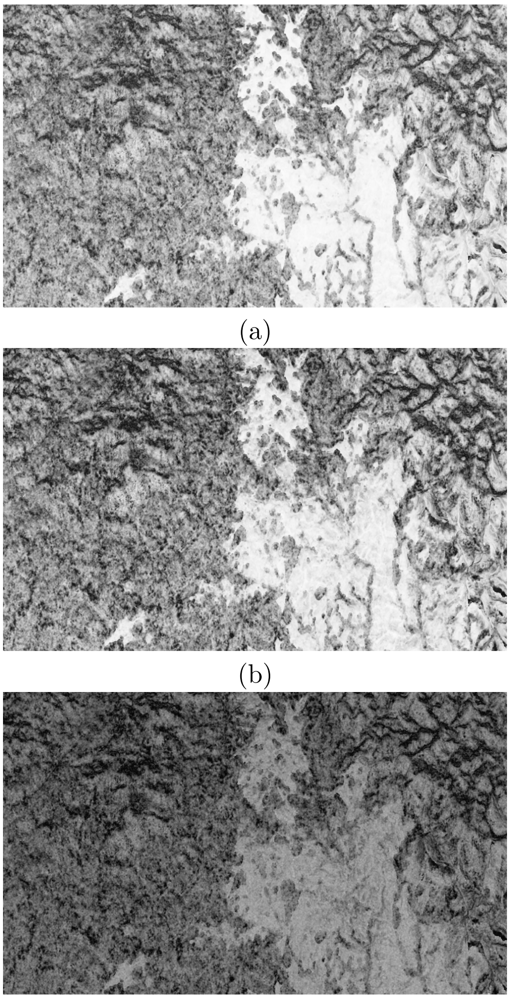

(a)

(b)

(c)

Figure 4.7: The magnitude of first three components of optimized coherence between images 1 and 2. The latitude and longitude of the top left corner coordinates are: 0.154197 W and 11.536575 N. The number of pixels are 600×1000 and each pixel has a size of 1.66×1.66 m^2.

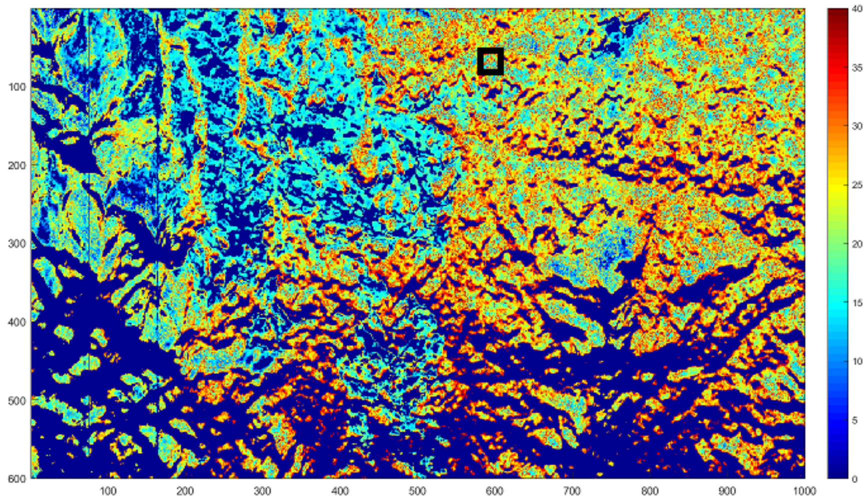

(a)

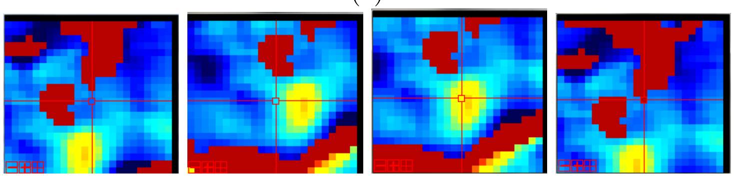

(b) (c) (d) (e)

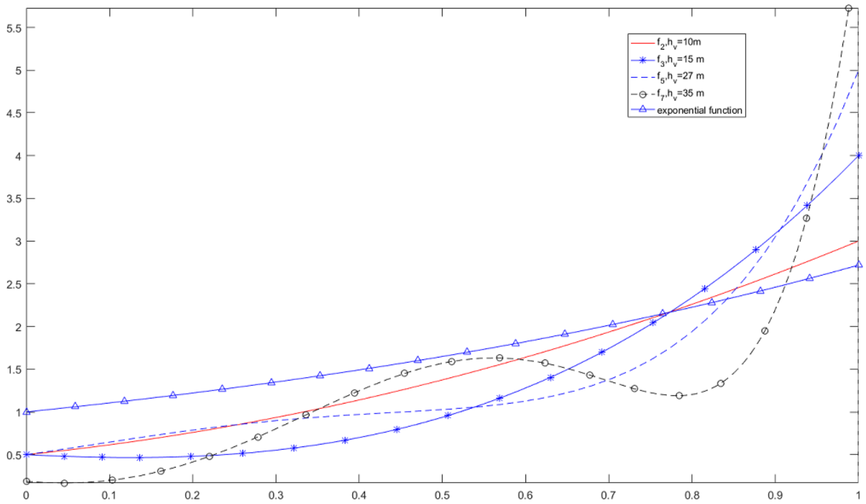

(f)

Figure 4.8: (a) Obtained height map from applying modified PCT model. The latitude and longitude of the top left corner coordinates are: 0.154197 W and 11.536575 N. The number of pixels are 600×1000 and each pixel has a size of 1.66×1.66 m^2. The area selected by black rectangle is magnified in Figures 4.8(b)– 4.8(e). The cross-hair points out pixels with: (b) $h_v = 10m$, (c) $h_v = 15m$, (d) $h_v = 27m$, (e) $h_v = 35m$ inside the black rectangle, and (f) structure functions for the selected pixels shown by cross-hair vs. the exponential function of the RMoG model.

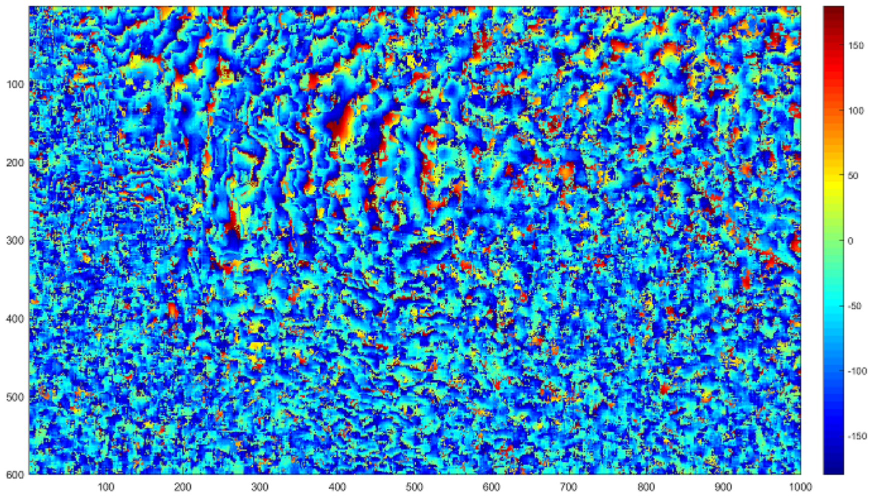

(a)

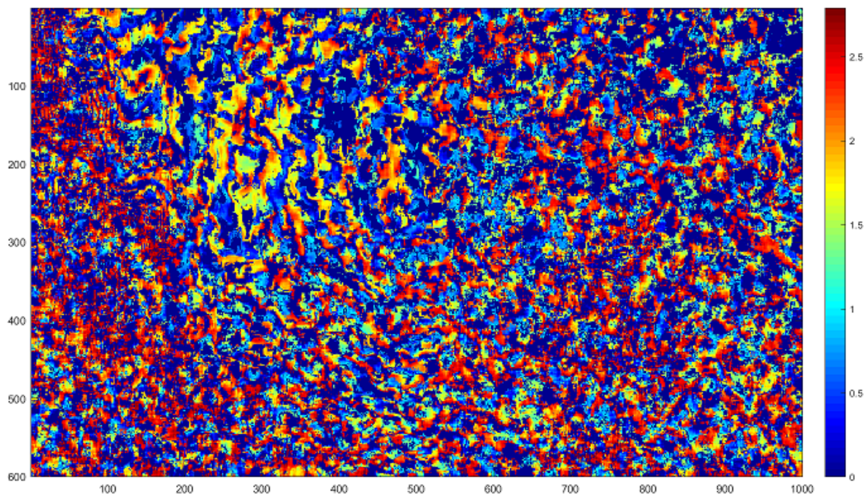

(b)

Figure 4.9: (a) Topographic phase and (b) k_v resulting of applying multi-baseline height estimation with compensation of temporal decorrelation. The latitude and longitude of the top left corner coordinates are: 0.154197 W and 11.536575 N. The number of pixels are 600×1000 and each pixel has a size of 1.66×1.66 m^2.

with tree heights taller than 30 m. The estimated structure function is plotted in Figure 4.8 where the exponential function shows the extremes of the structure function not necessarily occurring at the top of the canopy layer. It shows in particular multi-layer complex vertical structures in the vegetation layer. The resulting topographic phase and k_v are shown in Figure 4.9.

Table 4.2: The average RMSE values and correlation coefficients for two different height estimation models.

	Regular PCT	Modified PCT
Average RMSE (m)	7.5	5.6
R^2	0.65	0.70

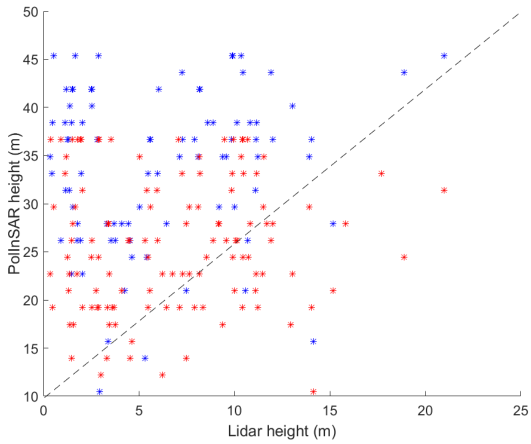

Figure 4.10: The scatter plot of the heights derived by regular PCT (blue points) and modified PCT (red points) vs. Lidar heights. The $R^2 = 0.65$ for regular PCT and $R^2 = 0.75$ for modified PCT.

As a comparison, the regular PCT method in Cloude (2006) was applied. For a point-to-point comparison between the heights obtained from the modified PCT and the regular PCT models, the RoIs are used. Average values inside each region were compared to corresponding values on reference height map. The average RMSE for all regions and R^2 values are listed in Table 4.2.

The scatter plot of the average height values inside the RoIs resulting from regular and modified PCT models versus Lidar height values are plotted in Figure 4.10. We observe that results from both height estimation models have a positive correlation with Lidar data. Also, the correlation between PolInSAR and Lidar height increased after modeling temporal decorrelation. We finally observe that the height values of the modified PCT model better coincide with the Lidar heights.

For providing a visual comparison between Lidar height map and height resulting from the modified PCT model, the Lidar height map is shown in Figure 4.11.

We see that the modified PCT model overestimates the height if the vegetation cover is short, especially in the middle part of image. Meanwhile the height of taller trees in the right part of image are underestimated by the modified PCT model. This is confirmed by the histograms (Figure 4.12).

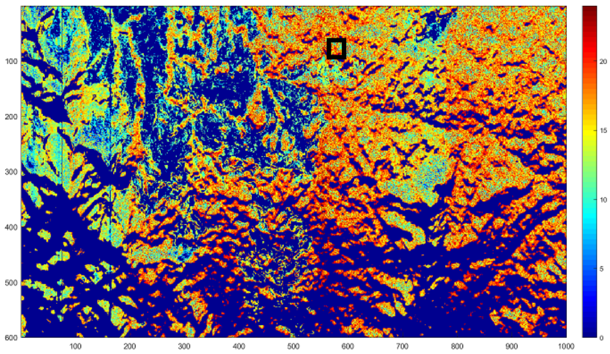

Figure 4.11: Lidar height map. Selected area is the one shown on Figure 8(a) as well. The latitude and longitude of the top left corner coordinates are: 0.154197 W and 11.536575 N. The number of pixels are 600×1000 and Lidar data is re-sampled to have similar pixel size as the PolInSAR images

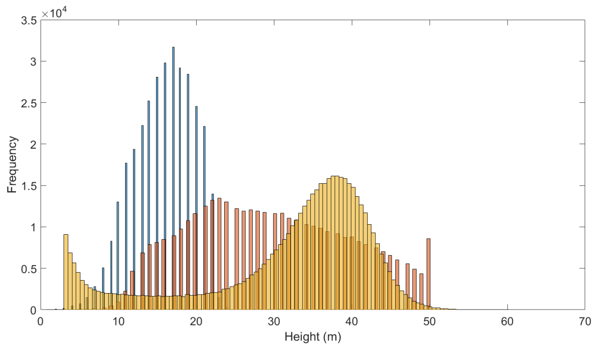

Figure 4.12: Histogram of obtained height maps and Lidar reference heights. blue: PCT, red: modified PCT, yellow: Lidar height.

Table 4.3: The average RMSE values and correlation coefficient for single-baseline tomography, Vs. the RVoG and RMoG models.

	RVoG	RMoG	Single-baseline modified PCT
Average RMSE (m)	9.8	8.5	7.8
R^2	0.57	0.68	0.60

The results of single baseline tomography are compared to the RVoG and RMoG models in Figure 4.13. The RMSE and R^2 values are listed in Table 4.3. Relatively large differences occur between single-baseline tomography and RVoG model, whereas differences with the RMoG model are small. This is because the RVoG model ignores any temporal decorrelation. The RMSE and correlation coefficient clearly show the contribution of multi-baseline PCT modeling in improving height estimation accuracy.

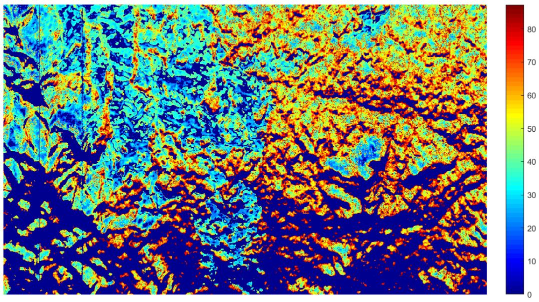

(a)

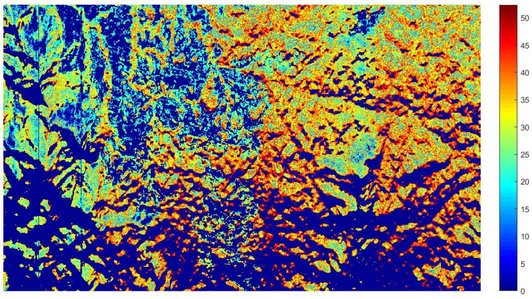

(b)

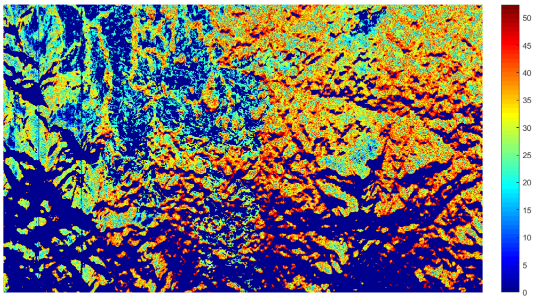

(c)

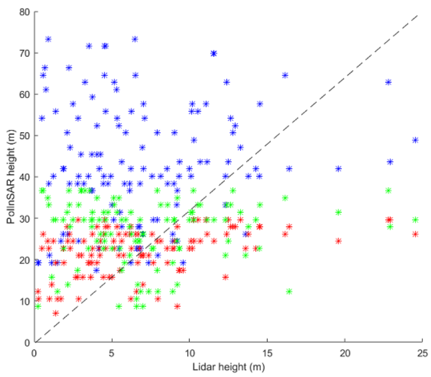

(d)

Figure 4.13: The height map resulting of (a) RVoG, (b) RMoG, and (c) single-baseline tomography with compensation of temporal decorrelation. The latitude and longitude of the top left corner coordinates are: 0.154197 W and 11.536575 N. The number of pixels are 600×1000 and Lidar data is re-sampled to have similar pixel size as the PolInSAR images. (d) The scatter plot of RVoG (blue), RMoG (red) and single-baseline tomography with compensation of temporal decorrelation (green).

4.4 Discussion

Tree height estimation using full polarimetric SAR images is challenging due to temporal decorrelation. This chapter shows that neglecting temporal decorrelation leads to error in height estimation when using the PCT model. Mitigating the decorrelation source becomes important if the estimated heights are used for obtaining other biophysical parameters i.e. biomass. This can be severe, as according to the past studies (Askne et al., 2013), biomass is exponentially related to height.

The obtained RMSE values are still relatively large. Previous studies have shown that an accuracy of 2 m was obtained by using PolInSAR data in deciduous, boreal and hemi-boreal forests (Praks et al., 2007). Other studies (Huang et al., 2011; Kugler, 2015; Florian et al., 2006; Hajnsek et al., 2009) suggest that the final accuracy is related to the wavelength, structure of trees and density of the vegetation cover in tropical forests (Tebaldini et al., 2011; Minh et al., 2014). The relatively large RMSE value obtained in our study could be due to several reasons. First, the L-band is not penetrating enough to the bottom of the vegetation layer. There are some studies investigating the ability of L- and P-bands to penetrate and represent the vertical structure for example Pardini et al. (2018). This study compares P- and L-band PolInSAR data to Lidar by ground-to-volume ratio and performance of the systems. Second, the number of Legendre coefficients is insufficient to estimate the height with a high accuracy. Third the hilly terrain of the study area may affect theresults although we corrected for topographic phase and masked out the steep slopes at the test site following Minh et al. (2014); Mercer et al. (2009); Woodhouse et al. (2003). Using multi-baseline tomographic data and accounting for local incidence angle reduces the topographic effect on estimating height. The topography error, however, is larger in P-band (Minh et al., 2014). If we could test the suggested model on P-band images from the same area, the effect of topography and other sources of errors might become more clear. According to the height maps, the result of the regular PCT model are affected by temporal decorrelation, especially for taller trees. This is similar to the results of previous studies (Cloude, 2006). Another interesting observation from Figure 4.13 is that both the regular and the modified PCT model overestimate the height for small trees and underestimate it for tall trees. Overestimation of short trees has been observed in previous studies (Cloude, 2008). It can be explained by using a constant temporal decorrelation function for all the image pairs and using a first order estimation for objects movements while the decorrelation may change from one pair to another. the This error is also visible when comparing single-baseline modified PCT with the RVoG and RMoG models in Figure 4.13(d).

A challenge we faced was the large computation time and the complexity of the equation system. We have more parameters than observations and often inversion becomes ill-posed (Lavalle and Hensley, 2015). One suggestion for overcoming the instability is repeating the solution process several times and comparing the results after each iteration. The process will stop if the difference values of the objective function between two iteration becomes

smaller than a pre-specified threshold. Using a threshold of 10^{-4} as suggested in (Lavalle and Hensley, 2015), the average number of iterations in this chapter was 45. Application of an iterative estimation process is necessary but not sufficient to guarantee robust parameter estimation. Initial values for unknown parameters should be selected from a meaningful physical range to ensure that the outcome is acceptable. Moreover, it is important to define a suitable threshold for the condition number of the matrix since the accuracy of height estimation depends on the inversion of an approximately diagonal matrix. Another problem with using multi-baseline SAR data with or without compensation of temporal decorrelation is the sensitivity to noise (Cloude, 2006; Lavalle and Hensley, 2015). Further, we changed the structure function independently from the motion standard deviation function according to Lavalle and Hensley (2012). The first order estimation of the object movements has shown good results in boreal forests. In tropical forests, however, we may need more accurate estimation of the movements of the objects. Using higher order functions for modeling vertical movements needs additional observations and requires more complex calculation.
Another important point is the role of coherence optimization in solving the equation system. The main role of the optimized channels is to isolate the volume and surface representations. Note that the linear combination obtained from the Pauli basis polarization are dependent, although each represents different physical properties of the scatterers. For example HH$-$VV, the double-bounce scattering, amplifies di-hedral scattering contributions and represents interaction between tree volume and the ground layer, while HH+VV amplifies surface scattering contributions and represents single bounce scattering coming from the surface layer. Thus they have been treated as independent observations in literature like in Lavalle and Hensley (2015). However, as the estimates of the interferometric coherences at the different polarizations are affected by uncertainty, multiple polarizations combinations can be used for a more accurate estimation using Least Squares technique. Ideally, we should have the linear and circular basis polarization channels measured by the sensor or have another type of observation. Alternatively we could add adding constraints to the equation system to estimate the unknown parameters. This, however, is not straightforward and requires more research.
Two main assumptions in this study are limiting when generalizing our findings. First the time intervals between images should be short enough to have similar weather condition in all PolInSAR pairs. Moreover, the difference between the look angles of different baselines should be small. Second, the surface layer should not change during image acquisition time thus $\sigma_g = 0$. We balanced the generality of temporal decorrelation with the definition of a vertical layer structure function that is more accurate by making these assumptions. These assumptions automatically make data acquisition limited to interferometric pairs that belong to similar weather condition and are preferably captured during a single day. A more general case of the multi-baseline PolInSAR data processing along with similar temporal decorrelation model can be found in Lavalle and Khun (2014), where the vertical structure function is the general Gaussian function. This specifies a dilemma between

generality and accuracy when choosing a height estimation method.
For examining the performance of the RMoG and modified PCT models in estimating temporal decorrelation one pair of zero spatial baseline PolInSAR images has to be acquired from the same area. In this case the complex coherence includes mainly temporal decorrelation. This was not possible in our study since we used the data from a previous campaign. Fortunately, it has been tested in Lavalle and Hensley (2012) and results showed good agreement with the RMoG model outcome. Finally, the temporal decorrelation is affected by the movement of the vegetation layer induced by the wind. This is a limitation of the RMoG and the modified PCT models because other decorrelation sources i.e. changes in seasonal and moisture content are not taken into account. Additional studies have concentrated on modelling other sources of temporal decorrelation (Lee et al., 2013). This can serve as an interesting point of departure for future studies in a PolInSAR data processing.

4.5 Conclusions

In this chapter, we combined the PCT model with the temporal decorrelation component from the RMoG model to estimate tree height. The modified PCT model was tested on a SAR tomographic stack available from the La Lope national park in Gabon. The modified PCT model improved the accuracy of height estimation compared to regular PCT. Moreover, the structure function was different for different regions on the image. Therefore using the same exponential function for the whole image is a sub-optimal choice. This means that for a complex structure e.g. tropical forests, we need to use a specialized structure function according to the vertical structure of the area. Main challenges are a heavy computation task and a larger number of unknown parameters than observations. The importance of temporal decorrelation and the use of an optimized structure function based upon the vegetation layer structure, are useful for future satellite missions that estimate tree heights and monitor forests.

5

Assessment of Forest Above-Ground Biomass Estimation from PolInSAR in the Presence of Temporal Decorrelation

This chapter is based on the published paper: Ghasemi, N., Tolpekin, V. and Stein, A., (2018). Assessment of Forest Above-Ground Biomass Estimation from PolInSAR in the Presence of Temporal Decorrelation. Remote Sensing, Volume:10, Issue: 6, PP.815.

Abstract

In forestry studies, remote sensing has been widely used to monitor deforestation and estimate biomass, and it has contributed to forest carbon stock management. A major problem when estimating biomass from optical and SAR remote sensing images is the saturation effect. As a solution, PolInSAR offers a high coverage height map that can be transformed into a biomass map. Temporal decorrelation may affect the accuracy of PolInSAR and may also have an effect on the accuracy of the biomass estimates. In this study, we compared three different height estimation models: the Random-Volume-over-Ground (RVoG), Random-Motion-over-Ground (RMoG), and Random-Motion-over-Ground-Legendre (RMoG$_L$) models. The RVoG model does not take into account the temporal decorrelation, while the other two compensate for temporal decorrelation but differ in structure function. The comparison was done on 214 field plots of the 10 m radius of the BioSAR2010 campaign. Different models relating PolInSAR height and biomass were developed by using polynomial, exponential, power series, and piece-wise linear regression. Different strategies for training and test subset selection were followed to obtain the best possible regression models. The study showed that the RMoG$_L$ model provided the most accurate biomass predictions. The relation between RMoG$_L$ height and biomass is well expressed by the exponential model with an average RMSE equal to 48 ton ha^{-1} and R^2 value equal to 0.62. The relative errors for estimated biomass were equal to 46% for the RVoG model, to 37% for the RMoG, and to 30% for the RMoG$_L$ model. We concluded that taking the temporal decorrelation into account for estimating tree height has a significant effect on providing accurate biomass estimates.

Keywords: biomass; temporal decorrelation; PolInSAR height; accuracy; RVoG model; RMoG model; RMoG$_L$ model.

5.1 Introduction

Forest biomass monitoring is important for several reasons: the critical role of forests on carbon stock and flux, quantification of the effect of deforestation on greenhouse gas emissions, and its use as an indicator of land cover change in UN-FAO's national statistics (Le Quéré et al., 2015; Houghton et al., 2012; Stocker et al., 2013). Remote sensing has been widely used in past decades to estimate biomass, monitor deforestation, and carbon stock management (Lu et al., 2016; Roy and Ravan, 1996; Drake et al., 2003).

Remote sensing for estimating biomass can be divided into two-dimensional and three-dimensional methods. Two-dimensional methods use optical reflectance or SAR backscatter and relate it to biomass using regression (Le Toan et al., 1992; Yu and Saatchi, 2016; Gizachew et al., 2016). Satellites such as LANDSAT and MODIS have been used for this purpose (Lu, 2005; Muukkonen and Heiskanen, 2007). The main problem with these methods is that the signal is insensitive to the increase of biomass above a certain level, i.e. the saturation effect. Therefore, they can only be used for areas with low biomass such as savannas (Gizachew et al., 2016). In the case of using SAR data, they can be extended to medium-level biomass if L and P band or multi-temporal SAR data is used (Rauste, 2005; Montesano et al., 2013; Santoro et al., 2015; Garestier et al., 2005). In contrast, biomass estimation using three-dimensional methods is more accurate since forest biomass is strongly related to the vertical structure of the trees (Dubayah et al., 2010; Yao et al., 2011; Mette et al., 2004; Sexton et al., 2009). Airborne and space-borne Lidar can provide an accurate height map of the forested areas that later can be converted into a biomass map (Næsset, 2002; Dubayah et al., 2010; Ni-Meister et al., 2010). In some studies, ground-based Lidar has been used to obtain biomass map as well (Yao et al., 2011; Nelson et al., 2017). Other means of acquiring a height map are photogrammetry, Interferometric SAR (InSAR) and Polarimetric Interferometric SAR (PolInSAR) (Lavalle et al., 2008; Neumann et al., 2011). PolInSAR records the reflected SAR signal from the same objects from two different points in two different times (Cloude and Papathanassiou, 1998b). InSAR and PolInSAR give a height map of a lower accuracy than Lidar, but they cover large areas and can be used under all weather conditions (Hyde et al., 2007; Rahlf et al., 2014). InSAR can produce a tree height map in two ways, e.g., by subtracting a DEM from InSAR height or by using dual-wavelength InSAR i.e., TanDEM-X and E-SAR (Sexton et al., 2009; Neeff et al., 2005; Rombach and Moreira, 2003).

More advanced techniques such as TomoSAR and fusion of LiDAR and InSAR have also been used to estimate biomass (Minh et al., 2014, 2016; Sun et al., 2011). These techniques provide more accurate results as compared to InSAR. The height estimation accuracy of PolInSAR and TomoSAR is directly affected by the presence of temporal decorrelation (Lavalle and Hensley, 2015; Le Toan et al., 2011; Ahmed et al., 2011). Temporal decorrelation is the change in SAR signal reflected from the objects changes in the position or attributes during the image acquisition time (Zebker and Villasenor, 1992). We may thus expect that the accuracy of biomass estimation improves after mitigating the temporal decorrelation. Recently, the Random-Motion-over-Ground (RMoG) model has been proposed to compensate the effect of temporal decorrelation on height estimation using PolInSAR. This model is based upon the RVoG model combined with modeling motion of trees in the vertical direction. It has shown promising results in improving height estimation accuracy up to 20% (Lavalle et al., 2012; Lavalle and Hensley, 2015). We have proposed the Random-Motion-over-Ground-Legendre (RMoG$_L$) model based on the RMoG model, but with the Fourier–Legendre series as the structure function instead of the simple exponential function used in the RMoG model (Ghasemi et al., 2018a).

The main objective of this chapter is to analyze the accuracy of biomass estimation after correcting for temporal decorrelation. To do so, the first step is to develop a model to estimate biomass from PolInSAR height maps resulting from the Random-Volume-over-Ground (RVoG), RMoG, and RMoG$_L$ models. We have selected the Remningstorp forest as a study area as it has been studied during BioSAR2010 campaign (Ulander et al., 2011b) as the test site. Both linear and non-linear models were developed to clarify the relation between PolInSAR height and biomass. The second step is to apply different strategies for train and test dataset selection to make sure that the chosen model is general and accurate enough (Reitermanova, 2010). At the final step, for evaluating the results both field data and Lidar data were used.

This chapter has been organized in the following sections: first, a short introduction of biomass estimation using remote sensing in general and SAR data specifically is given. Second, the dataset and study area is characterized. In the third section, explanation of the methodology is given. In the fourth section, the results are presented followed by the discussion and the conclusion sections.

5.2 Materials and Methods

A summary of the methodology used in this study is presented in Figure 5.1. Hereafter, the methodology is described in details.

5.2.1 Study Area

A complete report about the BioSAR2010 campaign and Remningstorp area has been published previously (Ulander et al., 2011b). Here, a summary is provided that is relevant for this study. The Remningstorp forest (58°30′N, 13°40′E) is located in the southwestern part of Sweden and has an area of approximately 1200 ha. The forest type is hemi-boreal, which intermediates between boreal and temperate forest types (Askne and Santoro, 2012). Dominant forest species are *Norway Spruce* and *Scots pine*, and it is completed by a mixture of *oak*, *birch*, and *aspen*. The elevation range of this area is between 120 and 145 m above sea level.

5.2.2 Field and Lidar Data

Field observations used in this study have been collected resulting in 214 circular plots with a radius of 10 m (Ulander et al., 2011a). The location of these field plots is shown in Figure 5.2. The area has been divided into several

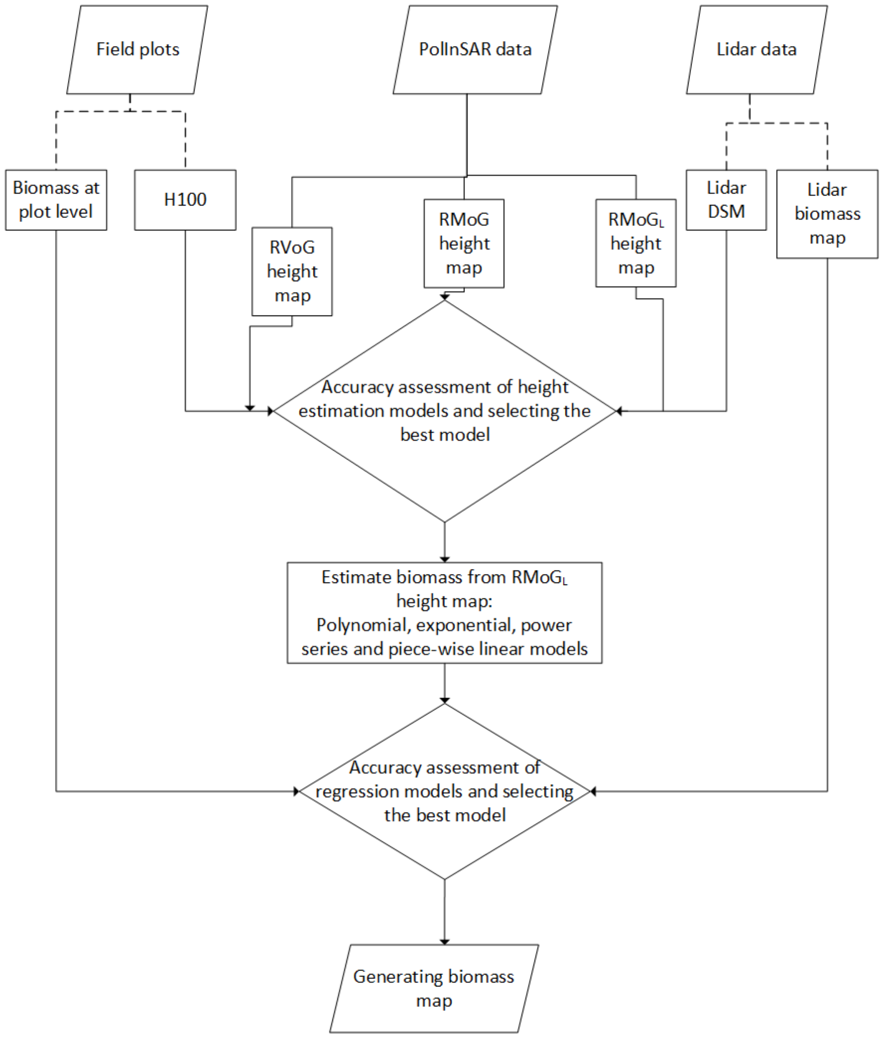

Figure 5.1: Flowchart of the biomass estimation methodology.

stands based upon the homogeneity of forest cover type. Field plots have been defined in such a way that they fall into one of these stands completely to minimize the effect of heterogeneity within the plots. Measurements inside each plot according to the Heureka forestry system (Wikström et al., 2011) include an H100 height, defined as the basal area weighted average of the 10 highest trees in each plot (Mette et al., 2004), Diameter at Breast Height (D_{BH}), that is defined as the diameter at 1.3 m above ground, and the

Figure 5.2: Location of field plots on Remningstorp area image. Google earth V 6.0. Remningstorp, Sweden. The center coordinates are: 58°30′ N and 13°40′ E, and the area is 1200 ha. Eye alt 3.58 km.

dominant tree species. According to the recorded information, 60% of the field plots is covered by spruce, 30% covered by pine, and 10% dominated by oak, birch, and aspen (mixed deciduous) trees. Additionally, dry aboveground biomass, including stems, branches, bark, and needles, has been measured (Ulander et al., 2011a). For all 10 m radius field plots, biomass was between 6 and 250 ton ha^{-1} with an average of 105 ton ha^{-1}. The allometric equation used for measuring biomass is based upon height and D$_{BH}$ (Muukkonen and Heiskanen, 2007). Allometric equations are the equations that relate biophysical parameters to biomass. At the plot level, the general form of this equation equals

$$B = N\pi \left(\frac{1}{2}D_{BH}\right)^2 H\rho f \tag{5.1}$$

where B is the above-ground biomass, N is the number of trees per area unit, H is the tree height, ρ is the species-related wood density, and f is a form factor. These equations have been developed for different forests according to the FAO standard procedure (Picard et al., 2012). Developing these equations requires excessive field work and the data are only valid for a 5-year period. After this period, the density and the factor f change, so the measurements are repeated every five years. In this chapter, we used the previously developed allometric equations for the test site (Ulander et al., 2011b). Lidar data of the study area were acquired with an average density of 69 returns m^{-2}. The airborne Lidar data has been used for two main purposes. First for evaluating height estimation models i.e., the RVoG, RMoG, and RMoG$_L$ models. Second, the biomass map produced from Lidar data (Næsset, 2002; Ulander et al., 2011b; Askne et al., 2013) was used for the assessment of generated biomass maps from PolInSAR heights beside the field data. The predicted biomass map from Lidar height is presented in

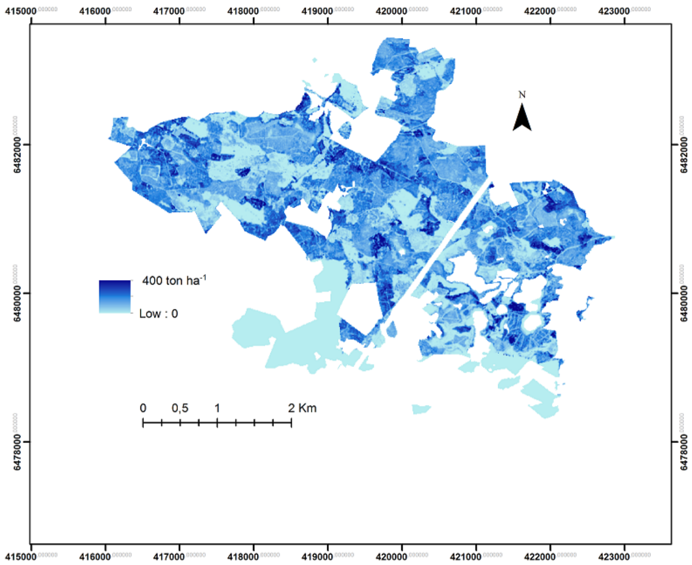

Figure 5.3: Predicted biomass map by Lidar data provided within campaign field data (Ulander et al., 2011b).

Figure 5.3. Besides predicting the biomass map, we used the Lidar Digital Surface Model (DSM) with a cell size of 0.5×0.5 m, as the reference height map. Since we have the canopy height map, the Lidar DSM is called the Canopy-Height-Model (CHM) hereafter. This map was derived from the differences between the first and the last returns of the Lidar pulses and is displayed in Figure 5.4. Both the predicted biomass map and the CHM have been used as the reference data sets. The areas with zero height values on the Lidar CHM are masked on the predicted biomass map. The areas with taller trees on the Lidar CHM correspond to areas with the highest biomass values. The two maps show a clear positive correspondence between tree height and biomass.

5.2.3 PolInSAR Data

During the BioSAR 2010 campaign, 10 PolInSAR images were obtained. These images were collected with the ONERA SETHI airborne sensor, developed by the Office National d'Etudes et de Recherches Aérospatiales (ONERA) (Ulander et al., 2011b). This device can acquire full Polarimetric Interferometric SAR images in both L and P bands.

Three pairs of P-band images, acquired specifically for PolInSAR analysis, were chosen for this study. Their spatial baseline is equal to 30 m, the heading angles equal 199°, 178°, and 270°, respectively, and the sensor height is approximately equal to 4000 m. The images have been delivered in SLC (Single Look Complex) format and have four polarization channels: HH, HV, VH, and VV with $HV = VH$ as the system is mono-static. The

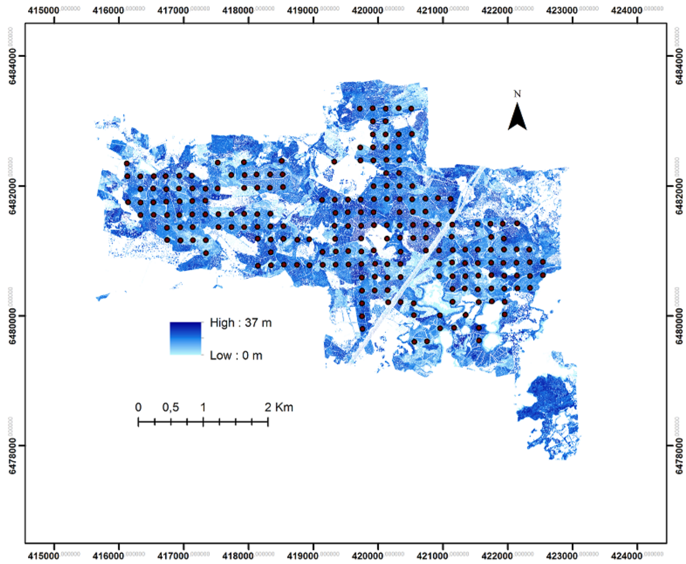

Figure 5.4: Available CHM from Lidar of the Remningstorp area. Dark circles show the location of field plots.

ground-range resolution of the InSAR data is 0.5×0.5 m.

Next, after correcting for the flat earth phase (Goldstein et al., 1988), the complex coherence was obtained according to Cloude and Papathanassiou (1998b). The optimized coherence channels plus linear polarizations (HH, HV, and VV), circular polarization (LL, LR, and RR), and the Pauli basis polarization ($HH+VV$ and $HH-VV$) channels (Lee and Pottier, 2009) served as input for the RVoG, RMoG, and RMoG$_L$ models. These models are applied on each pair of P-band images separately and the final height maps are generated by mosaicing the resulting images.

5.2.4 Tree Height Estimation Using PolInSAR Data

Since the Polarimetric Interferometric SAR systems illuminates an area from two different positions at two different times, any change in the objects is represented in the form of signal decorrelation. Thus, the height of the trees, like other properties, can be retrieved by reversing the process of interferograms generation, e.g., quantifying the decorrelation sources. In the past decade, the models used for obtaining tree properties were only taking volumetric decorrelation into account. Volumetric decorrelation is the inconsistency of the signal caused by the vertical structure of the trees. In the presence of natural phenomena in particular wind, changes in the position of the scatterers cause temporal decorrelation. This should be taken into account when estimating tree height. The following models have been applied to estimate height without and with accounting for temporal decorrelation.

5.2.4.1 The RVoG Model

The RVoG model has been popular over the past decade for estimating forest height (Dobson et al., 1995; **?**; Cloude, 2010). It relates the observed complex coherence to the height of the vegetation layer with the assumption that only volumetric decorrelation is present. It expresses the volumetric coherence γ_v, as

$$\gamma_v = \frac{e^{j\varphi_g}}{\mu+1}\left[\mu + \frac{p_1\left(e^{h_v p_2}-1\right)}{p_2\left(e^{h_v p_1}-1\right)}\right] \tag{5.2}$$

where φ_g is the ground phase, h_v is the vegetation height, and μ is the ground-to-volume-ratio (Cloude and Papathanassiou, 2003). The parameter μ is added to compensate for the surface scattering mechanism effects on the observed coherence. It can have any value between 0 and ∞ (Cloude and Papathanassiou, 2003). The parameters p_1 and p_2 are defined as

$$p_1 = \frac{2K_e}{\cos\left(\theta-\theta_s\right)} \tag{5.3}$$

$$p_2 = p_1 + jk_z \tag{5.4}$$

where K_e is the mean wave extinction coefficient ($0 < K_e < 1$), θ is the average look angle ($0 < \theta < 90°$), θ_s is the terrain slope angle ($0 \leq \theta_s \leq 90°$), and k_z is the vertical wave number ($0 < k_z < 1$). The final form of complex coherence by the RVoG model γ_R is

$$\gamma_R = e^{j\phi_g}\frac{\gamma_v+\mu}{1+\mu}. \tag{5.5}$$

To solve (5.5), we need to estimate μ, so we need a polarization channel as the volume and another channel as the ground scattering representation. Solving (5.2)– (5.5) is done with a multi-stepwise procedure following Cloude and Papathanassiou (2003). As the RVoG model ignores temporal decorrelation, it provides biased results if the temporal decorrelation is high. This can happen due to wind or precipitation. To tackle this limitation, the RMoG model has been proposed (Lavalle et al., 2012), which models the induced motion caused by wind in the vertical direction.

5.2.4.2 The RMoG Model

The RMoG model assumes that the vegetation layer consists of randomly distributed vertical scattering objects located on a rough dielectric layer. The main difference with the RVoG model here is to assume that both layers have random movements along the vertical axis (Lavalle and Hensley, 2015). The complex coherence using the RMoG model γ_M is obtained as

$$\gamma_M = \frac{\int_0^{h_v}\rho\left(z\right)\exp(jk_z z)\exp\left(-\frac{1}{2}(\frac{4\pi}{\lambda})^2\right)\sigma_r^2(z)dz}{\int_0^{h_v}\rho\left(z\right)dz} \tag{5.6}$$

where $\sigma_r^2(z)$ is defined as

$$\sigma_r^2(z) = \sigma_g^2 + (\sigma_v^2 - \sigma_g^2)\frac{z - z_g}{h_r}. \tag{5.7}$$

Here, h_r is the reference height, which is an arbitrary constant value (Lavalle and Hensley, 2015), λ is the SAR system wavelength, and σ_g and σ_v are the surface and canopy layer motion standard deviations, respectively. The function $\rho(z)$ is the structure function, which defines the vertical structure of the vegetation layer. Similar to the RVoG model, the RMoG model assumes a Gaussian function to represent the structure of the trees. The procedure of solving (5.6) is explained in details in Lavalle and Hensley (2015).

Here, the primary assumption is that the maximum of the structure function occurs at the top of the canopy layer and the volume backscatter and from ground components are distinguishable. This assumption leads to biased height estimation especially in complex and multi-layer forests (Lavalle et al., 2012). To improve the accuracy of the RMoG model, and inspired by Cloude (2010), we have proposed the RMoG$_L$ model (Ghasemi et al., 2018b).

5.2.4.3 The RMoG$_L$ Model

The RMoG$_L$ model is similar to the RMoG model, but instead of an exponential function, it uses a finite Fourier–Legendre series as the structure function when considering the motion of scatterers along the vertical axis (Ghasemi et al., 2018b). Thus, the complex coherence of the RMoG$_L$ model γ_{M_L} equals

$$\gamma_{M_L} = e^{jk_v}\frac{\int_{-1}^{1} f(z')\exp(1+f(z'))\exp(jk_v z')\exp(\frac{-1}{2}(\frac{4\pi}{\lambda})^2\sigma'^2(z'))dz'}{\int_{-1}^{1}(1+f(z'))dz'}. \tag{5.8}$$

Here, $z' = \frac{2z}{h_v} - 1$, $k_v = \frac{k_z h_v}{2}$, and $\sigma'(z') = \sigma\left(\frac{h_v(1+z')}{2}\right)$ (Ghasemi et al., 2018b). The a_i are normalized Legendre coefficients, and the $f_i, i = 1, 2, ..., n$ are Fourier functions of different orders (Cloude, 2010) defined as

$$f_i(z') = \sum_{i=0}^{n} a_i P_i(z'), \tag{5.9}$$

where the $P_i(z')$, $i = 1, 2, ...$ are Legendre polynomials (Cloude, 2006). If we assume that $\sigma_g = 0$ according to the short time interval between image acquisition times, the final form of complex coherence obtained by the RMoG$_L$ model equals

$$\gamma = \frac{\gamma_{M_L}}{\mu + 1}. \tag{5.10}$$

The number of terms in $f_i(z')$ depends upon the vegetation layer; for more complex vegetation layers, several terms are needed, whereas a single layer can be modeled by fewer terms. Note that, for estimating more than two Legendre coefficients, we need multi-baseline SAR data. It is argued in Cloude (2010) that using the first and second terms of the series should be sufficient in most cases; the accuracy, however, depends upon the complexity of the vegetation layer. According to the relatively simple structure of the hemi-boreal forest and the availability of PolInSAR data, we fixed the number of terms to two. Therefore, parameters to be estimated are φ_g, h_v, a_1, a_2, and $\sigma'(z')$. The way of solving (5.10) is described in Ghasemi et al. (2018b). The solving method is similar to the RMoG model, but some extra steps should be taken in order to deal with more number of unknown parameters.

5.2.5 Biomass Estimation Using PolInSAR Data

The most important outcome of the RVoG, RMoG, and RMoG$_L$ models is a height map of the area. Averaged, plot-wise height values are then extracted from these height maps. In this study, we applied a buffer zone of 10 m to reduce the border effect.

We used a robust regression model to retrieve biomass from PolInSAR height. The used algorithm is non-linear least square fitting with LAR (Least Absolute Resiuals) algorithm for providing the prediction bounds within a 95% of confidence interval (Chen et al., 2012). According to past studies, there are different assumptions about the relation between biomass and PolInSAR height. The first and most common assumption is that the biomass can be obtained from PolInSAR height by a linear (Gizachew et al., 2016). In other studies, this relation has been shown to be non-linear (Askne and Santoro, 2012). Therefore, to find the best model for estimating biomass, we started by a polynomial model to relate biomass to PolInSAR height. The general form of this model is

$$\ln(B) = \sum_{i=1}^{n+1} \alpha_i H^{n+1-i} \tag{5.11}$$

where n is the polynomial degree, B is biomass, H is the PolInSAR height obtained from the RVoG, RMoG, and RMoG$_L$ models, and the α_i are coefficients to be estimated. The parameters B and H are standardized and thus are dimensionless. We determined the number of coefficients by trial and error, and the final form arrived at a value of $n = 3$. The polynomial model is

$$\ln(B) = \alpha_1 H^3 + \alpha_2 H^2 + \alpha_3 H + \alpha_4. \tag{5.12}$$

We stopped to increase n if $\alpha_i \leq 0.005$ and consequently $\alpha_i H^{n+1-i} \leq 0.15$ according to Solberg et al. (2017). As is evident from (5.12), the relation between biomass and PolInSAR is non-linear.

Another common assumption is that biomass increases proportionally to the increase of height. Therefore, as a further examination, the one-term and two-term exponential equations were tested. Furthermore, we tested whether the power series can describe the relation between two variables. The general form of the selected exponential model equals

$$\ln(B) = \beta_1 \left(1 - e^{-\beta_2 H}\right), \tag{5.13}$$

and for the power series it equals

$$\ln(B) = \zeta_1 H^{\zeta_2} \tag{5.14}$$

where the β_i and ζ_i, $i = 1, 2$ are the coefficients to be estimated.

The reliability of (5.12)- (5.14) is based upon the assumption that the observed height values have a normal distribution of errors. In our case, according to Askne and Santoro (2012); Ulander et al. (2011a), outliers occur in measured biomass values. Robust regression (Rousseeuw and Leroy, 2005) was therefore applied to avoid the effect of outliers on estimated parameters. It assigns a weight value to each data point with weights being adjusted iteratively. In the first iteration, one value, in our case 0.5, is assigned to all data points, and by using normal least squares the coefficients are estimated. In the next iterations, the weights are re-estimated to place less emphasis on the points at a larger distance from model predictions. Next, the model coefficients are recalculated using weighted least squares. This procedure proceeds until the difference between each estimated coefficient in two different iterations is below a thereshold, selected as 0.005 in this study (Askne and Santoro, 2012).

5.2.5.1 Data Splitting

The selection of a training and a test data set directly affects the reliability of estimated parameters. Different strategies exist for solving the so-called "*data splitting*" problem (Picard and Berk, 1990; Reitermanova, 2010). It is important to choose a good subset of data for training that preserves the generality of the model while having high accuracy. These two aspects, however, are conflicting. For determining the best training subset, we applied two procedures. First, we selected 75%, 50%, and 25% of the data points randomly as the training set and carried out the regression. Second, the field plots were divided into three groups based upon measured biomass value as low ($<$ 120 ton ha^{-1}), medium (120–240 ton ha^{-1}), and high ($>$ 240 ton ha^{-1}). Half of the data points from each category was then used as training data and the other half as test data. These two approaches, called the random and stratified methods, respectively, were compared and the best method was selected. The modeling procedure was repeated for mean diameter and basal area to understand how structural properties of trees are related to the height obtained from PolInSAR images.

5.2.6 Accuracy Assessment

To compare PolInSAR height with ground truth data, the first step is to convert the height maps from slant-range to ground-range. This was done using a precise DEM available in the campaign data and using the suggested method in Ulander et al. (2011b). We used both field and Lidar data as the

Table 5.1: Summary statistics of the biophysical parameters measured within plots with 10 m radius.

Parameters	Mean	Range
Biomass (ton ha^{-1})	120.04	1.2–315.96
Basal area (m^2 ha^{-1})	26.34	1.35–77.81
Mean diameter (m)	2.39	0.52–5.05
H100 (m)	28.24	13.77–34.77

reference height map. For evaluating the accuracy of three different height estimation models, the average height inside each plot was compared with the corresponding values on Lidar CHM and with the H100 value of each plot. Different metrics were used for evaluating the RVoG, RMoG, and RMoG$_L$ models. To test the distribution of measured and obtained biomass maps and for comparing them, the Kolmogorov–Smirnov (KS) test was applied. A one-sample KS test examined the null hypothesis that the data distribution is a hypothesized distribution against the alternative that it does not follow such distribution. The test statistic is the maximum absolute difference between the empirical Cumulative Distribution Function (CDF) calculated from the dataset $\hat{F}(x)$ and the hypothesized CDF of $G(x)$, in our case the normal distribution:

$$D = \max\left(\left|\hat{F}(x) - G(x)\right|\right). \tag{5.15}$$

A two-sample KS test checks if the two datasets have similar distributions. The alternative is that the two tested datasets have different distributions.

5.3 Results

A summary of the most important biophysical parameters measured within field plots is provided in Table 5.1 and a histogram in Figure 5.5. These values are reported for the whole dataset, whereas the regression analyses results are based on the selected training data as described in Section 5.2.5.1. According to Table 5.1, the measured biomass varies from 1.2 to 315.96 ton ha^{-1}. The mean value is 120 ton ha^{-1} and the median value is 105 ton ha^{-1}, showing that the distribution of the field data deviates from the normal distribution. Other measured biophysical parameters i.e., basal area and mean diameter also have a wide range of variation.

The histogram is skewed and shows several peaks. This makes it difficult to fit a specific distribution function to biomass values. Most plots have a biomass around 100–130 ton ha^{-1}, whereas the second peak occurs between 200 and 230 ton ha^{-1}. This multi-modal histogram validates our choice to divide the data into different categories and to select a training data set for each category. The relation between measured biomass and biomass predicted by Lidar is presented in Figure 5.6. The relative error is approximately equal to 12.7%. The plot shows a positive correlation between measured biomass

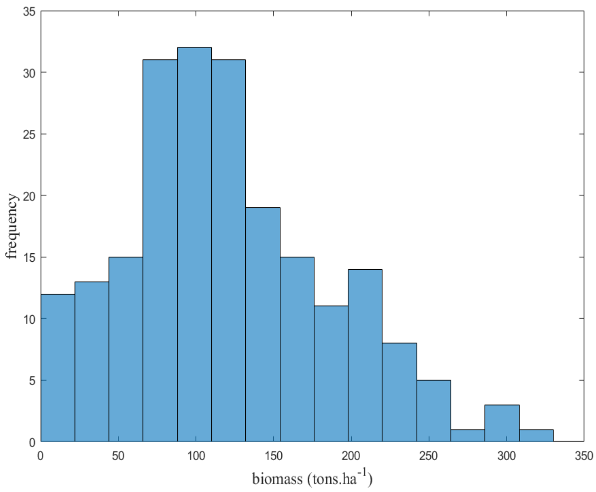

Figure 5.5: Distribution of forest plot biomass for the 214 plots at the test site.

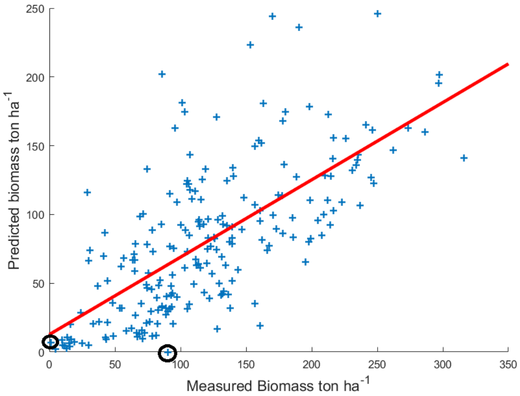

Figure 5.6: Relation between measured and predicted biomass using Lidar data with $R^2 = 0.60$ and RMSE=0.68 ton ha^{-1}. The points marked with dark circles are possibly the measurement errors.

and predicted biomass by Lidar height. Two points marked with circles are most likely measurement errors.

After processing SLC PolInSAR images and obtaining complex coherence (Cloude and Papathanassiou, 1998a), height maps using the RVoG, RMoG, and RMoG$_L$ models were obtained. The height map generated by the RMoG$_L$ model is shown in Figure 5.7. Figure 5.7 shows a good agreement with the Lidar CHM of Figure 5.4. For shorter trees, we see that the RMoG$_L$ model overestimates tree heights, while for taller trees the height is underestimated. Plot-wise averaged height values from three different models were compared

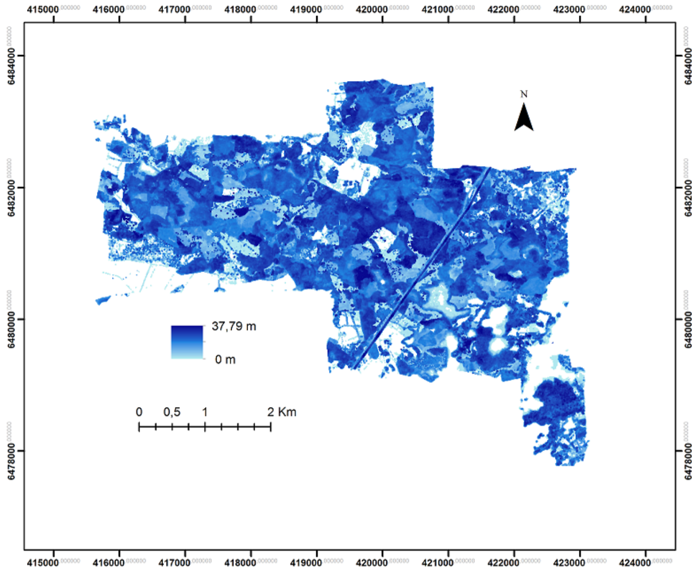

Figure 5.7: Resulting height map from the RMoG$_L$ model.

Table 5.2: Coefficients of the fitted polynomial model (within a 95% confidence interval).

α_1	α_2	α_3	α_4(Constant Term)	RMSE (ton ha^{-1})	Adjusted R^2	
RVoG	−0.028	−0.063	0.498	4.630	30.87	0.50
RMoG	−0.014	−0.083	0.498	3.660	30.80	0.62
RMoG$_L$	0.005	−0.102	0.467	2.694	30.75	0.73

to the corresponding H100 values. The results showed that $R^2 = 0.43$ for the RVoG model, $R^2 = 0.47$ for the RMoG model, and $R^2 = 0.48$ for the RMoG$_L$ mode. The weak correlation between PolInSAR height and H100 is because H100 is measured based on the tallest trees inside each field plot while the PolInSAR height represents the average of canopy height. Similarly, height maps obtained from the RVoG, RMoG, and RMoG$_L$ models were compared with Lidar CHM, and results are shown in Figure 5.8. The Lidar and PolInSAR heights show a positive correlation. In the case of the RMoG model, the noise has decreased and the data points are closer to the least square line. We also observe that the PolInSAR height estimation error increases with increasing tree heights. Next, we selected training and test sets for performing regression analyses. The stratified sampling leads to more accurate biomass estimation. All results hereafter have been obtained using stratified sampling. The relation between PolInSAR height and biomass was examined using different models. First, we fitted a polynomial model to relate the PolInSAR height and biomass. The results are listed in Table 5.2.

The highest R^2 and lowest RMSE values were obtained by the RMoG$_L$ model. Another important observation is that, if we set $H = 0$, then $B \neq 0$.

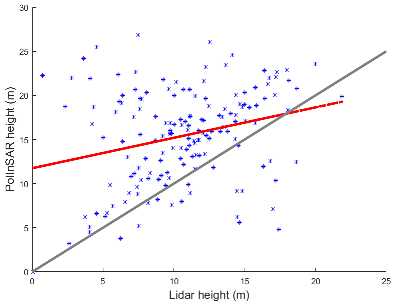

(a)

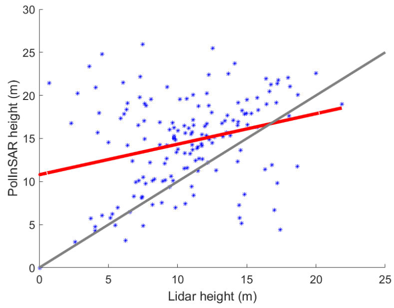

(b)

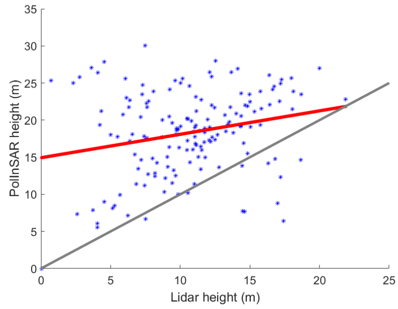

(c)

Figure 5.8: Relation (in red) between PolInSAR height resulting from: (a) the RVoG model ($R^2 = 0.50$, RMSE = 0.67 m), (b) the RMoG model ($R^2 = 0.69$, RMSE = 0.60 m), and (c) the RMoG$_L$ model ($R^2 = 0.78$, RMSE = 0.55 m) with the corresponding averaged height values from Lidar. The black line presents 1:1 line.

Table 5.3: Coefficients of the fitted exponential model (within 95% confidence interval).

	β_1	β_2	RMSE (ton ha^{-1})	Adjusted R^2
RVoG	5.15	0.13	30.87	0.54
RMoG	5.10	0.17	30.75	0.56
RMoG$_L$	5.10	0.18	30.61	0.61

The B value shows the error of the fitted polynomial model for estimating biomass from PolInSAR height. We can force a no-intercept regression to estimate biomass, but the RMSE value then becomes high (0.75 ton ha^{-1}). Next, we correlated height obtained by PolInSAR and biomass via an exponential model and a power series. The results of fitting the exponential model are listed in Table 5.3.

Similar to polynomial regression, the RMoG$_L$ model is the best model, with the lowest RMSE and highest R^2 value. Previous studies (Solberg et al., 2017) suggest using an exponential model to estimate biomass from height. We observed that the RMSE is higher than when using the polynomial

Table 5.4: Coefficients of the fitted power series (within 95% confidence interval).

	ζ_1	ζ_2	RMSE (ton ha^{-1})	Adjusted R^2
RVoG	2.068	0.277	40.01	0.56
RMoG	2.194	0.274	30.93	0.60
RMoG$_L$	2.224	0.276	30.87	0.65

Table 5.5: The slope and intercept of piece-wise linear regression for the RMoG$_L$ model.

Piece-Wise Regression	Slope	Intercept	Average RMSE (ton ha^{-1})	Adjusted R^2
H <8 m	1.73	0	30.91	0.90
8 m $\leq$ H	0.04	3.20	30.64	0.62

model, and R^2 is lower. In contrast with the third-degree polynomial, the exponential model passes through the origin, hence a zero biomass value for $H = 0$. In addition, the power series was tested to estimate biomass, and the results are presented in Table 5.4.

We obtain higher RMSE values by using power series in comparison with the polynomial and exponential models. According to the variation of the data set and to provide further comparison, the piece-wise regression was also tested. In finding the break points of the dataset, the target is to find y given the number of break points x, which minimizes the following function

$$p = |\mathrm{B} - \mathrm{interp}(H_b, B_b, H)|^2 . \tag{5.16}$$

Here, interp is the interpolation function, H_b is the break point, and B_b is the interpolation point for the H_b (Strikholm, 2006). The results of piece-wise linear regression relating biomass to the RMoG$_L$ height are listed in Table 5.5.

The piece-wise regression showed good results as compared to the power-series and polynomial models listed in Tables 5.2 and 5.3. For $H > 8$ m, the slope of the line decreases significantly, showing the saturation effect. For both exponential and piece-wise regression models, the saturation effect happens when biomass reaches approximately 300 ton ha^{-1}.

The polynomial, exponential, power series, and piece-wise linear regression curves for the RMoG$_L$ model are shown in Figure 5.9. We notice a saturation effect for $H > 8$ m in Figures 5.8b,d. Figure 5.8a does not show the saturation point clearly, which is in line with other studies(Solberg et al., 2017).

According to Tables 5.2–5.5 and Figure 5.8, the most accurate model is the exponential model, while the piece-wise regression also showed good results. Since it is more straightforward to fit a single curve to the whole dataset, we selected the exponential to produce the biomass map. For accuracy assessment, the remaining 52 plots out of 214 field plots were used as the test data set. Different metrics were employed for this purpose (Soja et al., 2013; Lu et al., 2016). These metrics included bias (μ), co-variance (σ),

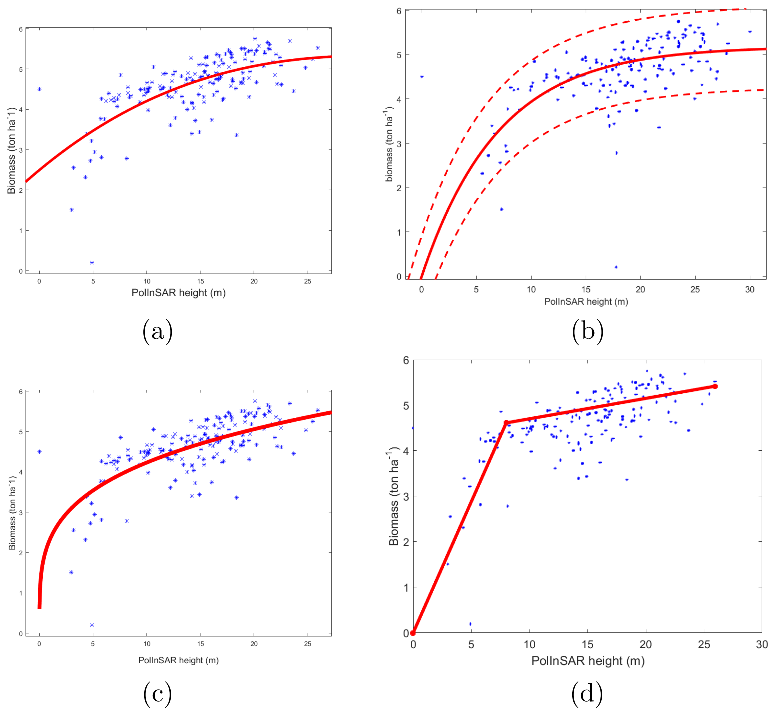

Figure 5.9: Relation between logarithm of measured biomass and RMoG$_L$ height resulting of: (a) polynomial ($R^2 = 0.42$), (b) exponential ($R^2 = 0.67$) with prediction bounds within a 95% confidence interval calculated by the LAR method (c) power series models ($R^2 = 0.54$), and (d) piece-wise linear model ($R^2 = 0.60$). The biomass values on vertical axis represent $\ln(B)$.

Table 5.6: Result of evaluating fitted exponential model using test datasets.

	μ(ton ha^{-1})	σ(ton ha^{-1})	RMSE (ton ha^{-1})	Adjusted R^2	Relative Error (%)
RVoG	36.81	0.72	62.06	0.45	46
RMoG	27.12	1.97	55.44	0.74	37
RMoG$_L$	15.97	2.09	46.65	0.82	30

root-mean-square-error (RMSE), and the coefficient of determination (R^2). The results are listed in Table 5.6.

Biomass values of the test dataset were compared to corresponding predicted biomass by the Lidar data, and the results are plotted in Figure 5.10.

Furthermore, the relation between PolInSAR height and mean diameter on the one hand and basal area on the other have been examined to gain insight into how these biophysical parameters affect height measurements. The results are shown in Figure 5.11. The results showed a significantly better performance of the RMoG$_L$ model on test data.

The results of applying two-dimensional KS-test between predicted bio-

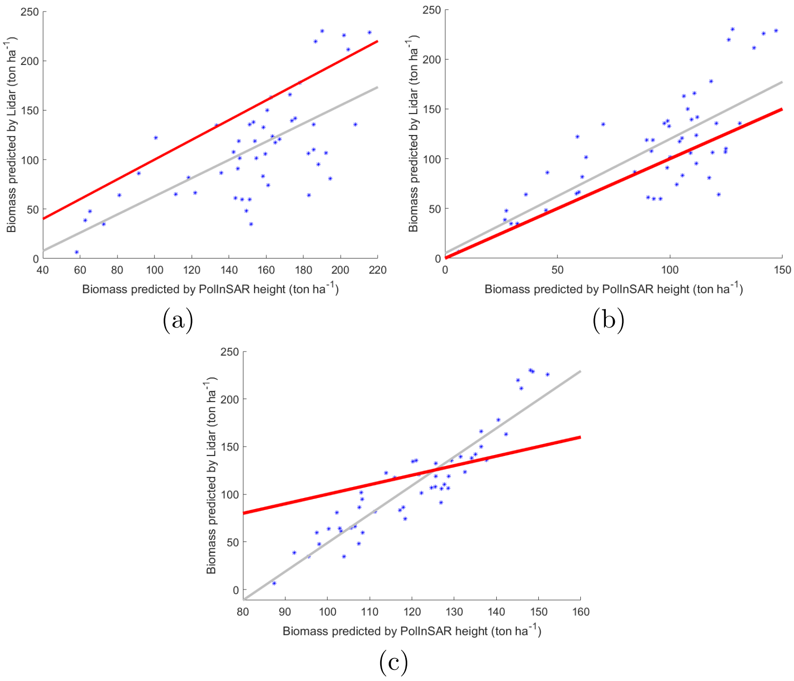

Figure 5.10: Relation between measured biomass by PolInSAR data and predicted biomass by Lidar data for the test dataset: (a) the RVoG model with $R^2 = 0.60$ and RMSE $= 30.85$ (ton ha^{-1}), (b) the RMoG model with $R^2 = 0.73$ and RMSE $= 30.73$ (ton ha^{-1}), and (c) the RMoG$_L$ model with $R^2 = 0.92$ and RMSE $= 30.64$ (ton ha^{-1}).

Table 5.7: Parameters of the two-dimensional KS test between biomass predicted by Lidar and PolInSAR.

	h	p	D
RVoG	0	0.001	0.41
RMoG	0	0.000	0.31
RMoG$_L$	0	0.000	0.21

mass by PolInSAR and Lidar data are listed in Table 5.7, whereas the biomass map resulting from the RMoG$_L$ model is shown in Figure 5.12. The results showed a positive linear relation between mean diameter, basal area, and PolInSAR height and the relation between mean diameter and basal area are stronger. This shows that inclusion of the mean diameter in obtaining biomass estimation models increases the accuracy of the biomass estimation.

The parameter h equals 0 if the null hypothesis of having similar CDFs is not rejected and equals 1 if the CDFs are not similar at the 0.05 significance level. The parameter D is the distance between two dataset distribution

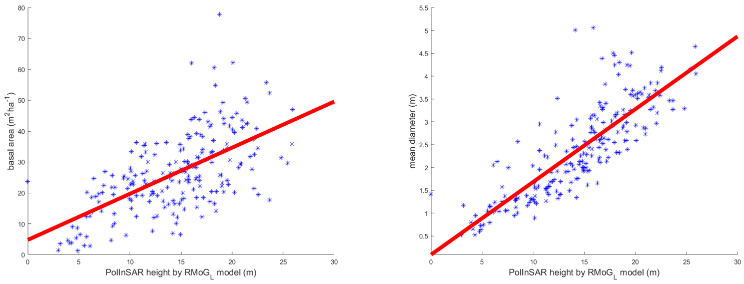

(**a**) (**b**)

Figure 5.11: The relationship: (a) between the PolInSAR height from the RMoG$_L$ model and the basal area with $R^2 = 0.61$, and (b) between this height and the mean diameter with $R^2 = 0.81$ in red.

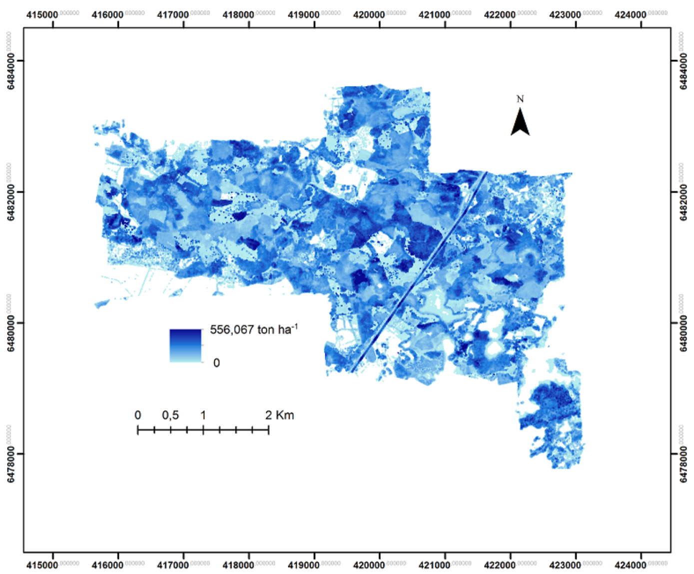

Figure 5.12: Resulting biomass map from the RMoG$_L$ model.

functions and shows the goodness of fit. From Table 5.7, we can see the D decreased by 50% by applying the RMoG$_L$ model.

To provide a better comparison, the predicted biomass by PolInSAR height was also compared to the measured biomass of the field plots. The results are shown in Figure 5.13.

The results shows a positive linear relation between PolInSAR predicted biomass and field biomass for all three height estimation models. Figure 5.13c shows better performance of the RMoG$_L$ model, while the other models show good correlation as well.

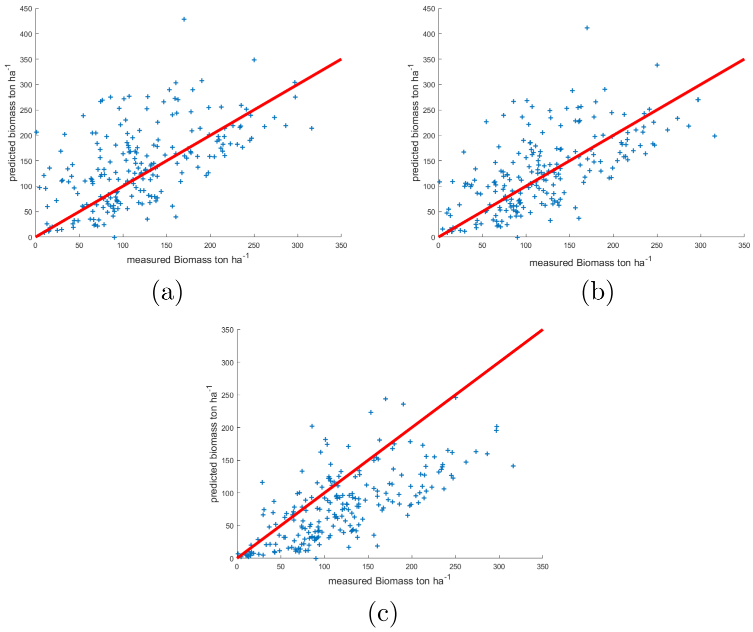

Figure 5.13: Relation between predicted biomass by PolInSAR data and measured biomass in field data: (a) the RVoG model with $R^2 = 0.55$ and RMSE = 30.97 (ton ha^{-1}), (b) the RMoG model with $R^2 = 0.69$ and RMSE = 30.76 (ton ha^{-1}), and (c) the RMoG$_L$ model with $R^2 = 0.74$ and RMSE = 30.69 (ton ha^{-1}). Red line is 1:1 line.

5.4 Discussion

In this chapter, we investigated whether correcting for temporal decorrelation improves biomass estimation accuracy. From the BioSAR2010 campaign, we selected plots with a 10 m radius, in line with other studies (Askne et al., 2013). Recorded values for these plots showed that biomass and other structural parameters had a broad range of varieties. This feature enabled us to examine how the PolInSAR height is related to different levels of biomass. Moreover, the effect of saturation was observed.

For evaluating three different height estimation models, the H100 and Lidar CHM were used as reference data. Neither Lidar nor PolInSAR height showed a significant correlation with the H100 parameter. The reason is that H100 represents the tallest trees, while the PolInSAR and Lidar height in each pixel represents the average of tree heights. In contrast, the Lidar and PolInSAR height values showed a strong relation. As we expected and as was shown previously, the relative error of height estimation decreased from 35% for the RVoG model to 18.6% for the RMoG$_L$ models.

Since there is no agreement in previous studies whether the correlation between biomass and tree height is linear or not, we examined different regression models. The outcome of the training sets should be a model that can predict the values for the test data set accurately and meanwhile is able to predict new data. If the model is over-trained, the accuracy will be good but the model would not be able to produce good results with new data. These two aspects, accuracy and generality, is known as the bias and variance dilemma (Picard and Berk, 1990). It becomes important when dealing with a high volume of data and when the developed model is being used in estimating biomass at the global scale. In this study, we tried two different strategies for data splitting to evaluate the effect of training set data selection on estimating biomass. The results showed a better performance of stratified sampling, but the computational time increased threefold. The best result is achieved by fitting an exponential model. The exponential curve and the piece-wise regression show a saturation effect for a biomass level above 300 ton ha^{-1}. The saturation level increases from 100 ton ha^{-1} when using SAR backscatter (Hansen et al., 2015) to 300 ton ha^{-1} by using PolInSAR height as the main predictor. In tropical forests, it is important to consider the saturation effect since biomass is mostly higher than 300 ton ha^{-1}.

The RMSE of biomass estimation decreased from 46% when using height resulting from the RVoG model to 30% for the RMoG_L model. As expected, there is a considerable improvement in estimating biomass after modeling temporal decorrelation. The results validated the hypothesis of the improvement of biomass estimation after correcting for temporal decorrelation.

Our results were compatible with previous studies for the same test site. For example, InSAR images at C-band were employed to estimate stem volume and achieved an RMSE value of 27% (Askne and Santoro, 2012). Similar studies using L and P-bands estimated biomass with RMSE values between 30–40% for L-band and between 20–30% for P-band (Soja et al., 2013; Sandberg et al., 2011). Interestingly, recent research in Remningstorp area using TanDEM-X interferometric heights showed an RMSE value around 16.5% (Askne et al., 2013). This improvement can be due to a larger number of baselines and a high number of field plots. Other studies in tropical, temperate, boreal, and hemi-boreal forests (Woodhouse et al., 2003; Papathanassiou and Cloude, 2003) showed an average error between 2 and 5 m with and average of 3.5 m in estimating tree heights using PolInSAR. This shows a PolInSAR height can be used to estimate biomass in different forest types.

The RMSE only, however, cannot be enough to show the model performance. Based on Table 5.6, the RVoG model has a significant bias, which, after correcting for temporal decorrelation, has decreased by about 50%. Moreover, the correlation increased from 0.45 for the RVoG model to 0.82 for the RMoG_L model. For the RMoG model, the results were close to the RMoG_L model. The difference is because of the more accurate structure function in the RMoG_L model.

The relation between the RMoG_L height and two other structural parameters, namely basal area and mean diameter, was also high. This is due to the capability of P-band in penetrating into the vegetation layer as well as the Fourier–Legendre series employed in the RMoG_L model to represent the structure of trees. This is an interesting finding since it shows the importance of taking different vegetation structures into account for estimating biomass.

Involving other biophysical parameters for example the D_{BH} in estimating biomass can have a huge effect on improving accuracy.

The result of the one-dimensional KS test showed a different distribution of measured biomass and predicted biomass by all height estimation models and Lidar data. The two-dimensional KS test showed similar distribution functions for predicted values by Lidar and PolInSAR data. The main reason is that, at the plot level, biomass is measured for individual trees, while remotely sensed data measure the canopy of trees that are spread around the tree trunk.

There is a requirement for methods that can estimate biomass at broader scales. The method and dataset we used here are limited because we used one pair of PolInSAR images. By using multi-baseline tomographic PolInSAR images, we can add more terms to the structure function of the RMoG_L model. Therefore, reconstruction of the tree structure has a higher resolution. We expect that this leads to more accurate biomass maps, but with an increased computation time.

There are other biophysical parameters of trees i.e., diameter and basal area that affect the SAR signal. The ideal case would be to develop a model based on height, diameter, and the basal area of the trees. In the case of using PolInSAR data, the only observable parameter is tree height. One possibility is to use the field data together with PolInSAR height, but in doing so the developed model would only be applicable to this area and we lose any generality. Thus, we chose to develop a model based on only PolInSAR height to maintain the general applicability of the model (Askne et al., 2013; Solberg et al., 2017).

Our findings showed a strong relation between PolInSAR height and above-ground biomass. The accuracy of biomass estimation improved considerably after correcting for temporal decorrelation. This means that the accuracy of height estimation is directly related to the biomass estimation accuracy. This shows the importance of mitigating temporal decorrelation in estimating height using PolInSAR since such mitigation affects the further products of height maps such as biomass. At present, the P-band images, on which we tested our proposed model, are only available in airborne sensors. Although they will also be available on spaceborne sensors in the near future, it would be of great value to examine the effect of the correction of temporal decorrelation on biomass estimation accuracy using other wavelengths, especially the L-band. As a sequel to this study, we suggest developing a unique structure function for each tree type according to the availability of the forest classification map. This will lead to more accurate biomass maps (Noble et al., 2000).

5.5 Conclusions

This study showed that, after mitigation of temporal decorrelation , the accuracy of biomass estimation improved by approximately 10%. Therefore, for producing biomass maps of a desirable accuracy, the temporal decorrelation factor should be considered. The best model selected for estimating biomass from PolInSAR was the exponential curve. Furthermore, we showed, in forests with diverse levels of biomass, that it is a good approach to divide the area according to the different height classes and use different regression lines for each class. By using PolInSAR height, the saturation level increases from 150 to 300 ton ha^{-1}. This is important in tropical forests where biomass is high and saturation becomes an issue.

A weak relation was observed between remotely sensed height maps and H100 values. This is due to the sensitivity of remote sensing sensors to the average height of the tree canopy versus the H100, which represents the tallest trees inside each plot. Basal area and mean diameter also affect the SAR signals, and consequently PolInSAR height estimates

The presented results demonstrate the capability of PolInSAR to obtain biomass maps. This is important since, in the near future, the satellite BIOMASS mission aims to produce biomass maps with wall-to-wall coverage of important forested areas.

6 Exploring the Sensitivity of Height Estimation Models to Adaptive Coherence Estimation

This chapter is based on the paper: Ghasemi, N., Tolpekin, V. and Stein, A. Exploring the effect of adaptive coherence estimation on tree height extraction from PolInSAR data. Submitted to 2019 Living Planet Symposium. 13-17 May 2019, Milan, Italy. Accepted as oral presentation.

Abstract

Complex coherence plays an important role in most application of PolInSAR. Most application estimate complex coherence using averaging in a neighborhood window, thus assuming stationarity. Recently, adaptive methods have been introduced to select the neighborhood that recognizes pixels with similar polarimetric or polarimetric interferometric properties. This study presents two methods to explore the effect of adaptive statistically homogeneous pixels (SHP) selection on PolInSAR height estimation. They obtain the complex coherence used by the RVoG and RMoG$_L$ models to obtain tree height maps. Data are from L-band tomostack of the La Lope national park in Gabon with an average tree height of 30 m. The Double-Similarity (DS) method, which takes into account both polarimetric and interferometric information, in combination with the RMoG$_L$ model had the most accurate height map with an RMSE of 2.50 m. The Fixed-Point (FP) method with the RMoG$_L$ model had an RMSE value of 3.70 m, the Double-Similarity (DS) method with the RVoG model had an RMSE of 6.70 m and the FP method with the RVoG model had an RMSE equal to 8.40 m. The two methods were compared with the Boxcar and Refined Lee methods as well. This comparison showed that the adaptive SHP selection methods improved height estimation accuracy by approximately 17%. The study concludes that adaptive methods for obtaining coherence improve the height estimation accuracy, irrespective of the choice for a height estimation model. They, however, require longer computations.

Keywords: Complex coherence estimation, Double-Similarity, Fixed-Point, PolInSAR, Tree height estimation, AfriSAR campaign.

6.1 Introduction

Mapping and monitoring forests have extensively studied in the past (Garestier et al., 2008; Hajnsek et al., 2016; Le Toan et al., 2011; Schlund et al., 2017). These two tasks play an important role in the understanding of the climate and our natural resources. Estimating tree height is important to obtain biomass as a measure for carbon estimation. To do so the upcoming space mission BIOMASS aims to map forests using Synthetic Aperture Radar (SAR) data using full polarimetric sensors at short time intervals (Le Toan et al., 2011). Thus Polarimetric Interferometric SAR (PolInSAR) data will be available worldwide to monitor and map forests. PolInSAR (Cloude and Papathanassiou, 1998a; Papathanassiou and Cloude, 2001; Treuhaft and Siqueira, 2000) deals with different scattering mechanisms in relation to their vertical locations. More precisely, the PolInSAR coherence is related to tree height and is often used together in physical models. Among the most successful physical models are the RVoG (Cloude and Papathanassiou, 2003), RMoG (Lavalle and Khun, 2014; Lavalle and Hensley, 2015), and the RMoG$_L$ models (Ghasemi et al., 2018b,a). All these models use complex coherence as the input and deliver tree heights as the output. Accurate and reliable estimation of complex coherence, thus, is crucial to generate height maps. Several studies have been dedicated to optimizing complex coherence estimation. Optimizing coherence based on identifying dominant scattering mechanisms for single and multi-baseline data first proposed in **?**Neumann et al. (2008). Another suggestion made by Colin et al. (2005, 2006); Lopez-Sanchez et al. (2007) assumes equal scattering mechanisms at both ends of the PolInSAR image pair baseline. Recent studies isolate the scattering mechanisms in both single and multi-baseline data (Garestier et al., 2008; Garestier and Le Toan, 2010; Tebaldini, 2009). Examining new methods for estimating complex coherence was extended to SAR tomography data as well (Ballester-Berman and Lopez-Sanchez, 2010; Cloude, 2007b; Tebaldini, 2010). Estimated complex coherence has also been employed to classify SAR data in addition to mapping tree heights (Lee et al., 2005; Jager et al., 2007). The common core of these studies is to select homogeneous pixels following an appropriate similarity criterion. Such a criterion makes use of either polarimetric (Vasile et al., 2010), interferometric (Jager et al., 2007), or both polarimetric and interferometric information (Conradsen et al., 2003; Chen et al., 2012). A PolInSAR pair s_1 and s_2 consists of two random matrices following the Complex Wishart distribution. The complex coherence γ of this pair equals

$$\gamma = \frac{E\{s_1 s_2^*\}}{\sqrt{E\{|s_1{}^2|\}E\{|s_2{}^2|\}}}, \tag{6.1}$$

where $E\{.\}$ is the expectation and * is the complex conjugate transpose. Assuming stationarity and ergodicity (6.1) can be estimated as

$$\hat{\gamma} = \frac{\langle s_1 s_2{}^* \rangle_Q}{\sqrt{\langle |s_1| \rangle \langle |s_2|^2 \rangle_Q}}. \tag{6.2}$$

Here, $\langle . \rangle$ is the averaging over a spatial ensemble denoted by Q and Q is the set of statistically homogeneous pixels (SHPs). be sufficiently large to ensure accurate estimation of gamma. Q can be estimated in various ways. A conventional way is the Boxcar method inside a pre-defined rectangular window. Recently, there is an increasing attention towards using the adaptive selection of SHPs. For example, Refined Lee (Lee et al., 2003a), wavelets (Lopez-Martinez et al., 2005), weighted averaging (Cho and Kim, 2007), adaptive Lee method (Lee et al., 1999), and extended version of it (Lee et al., 2003b) are among the most popular methods. To separate pixels with different scattering mechanisms polarimetric decomposition methods have been suggested as well (Lee et al., 2003a; Mullissa et al., 2017). A recent study proposed Fixed-point (FP) method that uses polarimetric scattering mechanism of pixels to select SHPs. Most of these methods like the FP, use only polarimetric information and ignore the interferometric phase. To address this issue, a new method based on the complex covariance matrix including both polarimetric and interferometric information, has been proposed by Chen et al. (2012). This method is called Double-Similarity (DS) and has been tested on the BioSAR2008 data from Northern Sweden and on simulated PolInSAR data. The effect of its use, however, has not been examined on producing PolInSAR forest height map.
The objective of this study is to assess the accuracy of height estimation when using adaptive SHP selection methods for obtaining complex coherence. Double-Similarity (Chen et al., 2012) and Fixed-Point (Vasile et al., 2010) have been applied in addition to Refined Lee and Boxcar methods. All methods were applied with varying window size. Estimated complex coherence serves as input for the RVoG (Cloude and Papathanassiou, 2003) and RMoG$_L$ (Ghasemi et al., 2018a) models. The accuracy of the obtained height maps acquired from the RVoG and RMoG$_L$ models is used as a criterion to evaluate the efficiency and reliability of the different complex coherence methods. The selected dataset for this study is L-band PolInSAR images acquired during the AfriSAR campaign at the La Lope national park in Gabon (Schlund et al., 2017).
Rest of the chapter is organized as follows. First, the used dataset and study area in addition to two complex coherence estimation methods are described. Second, the results are presented and then the discussion and conclusion sections are provided.

6.2 Materials and Methods

6.2.1 Study area and data set

AfriSAR campaign data that was sleceted for this study, was designed and conducted to support the future satellite missions BIOMASS, that focuses on forest monitoring and vegetation parameters estimation (Dubois-Fernandez et al., 2016). A subset of this campaign study area that was selected for this study is a tropical forest in Gabon. The central coordinates of the region are 0.5°W and 11.5°N and it has an area of 4910 km^2 (Dubois-Fernandez et al.,

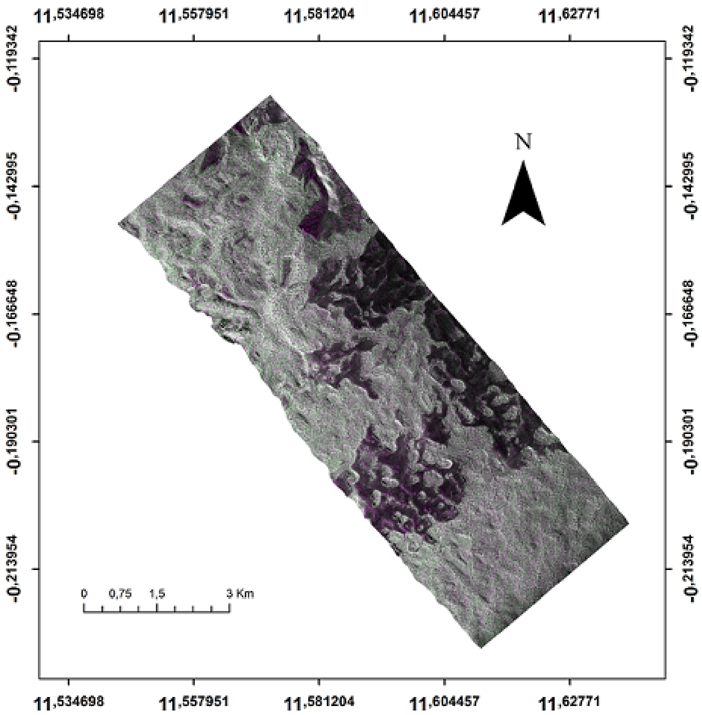

Figure 6.1: La Lope National park in Gabon studied during the AfriSAR campaign. The Pauli RGB is made of: red for HH, green for HV, and blue for VV channels.

2016). The Pauli RGB image of the full polarimetric L-band images acquired by UAVSAR sensor is shown in Figure 6.1. Selected L-band Single-Look-Complex (SLC) images have spatial baselines ranging from 20 m to 120 m with a 20 m interval. Temporal baselines vary from 22 minutes to 175 minutes. For the generation of the L-band tomostack, calibration and co-registration of the acquired images were performed using SRTM DEM and SAR orbital data following the process explained in Lavalle et al. (2016b); Dubois-Fernandez et al. (2016). Resulting tomostack has a spatial resolution of approximately 1.66 m in the range and 1 m in the azimuth directions, respectively. Pauli RGB and phase component of the HV channel interferogram of the master image are shown in Figure 6.2.

As Figure 6.2 shows, the area is covered by a mixture of forest and agriculture lands. The presence of speckle is noticeable and variation of topography is severe. These conditions provide us with the opportunity to examine the effect of adaptive complex coherence estimation over a heterogeneous and complicated forest. In addition to SLC images, Lidar data is available for the

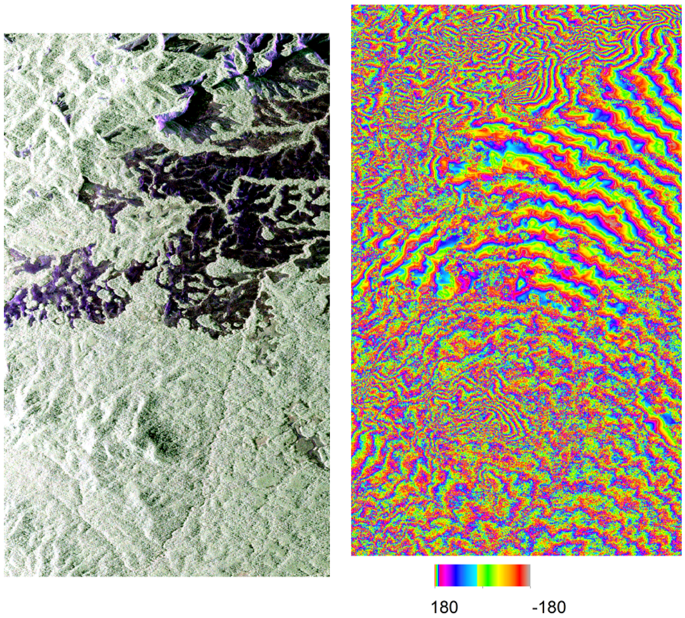

(a) (b)

Figure 6.2: L-band SLC stack of the La Lope national park (1000×600 pixels). (a) Pauli RGB of the master track ($HH - VV$: red, HV: green, and $HH + VV$: blue). (b) Phase component of the HV interferogram [°].

study area acquired by LVIS instrument from the Jet Propulsion Laboratory (JPL) of the National Aeronautics and Space Administration (NASA). The Lidar Canopy-Height-Map (CHM) is used as the ground truth for validation.

6.2.2 Adaptive estimation of complex coherence

As Figure 6.2 suggests, the area is covered mainly by forest and agriculture lands. The condition of the study area give us the opportunity to examine the effect of adaptive coherence estimation methods over a heterogeneous and complicated forest.

6.2.2.1 Boxcar and refined Lee

The boxcar method is based on incoherent averaging of the pixels within a pre-defined rectangular Q. This is the most simple method for defining Q (Lee et al., 2003b). Refined Lee method uses the minimum mean square error (MMSE) to perform the averaging. To do so, a linear model is used for de-spckling and the coefficients are defined based on the SHPs within the Q (Lee, 1986). Boxcar and Refined Lee methods have been compared with the FP and DS methods that are explained hereafter.

6.2.2.2 Fixed-point estimator of the complex coherence

For a mono-static SAR system, the target vector in the Pauli basis equals (Cloude, 2007a)

$$\mathbf{K} = [k_1, k_2, k_3]. \tag{6.3}$$

For vector $\mathbf{K}$, the Probability Density Function (PDF) function is obtained by

$$\mathrm{P}(\mathbf{K}) = \frac{\exp(-\mathbf{K}^{*}\mathrm{T}^{-1}\mathbf{K})}{\pi^{d}\det \mathrm{T}}, \tag{6.4}$$

where, $\mathrm{T} = \mathrm{E}\{\mathbf{K}\mathbf{K}^{*}\}$ is the PolInSAR coherency matrix, and $d = 3$ for a full polarimetric image. The Maximum Likelihood (ML) estimator of the coherency matrix equals (Chen et al., 2012)

$$\hat{\mathrm{T}} = \frac{1}{n}\sum_{q\in Q}^{n} \mathbf{K}_q {\mathbf{K}_q}^{*}, \tag{6.5}$$

where n is the number of samples. Following Yao et al. (2011), $\mathbf{K}_q$ can be estimated as

$$\mathbf{K}_q = \sqrt{\tau}\mathbf{z}_q, \tag{6.6}$$

where $\mathbf{z}$ is the speckle vector with zero mean, and τ is called "texture descriptor", which is a positive unknown variable defining the randomness of spatial variation in neighboring pixels. Covariance matrix of τ is defined as $\mathrm{M} = \mathrm{E}\{\mathbf{z}\mathbf{z}^{*}\}$ and represents the polarimetric information change (Rangaswamy et al., 1995).
The ML estimator of M under the assumption of identical independently distributed pixels within a neighborhood and $d = 3$ equals

$$\hat{M} = \frac{\prod_{q=1}^{n} \frac{1}{{\tau_q}^{3}} \exp\left(\frac{{\mathbf{K}_q}^{*} M^{-1}\mathbf{K}_q}{\tau_q}\right)}{\pi^{3q}\det\left(M\right)^{3}}. \tag{6.7}$$

Given M, the ML estimation of the τ equals

$$\hat{\tau_q} = \frac{{\mathbf{K}_q}^{*} M^{-1}\mathbf{K}_q}{3}. \tag{6.8}$$

For estimating M 6.9 is used (Vasile et al., 2010)

$$\hat{M}_{FP} = f(\hat{M}_{FP}) = \frac{3}{n}\sum_{q=1}^{n} \frac{\mathbf{z}_q {\mathbf{z}_q}^{*}}{{\mathbf{z}_q}^{*} M_{FP}^{-1}\mathbf{z}_q}. \tag{6.9}$$

M is estimated itratively and the initial value is the identity matrix. The condition to stop the iteration is (Pascal et al., 2008a)

$$D = \frac{||M_{q+1} - M_q||_F}{||M_q||_F} \leq \varepsilon. \tag{6.10}$$

Here, $||.||_F$ is Frobenius norm and ε is a predefined threshold (Pascal et al., 2008a). In Pascal et al. (2008b,a) it has been shown that 6.9 is independent from textural variability of the local window i.e. it is independent from τ and contains polarimetric information only.
For estimating the normalized coherency matrix over the selected SHPs, the following equation is applied

$$\hat{M}_q = \frac{3\hat{\mathrm{T}}}{\mathrm{Tr}(\hat{\mathrm{T}})}, \tag{6.11}$$

with

$$\hat{\mathrm{T}} = \frac{\sum_{q\in Q} \mathbf{K}_q \mathbf{K}_q^*}{\mathrm{card}(Q)}. \tag{6.12}$$

Here, card(Q) is the cardinality of Q. Combining 6.7 to 6.10, normalized estimator of the coherency matrix over Q equals

$$\hat{M}_l = \frac{3}{\mathrm{card}(Q)} \times \sum_{q\in Q} \frac{\mathbf{K}_q \mathbf{K}_q^*}{\mathbf{K}_q^* \hat{M}_{l-1} \mathbf{K}_q}, \tag{6.13}$$

where $l = 1, 2, ...$ and $\hat{M}_0 = I_3$. The final step is to obtain span image of the neighborhood and multiply it by the $\hat{M}$ estimated from 6.13 (Vasile et al., 2010).

6.2.2.3 Double-similarity method

Since the complex coherence obtained by 6.13 contains only polarimetric information, DS method has been proposed to include the interferometric phase as well as the magnitude. Following Chen et al. (2012), for two fully polarimetric images s_1 and s_2 with target vectors $\mathbf{K}_1$ and $\mathbf{K}_2$, the 6×6 complex covariance matrix equals

$$\mathrm{C}_6 = \left\langle \begin{bmatrix} \mathbf{K}_1 \\ \mathbf{K}_2 \end{bmatrix} \begin{bmatrix} \mathbf{K}_1^* & \mathbf{K}_2^* \end{bmatrix} \right\rangle = \begin{bmatrix} \mathrm{C}_{11} & \Omega_{12} \\ \Omega_{12}^* & \mathrm{C}_{22} \end{bmatrix}. \tag{6.14}$$

Here, C_{11} and C_{22} are 3×3 Hermitian covariance matrices for image s_1 and s_2 respectively. The Ω_{12} matrix contains the polarimetric interferometric phase correlation between two different channels and is not Hermitian. Following Chen et al. (2012), the PolInSAR covariance matrix can be presented as

$$\mathrm{C}_6 = \begin{bmatrix} \mathrm{C}_{11} & 0 \\ 0 & \mathrm{C}_{22} \end{bmatrix} + \begin{bmatrix} 0 & \Omega_{12} \\ \Omega_{12}^* & 0 \end{bmatrix} = \mathrm{C}_{pol} + \mathrm{C}_{int}. \tag{6.15}$$

Here, C_{pol} has only polarimetric information and thus is sensitive to speckle and scattering mechanisms variation whereas C_{int} contains both polarimetric and phase information.
To apply DS method for each candidate neighbor pixel (x_p, y_q), two indicators are proposed. The first is R_{PolIn}, defined as

$$\ln R_{PolIn} = L(2d\ln 2 + \ln(\det(\mathrm{X})) + \ln(\det(\mathrm{Y})) - 2\ln(\det(\mathrm{X})) + \det(\mathrm{Y})),$$

$$ \tag{6.16} $$

where X is the initial Q and Y is the initial Q when a potential candidate pixel for the SHP is added. The null hypothesis and alternative hypothesis are $H_0 : \mathrm{C}_x = \mathrm{C}_y$ $H_1 : \mathrm{C}_x \neq \mathrm{C}_y$ respectively. It has been shown in Chen et al. (2012) that if $\ln R_{PolIn} = 0$ then X = Y and for $\ln R_{PolIn} < 0$ for X $\neq$ Y. The second indicator is R_{pol} that only includes polarimetric information and defined as

$$\ln R_{Pol} = L(2d \ln 2 + \ln(\det(\mathrm{X}_{pol})) + \ln(\det(\mathrm{Y}_{pol})) - 2\ln(\det(\mathrm{X}_{pol} + \mathrm{Y}_{pol}))). \tag{6.17}$$

Here, $\mathrm{X}_{pol} = \begin{bmatrix} \mathrm{X}_1 & 0 \\ 0 & \mathrm{X}_2 \end{bmatrix}$ and $\mathrm{Y}_{pol} = \begin{bmatrix} \mathrm{Y}_1 & 0 \\ 0 & \mathrm{Y}_2 \end{bmatrix}$, and both follow a Wishart complex distribution. If $R_{polIn} > \varepsilon$ and $R_{pol} > \varepsilon$, then the pixel (x_p, y_p) is accepted as similar pixel where ε equals

$$\varepsilon = \sqrt{\frac{dD}{L}}. \tag{6.18}$$

For PolInSAR where $d = 6$ and for PolSAR $d = 2\sqrt{3}$, D is the minimum number of required SHPs, and L is the number of looks (Pascal et al., 2008a). Ultimately, the ML estimator of the covariance matrix of pixel (x_p, y_p), is

$$\hat{C}_{(x_p,y_p)} = \frac{1}{D} \sum_{l=1}^{D} \mathrm{C}_{6l}. \tag{6.19}$$

Here, C_{6l} is the original 6×6 covariance matrix. After repeating this procedure for all pixels the PolInSAR complex coherence is obtained (Cloude and Papathanassiou, 1998b).

6.2.3 Height estimation using adaptive complex coherence estimators

Complex coherence obtained with the four selected methods is used as the input for height estimation models i.e. the RVoG and RMoG$_L$ models. The output of the two models is compared with the Lidar CHM. The best method is then selected based on the accuracy of the estimated height. A summary of the procedure is presented in Figure 6.3.

6.3 Results

6.3.1 Complex coherence estimation

For performing the analyses a subset of the image was selected. The top left corner of Figure 6.2 was chosen to include both topographic variation and different types of vegetation cover i.e. forest and agriculture land. The complex coherence estimation methods were applied by varying the window size from 9×9, 11×11, and 15×15 pixels. Results of choosing an 11×11

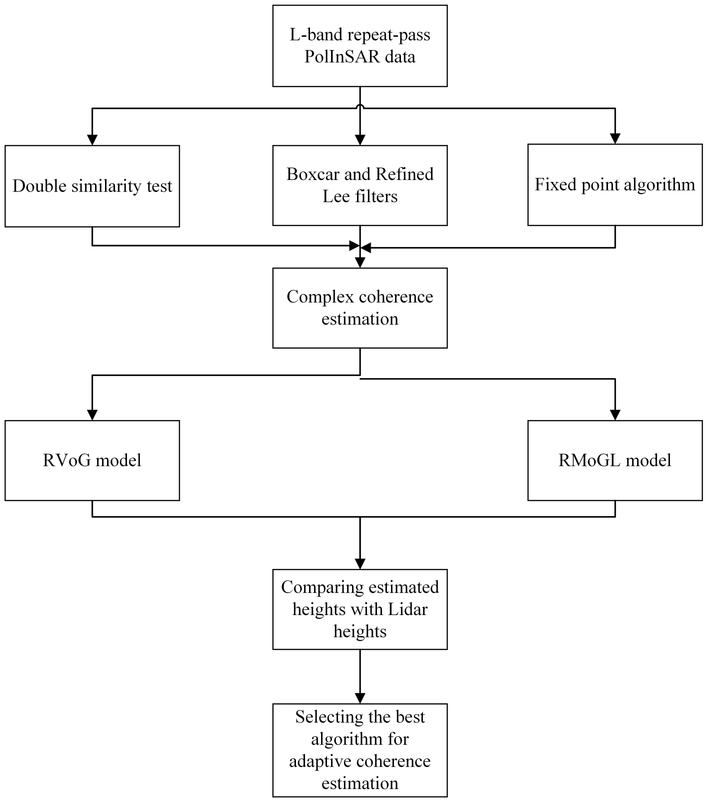

Figure 6.3: Flowchart of the methodology for selecting the best adaptive coherence estimation method.

window are shown in Figure 6.4. For the visual comparison of different adaptive methods, the area marked by a red square in Figure 5 is enlarged in Figure 6.5. According to Figure 6.5, the best method is DS (Figure 6.5(b)) as it achieves the most speckle reduction and detail preserving i.e. lines shown on Figure 6.5. The worst quality can be observed by applying Boxcar method (Figure 6.5(c)). The FP method (Figure 6.5(d)) has performed well on preserving the lines but has not reduced the speckle as compared to other methods. Refined Lee (Figure 6.5(a)) had an average performance on reducing speckle and improving visual quality. For providing a quantitative comparison signal-to-clutter (SCR)(Kim and Lee, 2012) ratio values for the displayed subset in Figure 6.5 is listed in Table 6.1. Table 6.1 shows the highest SCR belongs to the DS method applied on VV channel as also confirmed by Figure 6.5. The FP method produced high SCR values as well. Refined Lee and Boxcar methods had the lowest SCR values. For the subset displayed in Figure 6.4, mean and standard deviation values were obtained and are reported in Table 6.2. Values provided in Table 6.2 show how much speckle has been reduced after applying different methods. The best performance i.e. lowest std comes from DS and FP methods. For

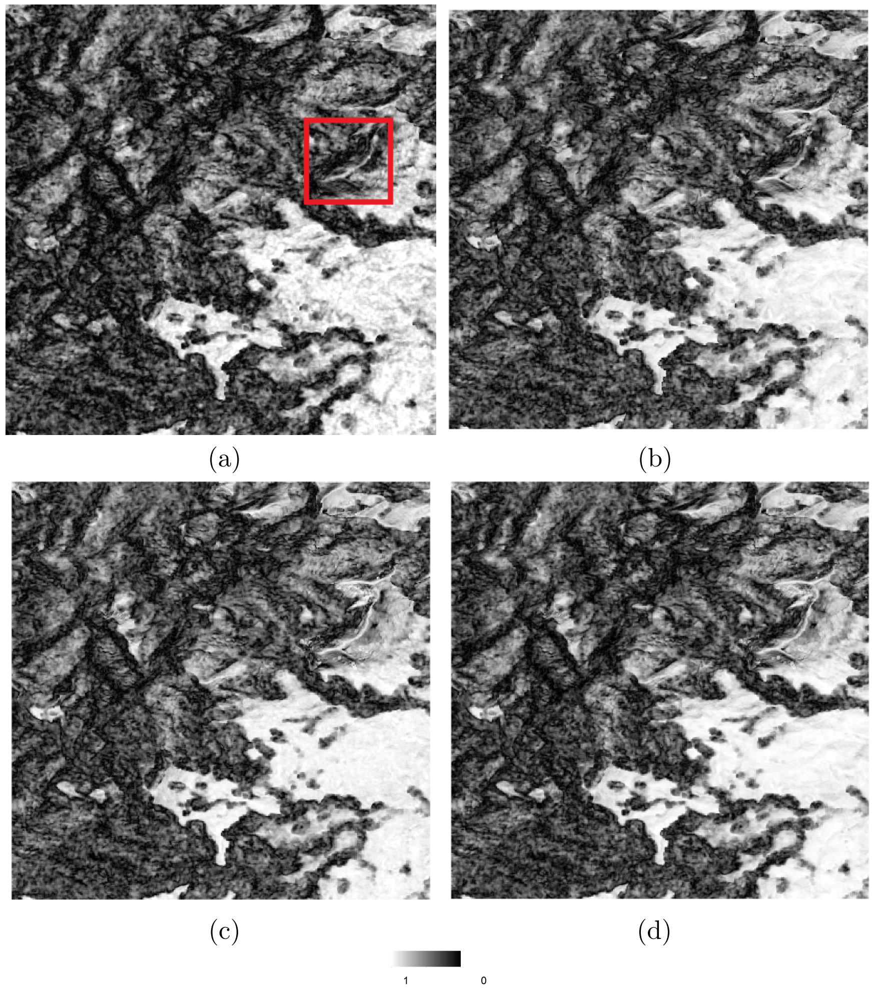

Figure 6.4: Results of adaptive methods on a 400×400 subset located at the top left corner of Figure 6.2. (a) Refined Lee, (b) DS method, (c) Boxcar, and (d) FP method. The window size for all methods is 11 × 11. The red rectangle is a 85 × 85 subset shown in Figure 6.5.

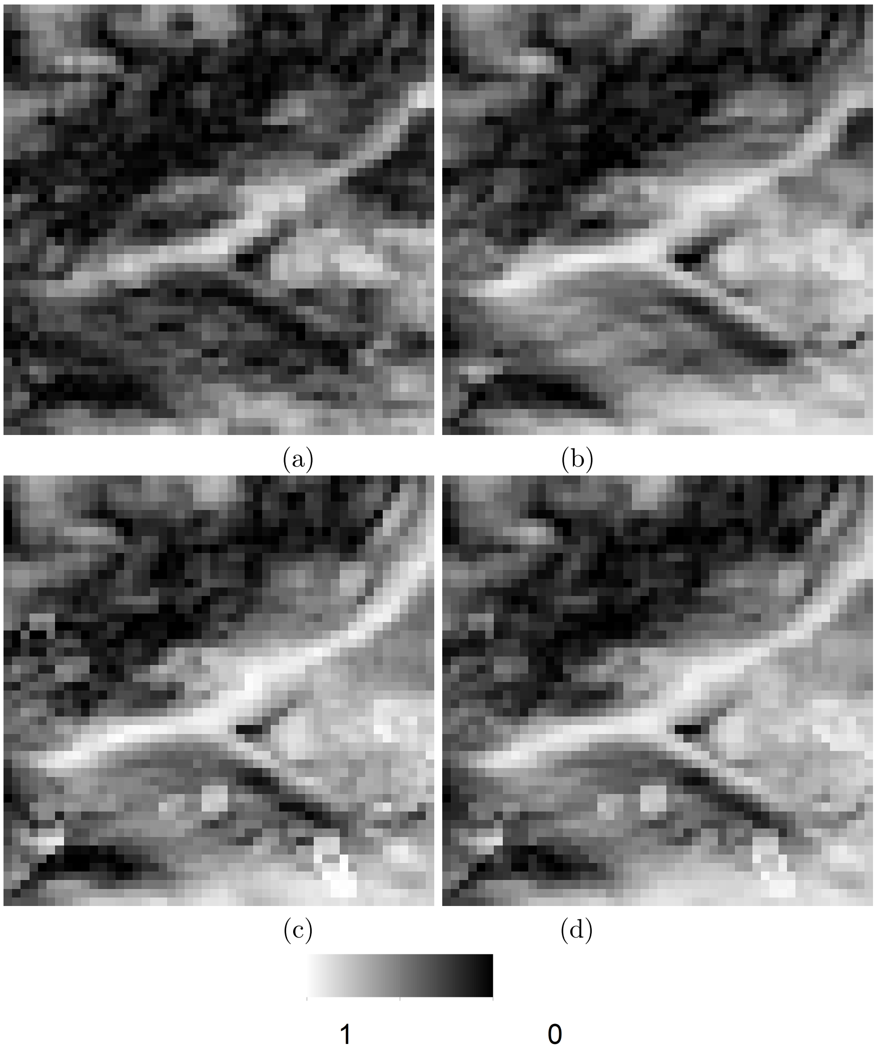

Figure 6.5: Enlarged magnitude image of the red rectangle shown in Figure 6.4 (85 × 85 pixels) by applying (a) Refined Lee, (b) DS, (c) Boxcar, and (d) FP methods.

Table 6.1: Signal-to-Clutter-Ratio for the selected area on Figure 6.5 for different polarimetric channels. Values are in Decibel (dB).

	HH	HV	VV
Boxcar	8.3	5.2	12.7
Refined Lee	15.7	6.3	18.3
FP	17.08	8.5	21.01
DS	20.55	10.7	23.05

Table 6.2: Mean and standard deviation (std) of coherence magnitude of the selected subset on Figure 6.4 for HH, HV, and VV channels using 11×11 window.

	Mean			Std		
	HH	HV	VV	HH	HV	VV
Boxcar	0.95	0.83	0.85	0.04	0.04	0.05
Refined Lee	0.90	0.83	0.86	0.04	0.05	0.05
FP	0.88	0.82	0.84	0.38	0.03	0.04
DS	0.86	0.79	0.80	0.05	0.03	0.03

Table 6.3: Mean and standard deviation (std) of the coherence magnitude using 9×9 and 11×11 windows on HH, HV and VV.

	Mean			Std			Mean			Std		
	HH	HV	VV	HH	HV	VV	HH	HV	VV	HH	HV	VV
	9 ×9 window						15 ×15 window					
Boxcar	0.90	0.89	0.82	0.06	0.04	0.06	0.95	0.87	0.88	0.05	0.04	0.06
Refined Lee	0.87	0.87	0.81	0.05	0.05	0.05	0.90	0.85	0.85	0.05	0.04	0.05
FP	0.85	0.85	0.80	0.05	0.05	0.05	0.90	0.85	0.85	0.04	0.03	0.05
DS	0.83	0.80	0.80	0.04	0.03	0.04	0.85	0.82	0.80	0.04	0.03	0.04

assessing the effect of local window size we applied all the four methods using 9 × 9, and 15 × 15 pixel windows as well as 11×11. The result is summarized in Table 6.3. A similar trend to Table 6.2 can be observed from Table 6.3. Better results were obtained with 15×15 window size, however, due to losing details using big window size is not advised. Thus all the results hereafter are produced with an 11×11 pixel window. For visualizing the difference between Boxcar, Refined Lee, and DS, the phase component of the original HV channel complex coherence, is shown in Figure 6.6. As Figure 6.6 suggests, DS method has the smoothest interferogram while preserving the fringes. Refined Lee method reduced speckle to a good extent but linear details have been lost. Boxcar reduces speckle, however, blurring effect also occurred.

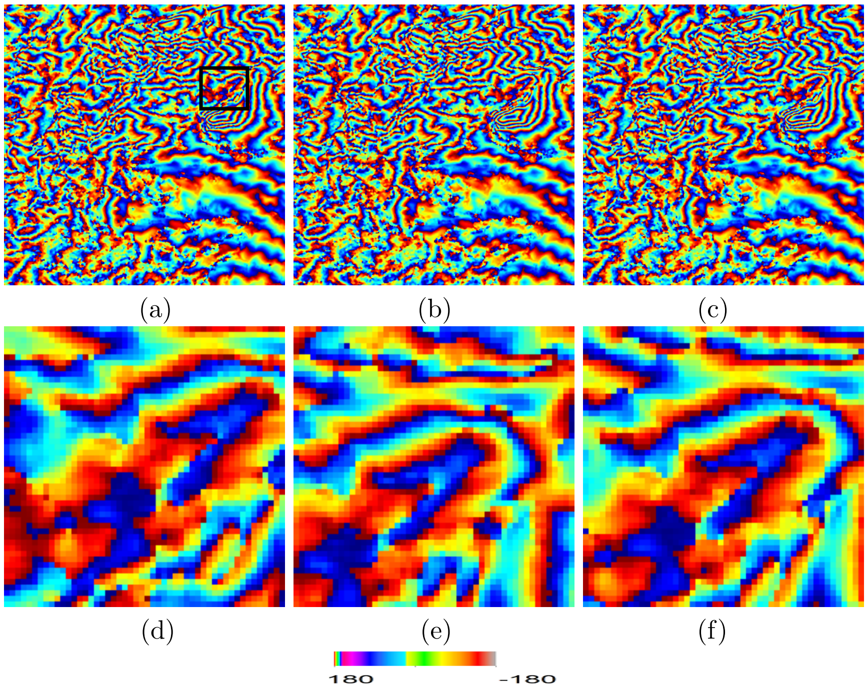

Figure 6.6: A subset (400×400 pixels) of the HV coherence phase component by applying :(a) Refined Lee, (b) DS, and (c) Boxcar methods. Images (d)–(e) are 85×85-pixel enlarged images of the shown area on part (a).

6.3.2 Height estimation and validation

Complex coherence was obtained with the four methods described in Section 2 and used as input for the RVoG and RMoG$_L$ models. Resulting tree height maps and Lidar CHM are presented in Figure 6.7. The better performance of DS method for the RVoG and RMoG$_L$ models is clearly visible in Figure 6.7. Overall, RMoG$_L$ model had more accurate results, however, the RVoG model accuracy also improved by employing DS method. For evaluating how adaptive complex coherence estimation methods contribute to the final produced height maps, the RMSE and R^2 values between acquired results and Lidar CHM were obtained. Additionally, the histograms and density functions of the height maps and Lidar CHM are provided. Histograms of the height maps vs. Lidar data presented in Figure 6.8. We can see the heights of trees are underestimated by using FP method whereas by using DS method, the height estimation improved considerably. The RMoG$_L$ model performs better independent from the choice of the coherence estimation method. Using DS method improved results for shorter trees specifically in both RVoG and RMoG$_L$ results. For taller trees, however, a bias can be observed with a slightly better performance of the DS method. In Table 6.4, the RMSE and Relative error values of the tested methods have been presented. They confirm a better performance of the both RVoG and RMoG$_L$ models by using DS.

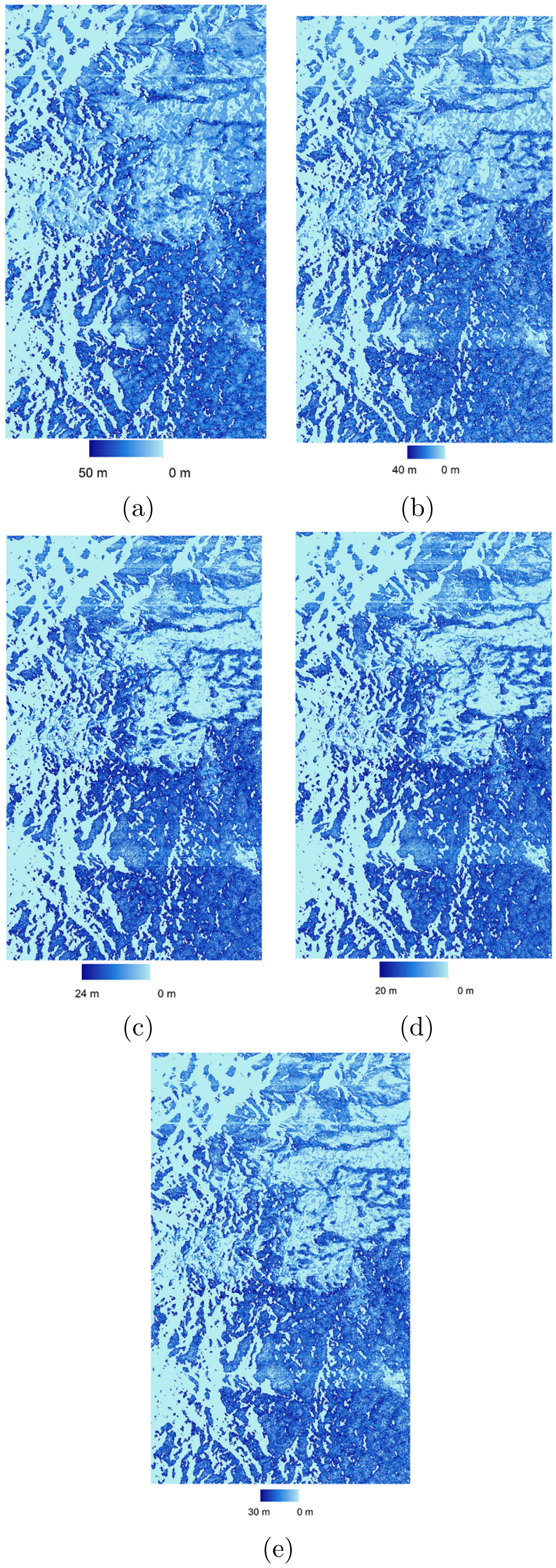

Figure 6.7: Height map of La Lope national park by: (a) RVoG model by applying FP, and (b) RVoG model by applying DS, (c) RMoG$_L$ model by applying FP, (d) RMoG$_L$ model by applying DS, and (e) Lidar CHM.

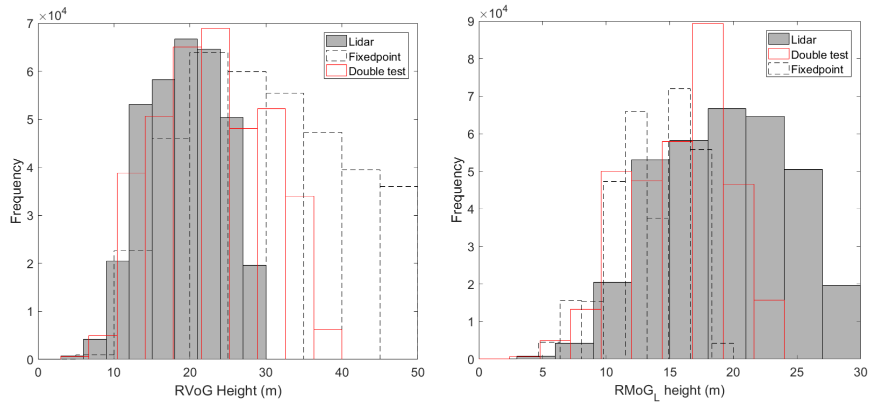

(a) (b)

Figure 6.8: Histograms of: (a) RVoG model by applying FP and by applying DS, (b) RMoG$_L$ model by applying FP and DS vs. Lidar CHM.

Table 6.4: The RMSE and relative error of different adaptive complex coherence estimation methods in comparison to Lidar height.

	FP method		DS method	
	RMSE (m)	Relative error (%)	RMSE (m)	Relative error (%)
RVoG model	8.40	36.40	6.70	31.00
RMoG$_L$ model	3.70	17.30	2.50	14.40

Table 6.5: R^2 values between PolInSAR height resulting from different adaptive methods and Lidar height.

	FP method	DS method
	R^2	R^2
RVoG model	0.55	0.58
RMoG$_L$ model	0.65	0.70

The best result is obtained with the RMoG$_L$ model when using DS method. Figure 6.9 shows the scatter plots of the displayed subset on Figure 6.5 used as another tool for comparison. Correlation coefficients obtained from these plots are listed in Table 6.5. These values show the improvement of height estimation accuracy by using DS method because of taking into account phase as well as polarimetric information. Table 6.6 compares the computational times of each method. As it shows, the computational time of the RMoG$_L$ model using DS method is three times longer than using similar set up with RVoG model. Refined Lee and Boxcar methods are close in computation time whereas FP has a moderate time. We should notice that using the RMoG$_L$ model is computationally heavy (Ghasemi et al., 2018b) and combining it

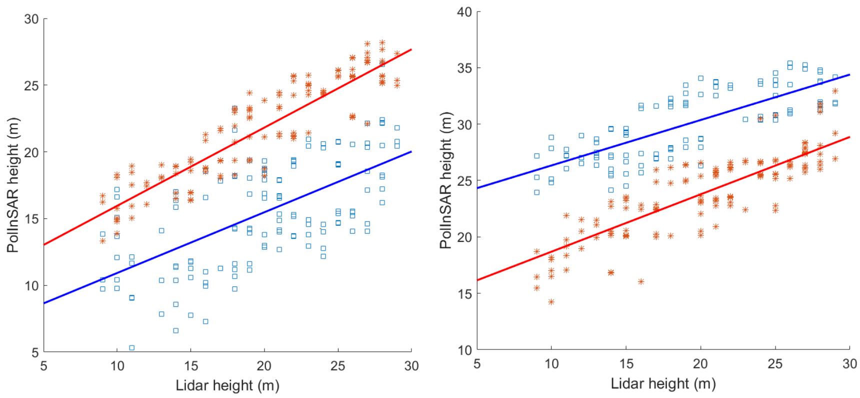

Figure 6.9: Scatter plots of: (a) RVoG model using FP method (□) and DS (∗), (b) RMoG$_L$ model using FP method (□) and DS (∗) vs. Lidar CHM. Displayed lines are least square ones.

Table 6.6: Computation time (minutes) of different methods in combination with the RVoG and RMoG$_L$ models for 400×400 pixels.

	DS	FP	Refined Lee	Boxcar
RVoG model	60	45	20	15
RMoG$_L$ model	180	120	60	45

with an adaptive coherence estimation increase computational task.

6.4 Discussion

Estimation of complex coherence by PolInSAR dependens upon selecting SHPs. Several studies have been dedicated to different methods for SHP selection (Vasile et al., 2010, 2006; Touzi et al., 1999). These methods commonly use polarimetric and texture information of the image. PolInSAR, though, consists of both interferometric and polarimetric data. As shown in the results, using only polarimetric features does not assure they have the same phase information and vice versa. Thus employing only one source of information may cause non-homogeneous pixels to be selected as SHPs.

To solve this problem, the DS method has been chosen and the results are compared to Refined Lee and Boxcar, and the FP method. A clear improvement was observed using FP and DS methods as compared to Refined Lee and Boxcar methods. Moreover, DS method increased the results of SCR value (Table 6.1) as well as the quality of images. This proves importance of using phase information in selecting homogeneous neighborhood.

For examining the effect of window size on estimating coherence, 9×9, 11×11, and 15×15 windows have been tested. In general, a larger window size allows to reduce speckle but leads to the loss of details. Boxcar treats all pixels inside the window equally and thus the blurring effect is visible in Figure 6.4(c) and Figure 6.5(c). The Refined Lee method obtains pixels weights and has better results compared to Boxcar method. The homogeneous pixels may not exactly fall into a pre-defined rectangular neighborhood. Since FP and DS examine homogeneous pixels based on different strategies, using larger window size i.e. 15×15 and 17×17 is also possible. Table 6.3 showed larger window size leads to better results i.e. lower standard deviation values. Using 15×15 windows, however, blurred out linear details. Thus, we had to choose between good performance and preserving details. When selecting 7×7 or 9×9 windows, most of the details are preserved but the probability of finding homogeneous pixels inside a small neighborhood is low. Therefore, we decided to apply a medium size i.e. 11×11 being a trade-off between performance and preserving details. For the selected subset shown in Figure 6.6, the number of similar pixels varied between 10 and 65. Differences between methods are then visible on interferograms.

Using DS method improved tree height estimation accuracy in both RVoG and RMoG$_L$ models. The effect on the RVoG model result is considerable while it does not affect the RMoG$_L$ model accuracy as much. The reason is using different structure function in the RMoG$_L$ model which has the flexibility to match with multi-layer vertical structure. This also shows the RMoG$_L$ model is more resistant to speckle. In addition, according to Figure 6.9, the scatter plot for the RVoG model shows better performance of the DS method on both RVoG and RMoG$_L$ results. These observations showed stability and higher SCR values in addition to lower standard deviation for the DS method.

The computation time of the DS and FP methods are approximately three times longer than those of the Boxcar and Refined Lee methods. Moreover, selecting a suitable method for coherence estimation is dependent on the application. Thus in the case of a big dataset and fast data browsing selecting Refined Lee and Boxcar may still be a suitable choice. For detailed analysis and in the case of sensitive data, more precise methods for coherence estimation leads to more accurate height estimation at the cost of longer computations. Thus one specific method is preferable to others in some cases whereas other methods are preferred otherwise. A selection is best based on the dataset, application and available computational resources.

6.5 Conclusions

Different methods for PolInSAR complex coherence estimations have been applied and the results were compared using several criteria. The results showed better performance of the adaptive methods for choosing homogeneous pixels inside a sliding window. Among all applied methods, FP and DS have been selected and applied for tree height estimation using the RVoG and RMoG$_L$ models. DS method improved the result of the RVoG model considerably while it had only a slight effect on the RMoG$_L$ model. This shows the stability of the RMoG$_L$ model to the method used for SHP selection. Using DS also reduces blurring and patchiness. Since the adaptive methods require longer computations, a trade-off should be made between the sensitivity of the data and speed of the computation. In case of the RMoG_L model, according to the complexity of the model itself and light improvement of the height estimation accuracy, using heavy-task methods is not recommended. In the case of the RVoG model, it has been observed in this chapter that using adaptive estimation of the complex coherence can improve the accuracy, especially in tropical dense forests with high variation of topography.

7 Synthesis

7.1 Research findings and conclusions

This chapter addresses the main research findings and conclusions of the dissertation. It summarizes how the objectives were achieved and the research questions have been answered. It also presents the direction for future research and recommendations.

- **Objective 1: To explore the possibilities of improving temporal decorrelation modeling by using a more accurate backscattering scenario.**

  In this objective, I explored how height estimation accuracy can be improved in the presence of temporal decorrelation is present. For this purpose, I combined a Fourier-Legendre series with the temporal decorrelation scenario of the RMoG model. According to this model, the main cause of the temporal decorrelation is the scatterers movement in the vertical direction, e.g. the movement of leaves and small branches induced by the wind. This motion can be represented by a Gaussian function. To avoid having an ill-posed equation system, I employed the first order approximation. In addition a finite number of Fourier-Legendre series was used as the structure function. Fourier-Legendre series have previously been used in Polarimetric Coherence Tomography (PCT) to reconstruct the vertical profile of the trees in details. I investigated the possibility of using Fourier-Legendre series and the motion component of the RMoG model and called the new modified model the RMoG$_L$ model. I tested the RMoG$_L$ model on P- and L-band PolInSAR images acquired during BioSAR2010 campaign designed and conducted by ESA.

  I further applied the RVoG and RMoG models on the same dataset. The RVoG model neglects the presence of temporal decorrelation. It assumes that the structure function is an exponential function. For the RMoG model, a similar structure function is used. The main difference is the movement of objects that increases from the bottom to the top of the vegetation layer. To compare the RVoG, RMoG and RMoG$_L$ models I used a Lidar height map. Field data were available for regions defined according to the campaign design. These datasets were compared with the resulting height maps from the three models.

  The RMoG$_L$ model delivers a tree height map which is more accurate than those obtained from the other models. For L-band, however, the RMoG model had a similar performance. The RVoG model showed the least accurate results in both P- and L-bands. The RMOG$_L$ model showed to be of importance for future SAR sensors which are aimed at tree height and biomass estimation.

  The following research question has been answered:

  - *Can using a more accurate structure function improve height estimation accuracy by PolInSAR?*

Changing the structure function of the RMoG model and replacing it with the Fourier-Legendre series improved height estimation accuracy on P- and L-bands from a boreal forest. The RMoG$_L$ model increased the height estimation accuracy as compared to the RVoG and RMoG models for P-band. For L-band the RMoG model was equally good due to the different penetration depth of the SAR signal and strong double-bounce scattering. Moreover, the RMoG$_L$ model showed more flexibility in modeling different structure types of the vegetation layer (Chapter 3). This conclusion can be useful as a support for future satellite missions operating on P-band. The multi-step procedure proposed in Chapter 3 for solving an equation system with more unknown parameters than the observations must be considered when dealing with more complicated vegetated areas.

- **Objective 2: To modify PCT and combine it with temporal decorrelation scenario for processing tomographic SAR data.**

In this objective, I explored if tomographic SAR data processing can be merged with the temporal decorrelation function of the RMoG model. To do so, I investigated how to expand the RMoG$_L$ model for multi-baseline SAR images. The previously introduced PCT model was combined with the motion of objects in the vertical direction. The dataset was a tomostack of L-band images acquired during the AfriSAR campaign performed by ESA in Gabon. A tropical forest located at La Lope national park in Gabon was selected as the study region. It has a heterogeneous multi-layer complicated forest cover.

The optimum number of Fourier-Legendre terms was selected for each pixel separately. This could be done since the available multi-baseline SAR images provided sufficient observations for solving the equation system. The number of terms started from two and incrementally increased. Motion components were added as unknown parameters to these non-linear systems. The optimum number was determined after solving the equations with different numbers of terms. According to Chapter 4, more terms were needed for pixels with taller trees and multi-layer tree coverage to acquire accurate height estimation. To evaluate the accuracy a Lidar height map was used as ground truth. A novelty in this chapter was the use of histograms in addition to the RMSE values. They provide a better understanding of how height maps obtained by tomoSAR differ from those obtained by Lidar data.

The combination of the PCT model with the temporal decorrelation scenario of the RMoG model increases the accuracy of forest height estimation. This is of value for tropical forests inventories where it has been a challenge to estimate tree height and biomass. Future satellite sensors will be able to collect multi-baseline SAR data and thus rely on the findings of this objective. The following research questions have been answered:

- *How can the PCT model be modified to mitigate for temporal decorrelation caused by objects movements in vertical direction?*

  Results showed that the modified PCT model improves tree height estimation considerably.

- *How many terms are needed to make a trade-off between vertical reconstruction detail and the number of model parameters to be estimated?*

  Using the Modified PCT model requires to select an optimum number of terms for each region of the area. This was done using trial and error. Starting from two terms of the series in addition to the motion components, terms were added one by one. For pixels and regions with trees taller than 20 m, more terms were required, whereas shorter trees, especially lower than 10 m, were adequately modeled by two basic terms of Fourier-Legendre series. Properly dealing with temporal decorrelation and use of an optimized structure function based upon the vegetation layer is essential for accurately observing tropical forests.

- **Objective 3: To exploit the effect of taking into account temporal decorrelation in height estimation modeling on biomass mapping accuracy.**

In this objective, I investigated the effect of using the modified RMoG$_L$ model that takes into account the temporal decorrelation on biomass estimation accuracy. As PolInSAR can provide us with high coverage height maps, we can use such height maps to obtain biomass. To do so, allometric equations are needed that relate height or other biophysical parameters to the above ground biomass. As described in Chapters 3 and 4, height estimation improved by modifying the conventional RVoG and RMoG models. In this objective, the proposed RMoG$_L$ model is employed to derive the height map of the Remingstorp test site, Sweden. Moreover, the RVoG and RMoG models were applied. To transform height into biomass, I further developed a new allometric equation with the help of measured biomass values during the fieldwork performed for BioSAR2010 campaign. In total, more than 200 field plots were available. Modeled data were related to height values by a regression model. For this purpose, I examined several data splitting methods to choose training and test datasets. Additionally, several regression methods have been applied.

This study concluded that taking the temporal decorrelation into account for estimating tree height has a significant effect on providing accurate biomass maps. The following research question has been answered:

▶ *Is biomass estimation accuracy affected by mitigation of temporal decorrelation and if the answer is yes, how much?*

After compensation of temporal decorrelation, the accuracy of biomass estimation improved on average by 10%. Thus, for producing biomass maps of a required accuracy, the temporal decorrelation component should be taken into account. The best method for relating biomass to PolInSAR height was shown to be the exponential curve. Moreover, as discussed in Chapter 5, in forests with various levels of biomass, it is useful to separate the area according to the different height clusters and use different regression lines for each cluster. This is particularly of value in tropical forests where biomass is high and biomass estimation is challenging.

▶ **Objective 4: To assess the sensitivity of PolInSAR height estimation models to different methods of obtaining the complex coherence.**

In this objective, I investigated the sensitivity of the newly proposed RMoG_L model to the complex coherence estimation method. As the complex coherence estimation acts as the base for estimation height, the method is important. To do so, I started with the first step of complex coherence estimation which is finding homogeneous pixels. There are several methods to do so. Conventionally, a rectangular area is defined and surrounding pixels are assumed to be homogeneous. Newly proposed methods, modify the similar pixels selection procedure. Within this expanded area, any pixel that satisfies the homogeneity condition is chosen irrespective of the final shape of the area. These adaptive methods for estimation complex coherence act based on only polarimetric or polarimetric interferometric information. I selected Fixed-point and Double similarity methods and applied them to the multi-baseline tomostack of La Lope national park. These methods were compared with the Boxcar and Refined Lee methods. The outcome of the two methods then served as inputs for estimating unknown parameters of the RVoG and RMoG_L models. In addition, the influence of window size was examined. The height maps obtained using different settings were compared to the Lidar map to assess the accuracy.

It was concluded that adaptive methods for obtaining coherence increase the height estimation accuracy, no matter which height estimation model is selected. This, however, comes at the cost of longer computations. The following research questions have been answered:

▶ *What is the dependency of height estimation accuracy on the complex coherence estimation method?*

The better performance of the adaptive methods for choosing homogeneous pixels inside a sliding window was shown in Chapter 6. The Fixed-point and Double similarity have been examined for tree height estimation using the RVoG and RMoGL models. Double similarity improved the result of the RVoG model considerably while it did not have an equally strong effect on the results of the RMoG_L model. Using Double similarity also reduced blurring and patchiness.

- *Does it pay off to invest on using adaptive methods for estimating complex coherence in combination with elaborated PolInSAR height estimation models?*

  Since the computational task of the double similarity is twice large as that for other methods, a trade-off should be considered between the sensitivity of the data and the speed of the computation. Because of the complicated nature of the RMoG_L model, combining adaptive methods for coherence estimation is not recommended.

7.2 Reflections

This research focused on improving tree height estimation accuracy in different forested areas by using a modified physical model applied on P- and L-band. This was accomplished in four steps:

- Fourier-Legendre series were selected to reconstruct the vertical structure of trees. This function was combined with a first-order approximation of Gaussian movement of scattering objects in the vertical direction. Combination of a detailed vertical reconstruction and temporal decorrelation compensation was introduced to improve the height estimation accuracy of a single-baseline PolInSAR data.
- Providing a solution for handling temporal decorrelation in processing tomostack SAR data, the PCT model was merged with the temporal decorrelation related to the leaves and branches motion and the number of optimum structure function terms was decided according to the biophysical and geometrical parameters of trees.
- Assessing the accuracy of biomass maps obtained by PolInSAR height, a modification was proposed along with the conventional RVoG model. For developing new allometric equations, the best data splitting and regression methods were selected among different available options.
- Assessing the effect of adaptive complex coherence estimation methods on the final resulting height maps by employing different ways of choosing homogeneous pixels and examine the impact in combination with the RVoG and RMoG_L models.

These steps contributed to the improvement of forest height estimation by means of PolInSAR applied to single and multi-baseline data.

According to the goal No.15 of the sustainable development goals announced by United Nations (UN), the protection, and revitalization of forests and the combating of deforestation plays an important role toward sustainable development. The forests used to cover 4.1 billion hectares on the whole planet in 2000, whereas in 2015 the coverage decreased to 4.0 billion hectares. The rate of deforestation is alarming but it has slowed down after 2005. This shows that global efforts have been effective. The UN–REDD (Reducing Emissions from Deforestation and Forest Degradation) program was launched in 2008 calling the experts to develop new models and share their expertise toward estimating biomass and forest biophysical parameters. This dissertation contributes to the global expert communities trying to save the forests worldwide. The finding of this thesis showed that handling a systematic error in the PolInSAR height estimation models will impact the quality of mapping forests.

Another aspect that the findings from this research are going to have an impact is sharing the developed allometric equations in Chapter 5 with the remote sensing portal for foresters built by the FAO (Food and Agriculture Organization). This portal will give national organizations and responsible people an opportunity to inspect the results we achieved and how to use them at local scale. The lack of accuracy was the main shortcoming of the RVoG model that was overcome in the past by combining the physical motion and RVoG backscatter scenarios. I had the pleasure to discover how the RMoG_L model for reconstructing the motion of scatterers in the vertical direction improved the accuracy of estimated tree heights. This contribution is going to be at the disposal of national and global experts via UN-REDD portals and thus may contribute toward sustainable forest management. According to the characteristics of this dissertation and initial objectives, several aspects of modifying the height estimation model were considered. For instance, defining the non-linear equation system, identifying ways of solving it and assigning the initial values are important achievements. If the local and national organizations have access to remote sensing portal of UN to upload their knowledge about different forest areas, then it can be transferred to the developing new technology and data processing techniques generally and to stabilize the equation systems specifically. Moreover, local expert system knowledge can be employed to define the level of complexity of the required for height estimation modeling, e.g. defining the optimum number of terms in Fourier-Legendre series as discussed in Chapter 3 and 4. It would be good to be involved in development of the future sensors, i.e. BIOMASS and NISAR (NASA-ISRO Synthetic Aperture Radar) to provide the opportunity to test the newly developed models.

Apart from the large effects the forest loss has on biodiversity and humanity, a major consequence of deforestation is the emission of heat-trapping carbon dioxide (CO_2) into the atmosphere. Forests have the role of carbon sinks on our planet. Thus when destroyed or burnt they release carbon into the atmosphere. CO_2 emission is the main component of human factors affecting the climate change. According to REDD, forest clear-cutting and conversion to other land use is responsible for approximately 10% of net global carbon emissions. Therefore, solving the problem of deforestation is a prerequisite for any effective response to climate change. After witnessing the many warning signs of climate change and global warming earlier than expected, mapping and monitoring of forest areas should be taken more seriously. There, remote sensing plays an important role. We can stabilize a simple global monitoring system with the help of future sensors and then elaborate it targeting the needs of individual countries based on the gathered knowledge in expert systems.

An important aspect covered in this thesis was transforming height maps into biomass maps that later should contribute to carbon stock estimates. Surprisingly, I discovered only a few sources that was addressed in the contribution of height maps to the final biomass estimation accuracy. Here I had to answer the question: "How much do we need to improve the height estimation models for biomass mapping purpose?". Unfortunately, there is no unique response to that question since there is no common agreement between foresters and other responsible organizations. For some areas, like European forests that are already well studied and technology is sufficiently developed, I strongly recommend to apply the more accurate models since they can be a pilot place to test how PolInSAR affects the carbon stock management. I propose to perform broad campaigns by airborne sensors and later by the spaceborne sensors in these areas to develop models with sufficient accuracy. The results demonstrate the capability of PolInSAR to obtain biomass maps especially for the satellite BIOMASS mission that aims to produce biomass maps with wall-to-wall coverage of forests.

7.3 Recommendations for future research

This thesis explored how to tackle temporal decorrelation in PolInSAR caused by objects movements induced by wind. The proposed models improved height estimation accuracy by PolInSAR but had several limitations on the other hand. The following recommendations are made to further investigate and improve in the proposed methods:

1. The temporal decorrelation model discussed in this thesis focuses only on objects movements in the vertical direction e.g. induced by wind. Changes in the moisture content and seasonal changes, as well as natural phenomena like landslides, are not taken into account. We recommend modifying the model further to include moisture content and seasonal changes as well as natural disasters like landslides.
2. The computational task of the proposed methodologies is still an important issue especially in processing large datasets (big data). An efficient model should be adopted as a trade–off of having both temporal decorrelation and an accurate vertical structure function. Additionally, using adaptive methods for selection of homogeneous pixels improves the accuracy of height estimation of simpler models like the RVoG model. Therefore, replacing complex coherence estimation methods with more efficient ones should be further explored.
3. All proposed methodologies, especially adaptive complex coherence estimation, are based on the estimation of the coherency and covariance

matrices. Regretfully, there is a lack of knowledge about the uncertainty that comes with estimation of these matrices. This should be addressed in future studies.

4. Unfortunately, in-situ measurement of the tree height and biomass were not available from the tropical forest located in Gabon. This happened due to the timing for releasing the complete dataset by European Space Agency. It is recommended to compare the results of the modified PCT model with average tree height inside each sampling plot and moreover, check the final accuracy after using adaptive methods for coherence estimation using the field data as well as the Lidar data similar to the process explained in Chapter 3 and 5.

5. The development of an index for structural complexity and various wind conditions within forested areas, followed by selecting height estimation model should be further investigated. This would save time and resources in case of processing frequently renewed datasets in the near future.

Bibliography

Ahmed, R., Siqueira, P., Hensley, S., Chapman, B., Bergen, K., 2011. A survey of temporal decorrelation from spaceborne l-band repeat-pass insar. Remote Sensing of Environment 115, 2887–2896.

Askne, J., Fransson, J., Santoro, M., Soja, M., Ulander, L., 2013. Model-based biomass estimation of a hemi-boreal forest from multitemporal tandem-x acquisitions. Remote Sensing 5, 5574–5597.

Askne, J., Santoro, M., 2012. Experiences in boreal forest stem volume estimation from multitemporal C-band InSAR, in: Recent Interferometry Applications in Topography and Astronomy. InTech.

Ballester-Berman, D., Lopez-Sanchez, J., 2010. Applying the freeman–durden decomposition concept to polarimetric SAR interferometry. IEEE Transactions on Geoscience and Remote Sensing 48, 466–479.

Balzter, H., Rowland, C., Saich, P., 2007. Forest canopy height and carbon estimation at monks wood national nature reserve, UK, using dual-wavelength SAR interferometry. Remote Sensing of Environment 108, 224–239.

Bamler, R., Hartl, P., 1998. Synthetic aperture radar interferometry. Inverse problems 14, R1.

Boerner, W., Yan, W.L., Xi, A.Q., Yamaguchi, Y., 1992. Basic concepts of radar polarimetry, in: Direct and Inverse Methods in Radar Polarimetry. Springer, pp. 155–245.

Chave, J., Coomes, D., Jansen, S., Lewis, S., Swenson, N., Zanne, A., 2009. Towards a worldwide wood economics spectrum. Ecology letters 12, 351–366.

Chen, S., Wang, X., Sato, M., 2012. PolInSAR complex coherence estimation based on covariance matrix similarity test. IEEE Transactions on Geoscience and Remote Sensing 50, 4699–4710.

Cho, B., Kim, Y., 2007. Multilook coherence estimation using adaptive weighted window in interferometric SAR. Journal of Electromagnetic Waves and Applications 21, 359–365.

Cloude, S., 2005. Pol-InSAR training course. Radio Science .

Cloude, S., 2006. Polarization coherence tomography. Radio Science 41, 1–27.

Cloude, S., 2007a. Dual-baseline coherence tomography. IEEE Geoscience and Remote Sensing Letters 4, 127–131.

Cloude, S., 2007b. Dual-baseline coherence tomography. IEEE Geoscience and Remote Sensing Letters 4, 127–131.

Cloude, S., 2008. Multifrequency 3-D imaging of tropical forest using polarization coherence tomography, in: Synthetic Aperture Radar (EUSAR), 2008 7th European Conference on, VDE. pp. 1–4.

Cloude, S., 2010. Polarisation: applications in remote sensing. Oxford University Press.

Cloude, S., Papathanassiou, K., 1998a. Polarimetric SAR interferometry. IEEE Transactions on Geoscience and Remote Sensing 36, 1551–1565.

Cloude, S., Papathanassiou, K., 1998b. Polarimetric SAR interferometry. IEEE Transactions on geoscience and remote sensing 36, 1551–1565.

Cloude, S., Papathanassiou, K., 2002. A 3-stage inversion process for polarimetric SAR interferometry. Proceedings EUSAR 2002 , 279–282.

Cloude, S., Papathanassiou, K., 2003. Three-stage inversion process for polarimetric SAR interferometry. IEEE Proceedings-Radar, Sonar and Navigation 150, 125–134.

Cloude, S., Pottier, E., 1996. A review of target decomposition theorems in radar polarimetry. IEEE Transactions on Geoscience and Remote Sensing 34, 498–518.

Colin, E., Titin-Schnaider, C., Tabbara, W., 2005. Coherence optimization methods for scattering centers separation in polarimetric interferometry. Journal of electromagnetic waves and applications 19, 1237–1250.

Colin, E., Titin-Schnaider, C., Tabbara, W., 2006. An interferometric coherence optimization method in radar polarimetry for high-resolution imagery. IEEE Transactions on Geoscience and Remote Sensing 44, 167–175.

Conradsen, K., Nielsen, A., Schou, J., Skriver, H., 2003. A test statistic in the complex wishart distribution and its application to change detection in polarimetric SAR data. IEEE Transactions on Geoscience and Remote Sensing 41, 4–19.

Dobson, C., Ulaby, F., Pierce, L., Sharik, T., Bergen, K., Kellndorfer, J., Kendra, J., Li, E., Lin, Y.C., Nashashibi, A., et al., 1995. Estimation of forest biophysical characteristics in northern michigan with sir-c/x-sar. IEEE Transactions on Geoscience and Remote Sensing 33, 877–895.

Drake, J., Knox, R., Dubayah, R., Clark, D., Condit, R., Blair, B., Hofton, M., 2003. Above-ground biomass estimation in closed canopy neotropical forests using lidar remote sensing: Factors affecting the generality of relationships. Global ecology and biogeography 12, 147–159.

Dubayah, R., Sheldon, S., Clark, D., Hofton, M., Blair, B., Hurtt, G., Chazdon, R., 2010. Estimation of tropical forest height and biomass dynamics using lidar remote sensing at La Selva, Costa Rica. Journal of Geophysical Research: Biogeosciences 115.

Dubois-Fernandez, P., Dupuis, X., Capdessus, P., Baque, R., 2016. Preliminary results of the AfriSAR campaign, in: EUSAR 2016: 11th European Conference on Synthetic Aperture Radar, Proceedings of, VDE. pp. 1–3.

Florian, K., Kostas, P., Irena, H., Dirk, H., 2006. Forest height estimation in tropical rain forest using pol-insar techniques, in: Geoscience and Remote Sensing Symposium, 2006. IGARSS 2006. IEEE International Conference on, pp. 2193–2196.

Fransson, J.E., Magnusson, M., Olsson, H., Eriksson, L.E., Folkesson, K., Sandberg, G., Santoro, M., Ulander, L., 2008. Detection of clear-cuts using alos palsar satellite images, in: Synthetic Aperture Radar (EUSAR), 2008 7th European Conference on, VDE. pp. 1–4.

Garestier, F., Champion, I., Dubois-Fernandez, P., Paillou, P., Dupuis, X., 2005. Polar and PolinSAR analysis of pine forest at L and P band on high resolution data, in: Geoscience and Remote Sensing Symposium, 2005. IGARSS'05. Proceedings. 2005 IEEE International, IEEE. pp. 1093–1096.

Garestier, F., Dubois-Fernandez, P., Champion, I., 2008. Forest height inversion using high-resolution P-band Pol-InSAR data. IEEE Transactions on Geoscience and Remote Sensing 46, 3544–3559.

Garestier, F., Le Toan, T., 2010. Estimation of the backscatter vertical profile of a pine forest using single baseline P-band PolInSAR data. IEEE Transactions on Geoscience and Remote Sensing .

Ghasemi, N., Tolpekin, V., Stein, A., 2018a. Assessment of forest above-ground biomass estimation from PolInSAR in the presence of temporal decorrelation. Remote Sensing 10, 815.

Ghasemi, N., Tolpekin, V., Stein, A., 2018b. A modified model for estimating tree height from PolinSAR with compensation for temporal decorrelation. International Journal of Applied Earth Observation and Geoinformation 73, 313 – 322. doi:10.1016/j.jag.2018.06.022.

Gizachew, B., Solberg, S., Næsset, E., Gobakken, T., Bollandsås, O., Breidenbach, J., Zahabu, E., Mauya, E., 2016. Mapping and estimating the total living biomass and carbon in low-biomass woodlands using landsat 8 CDR data. Carbon Balance and Management 11, 13.

Goldstein, R., Zebker, H., Werner, C., 1988. Satellite radar interferometry: Two-dimensional phase unwrapping. Radio science 23, 713–720.

Guillaso, S., Reigber, A., 2005. Polarimetric SAR tomography, in: ESA Special Publication, p. 4.

Hajnsek, I., Kugler, F., Lee, S.K., Papathanassiou, K., 2009. Tropical-forest-parameter estimation by means of Pol-InSAR: The INDREX-II campaign. IEEE transactions on Geoscience and Remote Sensing 47, 481–493.

Hajnsek, I., Pardini, M., Horn, R., Scheiber, R., Jaeger, M., Keller, M., Gesswein, D., Papathanassiou, K., Reigber, A., 2016. 3-D SAR imaging of african forests: results from the AfriSAR campaign at P-and L-band, in: EUSAR 2016: 11th European Conference on Synthetic Aperture Radar, Proceedings of, VDE. pp. 1–4.

Hansen, E.H., Gobakken, T., Bollandsås, O.M., Zahabu, E., Næsset, E., 2015. Modeling aboveground biomass in dense tropical submontane rainforest using airborne laser scanner data. Remote Sensing 7, 788–807.

Hosking, J., Wallis, J., Wood, E., 1985. Estimation of the generalized extreme-value distribution by the method of probability-weighted moments. Technometrics 27, 251–261.

Houghton, R., House, J., Pongratz, J., Van der Werf, G., DeFries, R., Hansen, M., Quéré, C., Ramankutty, N., 2012. Carbon emissions from land use and land-cover change. Biogeosciences 9, 5125–5142.

Huang, Y., Ferro-Famil, L., Lardeux, C., 2011. Polarimetric SAR tomography of tropical forests at P-band, in: Geoscience and Remote Sensing Symposium (IGARSS), 2011 IEEE International, IEEE. pp. 1373–1376.

Hyde, P., Nelson, R., Kimes, D., Levine, E., 2007. Exploring LiDAR–RaDAR synergy—predicting aboveground biomass in a southwestern ponderosa pine forest using LiDAR, SAR and InSAR. Remote Sensing of Environment 106, 28–38.

Jager, M., Neumann, M., Guillaso, S., Reigber, A., 2007. A self-initializing PolInSAR classifier using interferometric phase differences. IEEE Transactions on Geoscience and remote sensing 45, 3503–3518.

Jia, W., Zhang, H., He, X., Wu, Q., 2006. A comparison on histogram based image matching methods, in: Video and Signal Based Surveillance, 2006. AVSS'06. IEEE International Conference on, IEEE. pp. 97–103.

Kim, S., Lee, J., 2012. Scale invariant small target detection by optimizing signal-to-clutter ratio in heterogeneous background for infrared search and track. Pattern Recognition 45, 393–406.

Kugler, F., 2015. Pol-InSAR forest height estimation at different frequencies: Opportunities and limitations. Ph.D. thesis. Technical University Munich (TUM).

Kugler, F., Lee, S.K., Hajnsek, I., Papathanassiou, K.P., 2015. Forest height estimation by means of Pol-InSAR data inversion: The role of the vertical wavenumber. IEEE Transactions on Geoscience and Remote Sensing 53, 5294–5311.

Lavalle, M., 2009. Full and compact polarimetric radar interferometry for vegetation remote sensing. Ph.D. thesis. Université Rennes 1.

Lavalle, M., 2017. AfriSAR campaign and NASA/JPL contribu6on. techreport. NASA JPL.

Lavalle, M., Hensley, S., 2012. Demonstration of repeat-pass PolInSAR using UAVSAR: The RMOG model, in: Geoscience and Remote Sensing Symposium (IGARSS), 2012 IEEE International, IEEE. pp. 5876–5879.

Lavalle, M., Hensley, S., 2015. Extraction of structural and dynamic properties of forests from polarimetric-interferometric SAR data affected by temporal decorrelation. IEEE Transactions on Geoscience and Remote Sensing 53, 4752–4767.

Lavalle, M., Hensley, S., Lou, Y., Saatchi, S., Pinto, N., Simard, M., Fatoyinbo, T., Duncanson, L., Dubayah, R., Hofton, M., et al., 2016a. Canopy height and vertical structure from multibaseline polarimetric insar: First results of the 2016 nasa/esa afrisar campaign, in: AGU Fall Meeting Abstracts.

Lavalle, M., Khun, K., 2014. Three-baseline inSAR estimation of forest height. IEEE Geoscience and Remote Sensing Letters 11, 1737–1741.

Lavalle, M., Shiroma, G.H., Agram, P., Gurrola, E., Sacco, G.F., Rosen, P., 2016b. PLANT: Polarimetric-interferometric lab and analysis tools for ecosystem and land-cover science and applications, in: Geoscience and Remote Sensing Symposium (IGARSS), 2016 IEEE International, IEEE. pp. 5354–5357.

Lavalle, M., Simard, M., Hensley, S., 2012. A temporal decorrelation model for polarimetric radar interferometers. IEEE Transactions on Geoscience and Remote Sensing 50, 2880–2888.

Lavalle, M., Simard, M., Solimini, D., Pottier, E., 2010. Height-dependent temporal decorrelation for PolinSAR and TomoSAR forestry applications, in: Synthetic Aperture Radar (EUSAR), 2010 8th European Conference on, pp. 1–4.

Lavalle, M., Solimini, D., Pottier, E., Desnos, Y.L., 2008. PolInSAR for forest biomass retrieval: PALSAR observations and model analysis, in: Geoscience and Remote Sensing Symposium, 2008. IGARSS 2008. IEEE International, IEEE. pp. III–302.

Le Quéré, C., Moriarty, R., Andrew, R.M., Canadell, J.G., Sitch, S., Korsbakken, J.I., Friedlingstein, P., Peters, G.P., Andres, R.J., Boden, T.A., et al., 2015. Global carbon budget 2015. Earth System Science Data 7, 349–396.

Le Toan, T., Beaudoin, A., Riom, J., Guyon, D., 1992. Relating forest biomass to SAR data. IEEE Transactions on Geoscience and Remote Sensing 30, 403–411.

Le Toan, T., Quegan, S., Davidson, M., Balzter, H., Paillou, P., Papathanassiou, K., Plummer, S., Rocca, F., Saatchi, S., Shugart, H., et al., 2011. The BIOMASS mission: Mapping global forest biomass to better understand the terrestrial carbon cycle. Remote sensing of environment 115, 2850–2860.

Lee, J., Grunes, M., Ainsworth, T., Hajnsek, I., Mette, T., Papathanassiou, K., 2005. Forest classification based on L-band polarimetric and interferometric SAR data, in: ESA Special Publication, p. 6.

Lee, J., Grunes, M., Ainsworth, T., Schuler, D., Cloude, S., 2003a. Coherence estimation and speckle filtering based on scattering properties, in: Geoscience and Remote Sensing Symposium, 2003. IGARSS'03. Proceedings. 2003 IEEE International, IEEE. pp. 705–707.

Lee, J.S., 1986. Speckle suppression and analysis for synthetic aperture radar images. Optical engineering 25, 255636.

Lee, J.S., Cloude, S.R., Papathanassiou, K.P., Grunes, M.R., Woodhouse, I.H., 2003b. Speckle filtering and coherence estimation of polarimetric SAR interferometry data for forest applications. IEEE Transactions on Geoscience and Remote Sensing 41, 2254–2263.

Lee, J.S., Grunes, M.R., De Grandi, G., 1999. Polarimetric SAR speckle filtering and its implication for classification. IEEE Transactions on Geoscience and remote sensing 37, 2363–2373.

Lee, J.S., Pottier, E., 2009. Polarimetric radar imaging: from basics to applications. CRC press.

Lee, S.K., Kugler, F., Papathanassiou, K., Hajnsek, I., 2012. Quantification and compensation of temporal decorrelation effects in polarimetric SAR interferometry, in: Geoscience and Remote Sensing Symposium (IGARSS), 2012 IEEE International, pp. 3106–3109.

Lee, S.K., Kugler, F., Papathanassiou, K.P., Hajnsek, I., 2013. Quantification of temporal decorrelation effects at L-band for polarimetric SAR interferometry applications. IEEE Journal of Selected Topics in Applied Earth Observations and Remote Sensing 6, 1351–1367.

Li, Z., Guo, M., Wang, Z., Zhao, L., 2014. Forest-height inversion using repeat-pass spaceborne PolInSAR data. Science China Earth Sciences 57, 1314–1324.

Lopez-Martinez, C., Fabregas, X., Pottier, E., 2005. Wavelet transform-based interferometric SAR coherence estimator. IEEE Signal processing letters 12, 831–834.

Lopez-Sanchez, J.M., Ballester-Berman, J.D., Marquez-Moreno, Y., 2007. Model limitations and parameter-estimation methods for agricultural applications of polarimetric SAR interferometry. IEEE Transactions on Geoscience and Remote Sensing 45, 3481–3493.

Lu, D., 2005. Aboveground biomass estimation using landsat TM data in the Brazilian amazon. International Journal of Remote Sensing 26, 2509–2525.

Lu, D., Chen, Q., Wang, G., Liu, L., Li, G., Moran, E., 2016. A survey of remote sensing-based aboveground biomass estimation methods in forest ecosystems. International Journal of Digital Earth 9, 63–105.

Martinez, W.L., Martinez, A.R., 2007. Computational statistics handbook with MATLAB. CRC press.

Mercer, B., Zhang, Q., Schwaebisch, M., Denbina, M., Cloude, S., 2009. Forest height and ground topography at l-band from an experimental single-pass airborne PolInSAR system, in: Proc. of 4th Int. Workshop on Science and Applications of SAR Polarimetry and Polarimetric Interferometry, Frascati, Italy, H. Lacoste and L. Ouwehand, Eds, p. 16.

Mette, T., Papathanassiou, K., Hajnsek, I., Pretzsch, H., Biber, P., 2004. Applying a common allometric equation to convert forest height from PolInSAR data to forest biomass, in: Geoscience and Remote Sensing Symposium, 2004. IGARSS'04. Proceedings. 2004 IEEE International, IEEE.

Minh, D.H.T., Le Toan, T., Rocca, F., Tebaldini, S., d'Alessandro, M.M., Villard, L., 2014. Relating P-band synthetic aperture radar tomography to tropical forest biomass. IEEE Transactions on Geoscience and Remote Sensing 52, 967–979.

Minh, D.H.T., Le Toan, T., Rocca, F., Tebaldini, S., Villard, L., Réjou-Méchain, M., Phillips, O.L., Feldpausch, T.R., Dubois-Fernandez, P., Scipal, K., et al., 2016. SAR tomography for the retrieval of forest biomass and height: Cross-validation at two tropical forest sites in French Guiana. Remote Sensing of Environment 175, 138–147.

Montesano, P., Cook, B., Sun, G., Simard, M., Nelson, R., Ranson, K., Zhang, Z., Luthcke, S., 2013. Achieving accuracy requirements for forest biomass mapping: A spaceborne data fusion method for estimating forest biomass and LiDAR sampling error. Remote Sensing of Environment 130, 153–170.

Mullissa, A., Tolpekin, V., Stein, A., 2017. Scattering property based contextual PolSAR speckle filter. International Journal of Applied Earth Observation and Geoinformation 63, 78–89.

Muukkonen, P., Heiskanen, J., 2007. Biomass estimation over a large area based on standwise forest inventory data and ASTER and MODIS satellite data: A possibility to verify carbon inventories. Remote Sensing of Environment 107, 617–624.

Næsset, E., 2002. Predicting forest stand characteristics with airborne scanning laser using a practical two-stage procedure and field data. Remote sensing of environment .

Neeff, T., Dutra, L.V., dos Santos, J.R., Freitas, C.d.C., Araujo, L.S., 2005. Tropical forest measurement by interferometric height modeling and P-band radar backscatter. Forest Science 51, 6.

Nelson, R., Margolis, H., Montesano, P., Sun, G., Cook, B., Andersen, H.E., Pellat, F.P., Fickel, T., Kauffman, J., Prisley, S., et al., 2017. Lidar-based estimates of aboveground biomass in the continental US and mexico using ground, airborne, and satellite observations. Remote Sensing of Environment 188, 127–140.

Neumann, M., Ferro-Famil, L., Reigber, A., 2008. Multibaseline polarimetric SAR interferometry coherence optimization. IEEE Geoscience and Remote Sensing Letters 5, 93–97.

Neumann, M., Ferro-Famil, L., Reigber, A., 2010. Estimation of forest structure, ground, and canopy layer characteristics from multibaseline polarimetric interferometric SAR data. IEEE Transactions on Geoscience and Remote Sensing 48, 1086–1104.

Neumann, M., Saatchi, S.S., Ulander, L.M., Fransson, J.E., 2011. Parametric and non-parametric forest biomass estimation from PolInSAR data, in: Geoscience and Remote Sensing Symposium (IGARSS), 2011 IEEE International, IEEE. pp. 420–423.

Ni-Meister, W., Lee, S., Strahler, A.H., Woodcock, C.E., Schaaf, C., Yao, T., Ranson, K.J., Sun, G., Blair, J.B., 2010. Assessing general relationships between aboveground biomass and vegetation structure parameters for improved carbon estimate from lidar remote sensing. Journal of Geophysical Research: Biogeosciences 115, G2.

Noble, I., Bolin, B., Ravindranath, N., Verardo, D., Dokken, D., 2000. Land use, land use change, and forestry. Cambridge University Press.

Papathanassiou, K., Cloude, S.R., 2003. The effect of temporal decorrelation on the inversion of forest parameters from PoIInSAR data, in: International Geoscience and Remote Sensing Symposium, pp. III–1429.

Papathanassiou, K.P., Cloude, S.R., 2001. Single-baseline polarimetric SAR interferometry. IEEE Transactions on Geoscience and Remote Sensing 39, 2352–2363.

Pardini, M., Tello, M., Cazcarra-Bes, V., Papathanassiou, K.P., Hajnsek, I., 2018. L- and P-band 3-d SAR reflectivity profiles vs. Lidar waveforms: the AfriSAR case. IEEE Journal of Selected Topics in Applied Earth Observations and Remote Sensing 11, 1–16.

Pascal, F., Chitour, Y., Ovarlez, J.P., Forster, P., Larzabal, P., 2008a. Covariance structure maximum-likelihood estimates in compound Gaussian noise: Existence and algorithm analysis. IEEE Transactions on Signal Processing 56, 34–48.

Pascal, F., Forster, P., Ovarlez, J.P., Larzabal, P., 2008b. Performance analysis of covariance matrix estimates in impulsive noise. IEEE Transactions on Signal Processing 56, 2206–2217.

Pass, G., Zabih, R., 1999. Comparing images using joint histograms. Multimedia systems 7, 234–240.

Picard, N., Saint-André, L., Henry, M., 2012. Manual for building tree volume and biomass allometric equations: From field measurement to prediction. FAO/CIRAD .

Picard, R.R., Berk, K.N., 1990. Data splitting. The American Statistician 44, 140–147.

Praks, J., Kugler, F., Papathanassiou, K.P., Hajnsek, I., Hallikainen, M., 2007. Height estimation of boreal forest: interferometric model-based inversion at L-and X-band versus HUTSCAT profiling scatterometer. IEEE Geoscience and remote sensing letters 4, 466–470.

Press, W.H., 2007. Numerical recipes 3rd edition: The art of scientific computing. Cambridge university press.

Rahlf, J., Breidenbach, J., Solberg, S., Næsset, E., Astrup, R., 2014. Comparison of four types of 3D data for timber volume estimation. Remote Sensing of Environment 155, 325–333.

Rangaswamy, M., Weiner, D., Ozturk, A., 1995. Computer generation of correlated non-Gaussian radar clutter. IEEE Transactions on Aerospace and Electronic Systems 31, 106–116.

Rauste, Y., 2005. Multi-temporal JERS SAR data in boreal forest biomass mapping. Remote Sensing of Environment 97, 263–275.

Reigber, A., Moreira, A., 2000. First demonstration of airborne SAR tomography using multibaseline L-band data. IEEE Transactions on Geoscience and Remote Sensing 38, 2142–2152.

Reitermanova, Z., 2010. Data splitting, in: WDS, pp. 31–36.

Rocca, F., 2007. Modeling interferogram stacks. IEEE Transactions on Geoscience and Remote Sensing 45, 3289–3299.

Rolland, J., Vo, V., Bloss, B., Abbey, C., 2000. Fast algorithms for histogram matching: Application to texture synthesis. Journal of Electronic Imaging 9, 39–45.

Rombach, M., Moreira, J., 2003. Description and applications of the multipolarized dual band OrbiSAR-1 InSAR sensor, in: Radar Conference, 2003. Proceedings of the International, IEEE. pp. 245–250.

Rousseeuw, P.J., Leroy, A.M., 2005. Robust regression and outlier detection. John wiley & sons.

Roy, P., Ravan, S.A., 1996. Biomass estimation using satellite remote sensing data—an investigation on possible approaches for natural forest. Journal of biosciences 21, 535–561.

Sandberg, G., Ulander, L.M., Fransson, J., Holmgren, J., Le Toan, T., 2011. L-and P-band backscatter intensity for biomass retrieval in hemiboreal forest. Remote Sensing of Environment 115, 2874–2886.

Santoro, M., Beaudoin, A., Beer, C., Cartus, O., Fransson, J.E., Hall, R.J., Pathe, C., Schmullius, C., Schepaschenko, D., Shvidenko, A., et al., 2015. Forest growing stock volume of the northern hemisphere: Spatially explicit estimates for 2010 derived from Envisat ASAR. Remote Sensing of Environment 168, 316–334.

Schlund, M., Scipal, K., Davidson, M.W., 2017. Forest classification and impact of BIOMASS resolution on forest area and aboveground biomass estimation. International Journal of Applied Earth Observation and Geoinformation 56, 65–76.

Sexton, J.O., Bax, T., Siqueira, P., Swenson, J.J., Hensley, S., 2009. A comparison of lidar, radar, and field measurements of canopy height in pine and hardwood forests of southeastern North America. Forest Ecology and Management 257, 1136–1147.

Seymour, M., Cumming, I., 1994. Maximum likelihood estimation for SAR interferometry, in: Geoscience and Remote Sensing Symposium, 1994. IGARSS'94. Surface and Atmospheric Remote Sensing: Technologies, Data Analysis and Interpretation., International, IEEE. pp. 2272–2275.

Silva, C.A., Saatchi, S.S., Garcia, M., Labriere, N., Klauberg, C., Ferraz, A., Meyer, V., Jeffery, K.J., Abernethy, K., White, L., Zhao, K., Lewis, S.L., Hudak, A.T., 2018. Comparison of small-and large-footprint Lidar characterization of tropical forest aboveground structure and biomass: A case study from central gabon (forthcoming/available online). IEEE Journal of Selected Topics in Applied Earth Observations and Remote Sensing .

Simard, M., Denbina, M., 2018. An assessment of temporal decorrelation compensation methods for forest canopy height estimation using airborne L-band same-day repeat-pass polarimetric SAR interferometry. IEEE

Journal of Selected Topics in Applied Earth Observations and Remote Sensing 11, 95–111.

Simard, M., Hensley, S., Lavalle, M., Dubayah, R., Pinto, N., Hofton, M., 2012. An empirical assessment of temporal decorrelation using the uninhabited aerial vehicle synthetic aperture radar over forested landscapes. Remote Sensing 4, 975–986.

Soja, M.J., Sandberg, G., Ulander, L.M., 2013. Regression-based retrieval of boreal forest biomass in sloping terrain using P-band SAR backscatter intensity data. IEEE Transactions on Geoscience and Remote Sensing 51, 2646–2665.

Solberg, S., Hansen, E., Gobakken, T., Næssset, E., Zahabu, E., 2017. Biomass and InSAR height relationship in a dense tropical forest. Remote Sensing of Environment 192, 166–175.

Stocker, T.F., Qin, D., Plattner, G.K., Tignor, M., Allen, S.K., Boschung, J., Nauels, A., Xia, Y., Bex, V., Midgley, P.M., et al., 2013. Climate change 2013: The physical science basis. Intergovernmental Panel on Climate Change, Working Group I Contribution to the IPCC Fifth Assessment Report (AR5)(Cambridge Univ Press, New York) .

Strikholm, B., 2006. Determining the number of breaks in a piecewise linear regression model. Technical Report. SSE/EFI Working Paper Series in Economics and Finance.

Sun, G., Ranson, K.J., Guo, Z., Zhang, Z., Montesano, P., Kimes, D., 2011. Forest biomass mapping from Lidar and radar synergies. Remote Sensing of Environment 115, 2906–2916.

Tebaldini, S., 2009. Algebraic synthesis of forest scenarios from multibaseline PolInSar data. IEEE Transactions on Geoscience and Remote Sensing 47, 4132–4142.

Tebaldini, S., 2010. Single and multipolarimetric SAR tomography of forested areas: A parametric approach. IEEE Transactions on Geoscience and Remote Sensing 48, 2375–2387.

Tebaldini, S., d'Alessandro, M.M., Dinh, H.T.M., Rocca, F., 2011. P-band penetration in tropical and boreal forests: Tomographical results, in: Geoscience and Remote Sensing Symposium (IGARSS), 2011 IEEE International, IEEE. pp. 4241–4244.

Tebaldini, S., Rocca, F., 2012. Multibaseline polarimetric SAR tomography of a boreal forest at P-and L-bands. IEEE Transactions on Geoscience and Remote Sensing 50, 232–246.

Touzi, R., Lopes, A., Bruniquel, J., Vachon, P.W., 1999. Coherence estimation for SAR imagery. IEEE Transactions on Geoscience and Remote Sensing 37, 135–149.

Treuhaft, R.N., Siqueira, P.R., 2000. Vertical structure of vegetated land surfaces from interferometric and polarimetric radar. Radio Science 35, 141–177.

Ulander, L., Gustavsson, A., Flood, B., Murdin, D., Dubois-Fernandez, P., Depuis, X., Sandberg, G., Soja, M., Eriksson, L., Fransson, J., et al., 2011a. BioSAR 2010: Technical assistance for the development of airborne SAR and geophysical measurements during the BioSAR 2010 experiment: Final report. Eur. Space Agency (ESA), Paris, France, Tech. Rep. Contract No. 4000102285/10/NL/JA/ef .

Ulander, L.M., Gustavsson, A., Dubois-Fernandez, P., Dupuis, X., Fransson, J.E., Holmgren, J., Wallerman, J., Eriksson, L., Sandberg, G., Soja, M., 2011b. BioSAR 2010-a SAR campaign in support to the BIOMASS mission, in: Geoscience and Remote Sensing Symposium (IGARSS), 2011 IEEE International.

Vasile, G., Ovarlez, J.P., Pascal, F., Tison, C., 2010. Coherency matrix estimation of heterogeneous clutter in high-resolution polarimetric SAR images. IEEE Transactions on Geoscience and Remote Sensing 48, 1809–1826.

Vasile, G., Trouvé, E., Lee, J.S., Buzuloiu, V., 2006. Intensity-driven adaptive-neighborhood technique for polarimetric and interferometric SAR parameters estimation. IEEE Transactions on Geoscience and Remote Sensing 44, 1609–1621.

Wang, C., Wang, L., Fu, H., Xie, Q., Zhu, J., 2016. The impact of forest density on forest height inversion modeling from polarimetric InSAR data. Remote Sensing 8, 291.

Wikström, P., Edenius, L., Elfving, B., Eriksson, L.O., Lämås, T., Sonesson, J., Öhman, K., Wallerman, J., Waller, C., Klintebäck, F., 2011. The Heureka forestry decision support system: an overview. Mathematical and Computational Forestry & Natural Resource Sciences 3, 87.

Woodhouse, I., Cloude, S., Papathanassiou, K., Hutchinson, C., 2003. Evaluating PolInSAR tree height and topography retrievals in glen affric, in: Applications of SAR Polarimetry and Polarimetric Interferometry, pp. 1–6.

Yao, T., Yang, X., Zhao, F., Wang, Z., Zhang, Q., Jupp, D., Lovell, J., Culvenor, D., Newnham, G., Ni-Meister, W., et al., 2011. Measuring forest structure and biomass in New England forest stands using Echidna ground-based Lidar. Remote sensing of Environment 115, 2965–2974.

Yu, Y., Saatchi, S., 2016. Sensitivity of L-band SAR backscatter to aboveground biomass of global forests. Remote Sensing 8, 522.

Zebker, H.A., Villasenor, J., 1992. Decorrelation in interferometric radar echoes. IEEE Transactions on geoscience and remote sensing 30, 950–959.

Zhou, Y., Hong, W., Cao, F., Wang, Y., Wu, Y., 2008. Analysis of temporal decorrelation in dual-baseline PolInSAR vegetation parameter estimation, in: Geoscience and Remote Sensing Symposium, 2008. IGARSS 2008. IEEE International, IEEE. pp. II–473.

Biography

Nafiseh (Shima) Ghasemi obtained her BSc degree in Geodesy and Geomatic engineering from K.N.Toosi University, Tehran, Iran in 2008, and the MSc degree in Remote sensing with afocus on microwave remote sensing at K.N.Toosi University in 2011. In September 2014, she was awarded the Erasmus Mundus scholarship to study PhD at the Faculty of Geo-Information science and Earth Observation (ITC) at the University of Twente. Her research interests include PolInSAR for environmental studies, machine learning, and crop mapping and monitoring by means of SAR and optical data.

Author’s publication

Published ISI journal articles

- **Ghasemi, N.**, Tolpekin, V., Stein, A., 2018. Assessment of forest above-ground biomass estimation from PolInSAR in the presence of temporal decorrelation. *Remote sensing journal* 10(6), 815.
- **Ghasemi, N.**, Tolpekin, V., Stein, A., 2018. A modified model for estimating tree height from PolInSAR with compensation for temporal decorrelation. *International Journal of Applied Earth Observation and Geoinformation* 73, 313–322.
- **Ghasemi, N.**, Tolpekin, V., Stein, A., 2018. Estimating tree heights using multibaseline PolInSAR data with compensation for temporal decorrelation, case Study: AfriSAR campaign data. *IEEE Journal of Selected Topics in Applied Earth Observations and Remote Sensing* 11(10), 3464–3477.

Conference presentations

- **Ghasemi, N.**, Tolpekin, V., Stein, A., 2018. Exploring the effect of adaptive coherence estimation on tree height extraction from PolInSAR data *ESA living planet symposium 2019*, 13-17 May, Milan, Italy. Accepted for oral presentation.

ITC Dissertation List

http://www.itc.nl/Pub/research_programme/Research-review-and-output/PhD-Graduates